Roddy Alexander Romero Antayhua

Contribuições ao projeto de leitores e dispositivos sensores baseados em retroespalhamento sem chip, de baixo custo

Florianópolis
2018

Ficha de identificação da obra elaborada pelo autor,
através do Programa de Geração Automática da Biblioteca Universitária da UFSC.

Roddy Alexander Romero Antayhua

CONTRIBUIÇÕES AO PROJETO DE LEITORES E DISPOSITIVOS SENSORES BASEADOS EM RETROESPALHAMENTO SEM CHIP, DE BAIXO CUSTO

Esta Tese foi julgada adequada para obtenção do Título de Doutor em Engenharia Elétrica e aprovada em sua forma final pelo Programa de Pós-Graduação em Engenharia Elétrica da Universidade Federal de Santa Catarina.

Florianópolis, 13 de Setembro de 2018.

_____
Prof. Bartolomeu Ferreira Uchôa Filho, Dr.
Coordenador do Curso

_____
Prof. Fernando Rangel de Sousa, Dr.
Orientador
Universidade Federal de Santa Catarina

_____
Prof. Carlos Renato Rambo, Dr.
Coorientador
Universidade Federal de Santa Catarina

Banca Examinadora:

_____
Prof. André Augusto Mariano, Ph.D.
Universidade Federal de Paraná

_____
Prof. Mário de Noronha Neto, Dr.
Instituto Federal de Santa Catarina

_____
Prof. Walter Pereira Carpes Junior, Dr.
Universidade Federal de Santa Catarina

Aos meus pais Rodolfo e Fidela, a minha esposa Jaqueline e a minha filha Liz.

AGRADECIMENTOS

RESUMO

A tecnologia *chipless*, baseada em *tags* sem *chip* para a identificação de objetos, tem surgido como uma alternativa de baixo custo à tradicional com *chip*, referida comumente como RFID (identificação por radiofrequência). Mais recentemente, o uso de sensores *chipless* também foi proposto em situações específicas, como no caso de sensoriamento em ambientes hostis ou no monitoramento de itens de muito baixo custo, por exemplo, onde sensores RFID não são adequados. Esta pesquisa se concentrou no estudo de um sistema de monitoramento *chipless*. Foi identificado que garantir uma distância máxima de comunicação adequada entre uma *tag* e o seu dispositivo leitor era um dos maiores desafios nesses sistemas, especificamente quando o sensor e o leitor têm seus tamanhos restritos devido aos requisitos específicos da própria aplicação. Consequentemente, neste trabalho, um novo projeto de sensor foi proposto visando o aumento de sua eficiência de radiação. Vários protótipos foram implementados em substratos de baixo custo, tais como laminados de uso comum na fabricação de placas de circuito impresso, e substratos flexíveis como o plástico e o papel. Testes feitos com os propótipos demonstraram resultados comparáveis aos sensores reportados na literatura em termos de sensibilidade e, sobretudo, um nível de seção reta de radar superior, considerando seu tamanho reduzido. Adicionalmente ao projeto do sensor, uma análise teórica e testes experimentais foram conduzidos para verificar a necessidade do uso de técnicas de cancelamento de autointerferência em sistemas monoestáticos baseados em leitores *chipless* com o objetivo de melhorar a leitura da *tag*. Ambas as propostas feitas neste trabalho, tanto do lado do sensor como do leitor, podem contribuir para o aumento do alcançe de leitura em sistemas de monitoramento *chipless*.

Palavras-chave: sensores miniaturizados, aumento da RCS, cancelamento de autointerferência, substratos flexíveis de baixo custo, metodologia de projeto de sensor *chipless*, sensibilidade do sensor.

RESUMO EXPANDIDO

Introdução

A internet das coisas (IoT) prevê bilhões de objetos interconectados trocando informação de maneira continua e sem intervenção do homem. Tudo isto com o intuito de um aumento da qualidade de vida em diversas áreas tais como a saúde, o lazer e o entretenimento, as relações interpessoais, o comércio, a agricultura, a prevenção de desastres naturais, entre outros.

No entanto, uma dúvida surge a partir desse conceito de IoT. Será que é possível que todos os objetos sejam conectados a esta grande rede? O quê acontece com objetos de baixo custo, quando comparados com o custo do *hardware* necessário para sua conexão?

Pode-se imaginar que a possível solução a essa questão seja o uso de etiquetas e sensores de ultra-baixo custo, capazes de comunicar às unidades de processamento disponíveis, sejam fixas ou móveis, as informações mais relevantes sobre o objeto: identificação e/ou informação de alguma variável crítica que se deseja monitorar. Para viabilizar tais sensores, precisaria-se de uma tecnologia que diminua a quantidade de componentes eletrônicos e, ao mesmo tempo, seja plausível de integração ao processo produtivo do objeto em questão, tendo assim como alvo principal a diminuição dos custos de produção. Também, o monitoramento desse sensor dentro do contexto da IoT implica o acesso a suas informações a distância (sem fio) e que suas as dimensões sejam reduzidas (estrutura miniaturizada).

Levando esses requisitos em consideração, esta pesquisa centrou a sua atenção na tecnologia *chipless*, cujo nome quer dizer "sem chip". Originalmente, ela foi proposta como alternativa à de RFID (identificação por radio-frequência), que utiliza etiquetas com chips para a identificação de objetos. Posteriormente, sensores *chipless* foram propostos. Eles consistem em estruturas com formato específico, baseadas em uma combinação de materiais condutores e dielétricos, capazes de modificar a informação (amplitude e fase) da onda eletromagnética refletida em função do parâmetro a ser monitorado. A informação pode ser recuperada pelo dispositivo leitor compatível, tanto no domínio do tempo como no da frequência, e codificada na amplitude, frequência e/ou fase. Se o sensor cumprir com certas especificações de formato, tamanho, eficiência de radiação, e além disso, pode ser fabricados com materiais de baixo custo e utilizando processos compatíveis aos objetos aos que serão integrados, a tecnologia de sensores *chipless* pode servir como solução compatível com as demandas impostas no contexto da

IoT.

Objetivos

Neste trabalho de pesquisa, buscou-se contribuir na área da tecnologia *chipless*, em particular, com o tema de sensores *chipless*, estudando as limitações principais para sua adoção e propondo melhorias para atingir uma solução de monitoramento sem fio. Baseado na revisão do estado da arte, e alinhado ao escopo desta pesquisa, o principal objetivo deste trabalho é dar contribuições relacionadas a sensores *chipless* miniaturizados planares de única camada com codificação na frequência, operando na banda de 2,4 GHz (ISM). Os objetivos específicos do trabalho são:

1. Identificar as variáveis críticas do sistema de monitoramento *chipless* que impactam na distância de leitura, considerando a restrição de tamanho e custo tanto do lado do leitor leitor e do sensor.

2. Estudar a relação entre miniaturização e seção reta de radar em sensores planares miniaturizados e propor uma nova estrutura que permita maximizar o desempenho considerando essas variáveis.

3. Estudar a relação entre sensibilidade e miniaturização, dando especial ênfase ao caso de sensores fabricados com materiais de baixo custo.

4. Delinear uma método para o projeto do sensor proposto baseado nas entradas de projeto: especificações e materiais.

5. Estudar e propor melhorias para o leitor.

Metodologia

Para atingir os objetivos propostos, foram realizados os procedimentos listados a seguir:

1. Estudo das propriedades elétricas dos materiais a utilizar na construção dos sensores.

2. Revisão e classificação dos sensores reportados na literatura científica.

3. Revisão de técnicas de medição de sensores *chipless* e leitores *chipless* reportados.

4. Análise das variáveis que impactam na leitura do sensor.

5. Proposta de nova estrutura para o sensor.

6. Modelagem do sensor e verificação utilizando simulações eletromagnéticas.

7. Obtenção de principais figuras de mérito a partir do modelo.

8. Implementação e medição de protótipos em FR-4, e comparação com esperado.

9. Implementação e medição de protótipos em substratos flexíveis (plástico, papel).

10. Proposta de melhorias a partir dos resultados de medição.

11. Proposta e verificação de técnicas de leitura de sensores *chipless*.

Resultados e Discussão

Esta pesquisa teve como foco principal o estudo de sistemas de monitoramento *chipless*, nos quais a leitura do sensor sem fio é dificultada dado os seus requisitos de miniaturização e materiais de baixo custo para sua fabricação. A seguir, encomtram-se as contribuições principais da tese:

- A respeito do sensor, foi proposta uma estrutura que pudesse incrementar a eficiência de radiação do espalhador (*scatterer*) independentemente do projeto do transdutor. Dessa maneira, a RCS (seção reta de radar) poderia ser otimizada segundo a restrição de tamanho do sensor imposta pela aplicação.

- Foi proposto um modelo elétrico para a obtenção das principais figuras de mérito do sensor, RCS e sensibilidade, podendo assim identificar as variáveis críticas no projeto do sensor. O modelo foi comparado com simulações eletromagnéticas verificando sua acurácia.

- Duas rodadas de protótipos foram implementadas para verificar a funcionalidade do sensor operando na banda ISM. Os primeiros protótipos feitos em FR-4 comprovaram que o sensor pode atingir níveis de sensibilidade comparáveis aos reportados na literatura, e ao mesmo tempo, um grau considerável de miniaturização com um nível de RCS adequado para monitoramento sem fio.

- Os protótipos fabricados em substratos flexíveis também demonstraram que a estrutura proposta é vantajosa nos casos em que os materiais tem perdas consideráveis. A partir dos resultados de medição, foram propostas melhorias, principalmente para incrementar a sensibilidade.

- No que diz respeito ao estudo sobre o leitor, foi analisado o caso de leitores monoestáticos com única antena e interrogação por onda contínua, compatíveis com o sensor proposto. Foi verificado que nesse tipo de leitores, o sinal de autointerferência proveniente do transmissor limita a distância de leitura. A limitação pode ocorrer a causa do ruído ou da amplitude do sinal de fuga do transmissor. Para ambos casos foram obtidas as distâncias de leitura máximas teóricas.

- Um protótipo de leitor com capacidade de cancelamento de autointerferência foi construído. Nesse protótipo foi verificada a limitação por autointerferência e o quanto o seu cancelamento é importante para garantir o aumento da distância de leitura.

Considerações Finais

Os objetivos traçados no começo da pesquisa foram atingidos, contribuindo assim com o projeto de sistemas de monitamento baseado em tecnologia *chipless* no contexto da IoT. Os resultados obtidos poderão servir como base a futuros trabalhos, os quais incluim um rodada de testes de sensibilidade com sensor fabricado com as melhorias propostas, testes experimentais do sistema completo (leitor e sensor), modificação do sistema para leitura em polarização cruzada, e implementação de sistema de monitoramento *chipless* em outras bandas de frequência, por exemplo a UHF.

Palavras-chave: sensores miniaturizados, aumento da RCS, cancelamento de autointerferência, substratos flexíveis de baixo custo, metodologia de projeto de sensor *chipless*, sensibilidade do sensor.

ABSTRACT

Chipless tags for objects identification have been proposed as a low-cost alternative to the well-known chipped Radio Frequency IDentification (RFID) tags technology. More recently, chipless sensors have also been indicated for specific applications in which RFID-based sensor are not very suitable, such as in harsh environments or ultra-low cost item monitoring. This research have focused on the study of a chipless monitoring system. It was identified that the reading range is one of the most important concerns of these systems, specifically when both the sensor and the reader are size restricted due to a specific application. Consequently, in this work, a new sensor design is proposed to tackle this issue. Several prototypes of the sensor have been implemented in low-cost substrates, such as common PCB glass epoxy-based laminates, and flexible substrates such as plastic and paper. These have shown comparable results to the reported sensors in literature in terms of sensitivity and, more importantly, a superior radar cross section level considering its reduced size. In addition to the sensor, a theoretical analysis and some tests were conducted to prove the need of implementing self-interference cancellation techniques in single-antenna monostatic chipless readers for improving the readability of the tag. Both proposals, on the sensor and on the reader side, can contribute to the reading range enhancement in frequency coded chipless systems.

Keywords: sensor miniaturization, maximizing *tag* RCS, self-interference cancellation, low-cost flexible substrates, chipless sensor design methodology, sensor sensitivity.

LIST OF FIGURES

LIST OF TABLES

ACRONYMS

AC Amplitude-based Codification.

ADC Analog-to-Digital Converter.

CPW Coplanar Wave Guide.

CW Continuous Wave.

DS Drop Size.

EM EletroMagnetic.

EP Encoding Particle.

FC Frequency-based Codification.

FDTD Finite-Difference Time-Domain.

FEM Finite Element Method.

FMCW Frequency-Modulated Continuous Wave.

FSCW Frequency-Stepped Continuous Wave.

IC Integrated Circuit.

IoT Internet of Things.

ISM Industrial, Scientific and Medical.

LH Left-Handed.

LPDA LogPeriodic Dipole Array.

MoM Method of Moments.

ORR Open Ring Resonator.

PET PolyEthylene Therepthalate.

PU Processing Unit.

PVA PolyVinyl Alcohol.

RCS Radar Cross Section.

RFID RadioFrequency IDentification.

RH Relative Humidity.

RT ReTransmission.

SAW Surface Acoustic Wave.

SDR Software Design Radio.

SIC Self-Interference Cancellation.

SRR Split Ring Resonator.

TDR Time-Domain Reflectometry.

TL Transmission Line.

UWB Ultra-Wide Band.

VNA Vector Network Analyzer.

SYMBOLS

A Complex number related to RCS structural mode.

C_A Antenna capacitance. Sensor capacitance.

$ENOB$ Effective number of bits.

E_{inc} Incident electrical field intensity.

E_{scat} Scattered electrical field intensity.

FSV Full-scale voltage.

G_a Gain of the reader antenna.

G_b Baseband voltage gain at the receiver.

P_{inc} Scattered incident power.

P_{rx} Received power by the reader.

P_{scat} Scattered radiated power.

P_{tx} Reader Transmitted power.

Q_A Sensor quality factor.

Q_r Sensitized resonator quality factor.

Q_s Scatterer quality factor.

RCS_a Antenna mode Radar cross section.

RCS_s Structural mode Radar cross section.

RCS Radar cross section.

R_A Antenna resistance.

R_l Loss resistance.

R_r Radiation resistance.

SNR Signal-to-noise ratio.

S_x^y Relative sensitivity of variable y due to x.

S_{inc} Incident power density.

S_r Sensitivity of the reader.

S_{scat} Scattered power density.

S Absolute sensitivity.

V_l Downconverted leakage voltage term.

V_{tag} Downconverted chipless tag voltage term.

X_A Antenna reactance. Sensor reactance.

Z_A Antenna self-impedance.

Z_L Antenna load impedance.

α Normalized sensor resonance frequency.

β Normalized resonator resonance frequency.

η_r Radiation efficiency.

η Radiation efficiency.

λ Wavelength.

ω_A Angular resonance frequency of the sensor.

ϕ_s Slit angle of a circular ORR.

ϕ Phase term; azimuth angle.

θ Elevation angle.

ε_r Relative permittivity.

d Distance between reader and chipless tag.

f_A Sensor resonance frequency.

f_S Scatterer resonance frequency.

f_r Sensitized resonator resonance frequency.

f_{res} Resonance frequency.

g_s Slit size.

h substrate height.

k Magnetic coupling factor.

l_o lateral length.

l_{ORR} ORR lateral length.

l_{SRR} SRR lateral length.

s_o ORR slit size.

t_c Coating layer thickness.

t_s Substrate thickness.

CONTENTS

1 INTRODUCTION

1.1 MOTIVATION

Guided by the under-construction definition of the Internet of Things (IoT) [1], it is easy to imagine some of the daily objects we interact with as turning wirelessly interconnected and exchanging information so as to hopefully build a smarter world. Still, a question remains regarding the IoT pervasiveness level: will the IoT provide with intelligence to every single "thing" around us? Maybe one day, as this futuristic trend is clearly seemed to be pushed by enthusiastic giant players which envisage a promising billionaire market [2, 3]. For us, users, what is indeed important behind this trend is that it could be a potential quality-of-life promoter, since these "things", supplied with intelligence, could efficiently assist our daily tasks in every aspect of our lives. This includes areas such as health, entertainment, education, social relationships, agriculture, manufacturing, disaster prevention, among others [4, 5, 6, 7, 8].

Certainly, there are still some social and technological barriers which are delaying IoT's materialization [9, 10, 11, 12]. In determined applications, one of these related barriers is cost. A particular situation can be considered in which it is desired to monitor a specific environmental parameter at the item level, for example, the freshness of a box of juice in a supermarket shelve. If we were to add to the box the capability of communicating its freshness level in real time, we would probably be impeded due to the electronics associated cost compared to the cost of the box of juice itself.

Fortunately, being conscious of the fact that some "things" only need to be intelligent enough, they would just need to communicate specific own states that are judged as important to the interested users. Thus, there is no need, in this case, for the "thing" to process any information or even execute any particular action. This high-level processing should be performed by a more complex element which can then delivered the treated information to the cloud. Having said that, we could reckon that a practical sensor, using a simplified communication protocol with this high-level processing unit and making part of this low-cost object, will be sufficient to get the job done.

Figure 1.1 illustrates the case commented above. The box of juice

in a supermarket shelf is monitored by a fixed Processing Unit (PU), which obtains periodically the freshness-related data, This PU extract only relevant information from the embedded low-cost sensor, process it, and then deliver it to the supermarket data server for storage or further data analysis. This PU may also be mobile, so the juice box information can be retrieved whenever is required by any user.

Figure 1.1: Example of wireless sensor application embedded into a low-cost product. Information is retrieved by the fixed or mobile processing unit (PU) for further analysis.
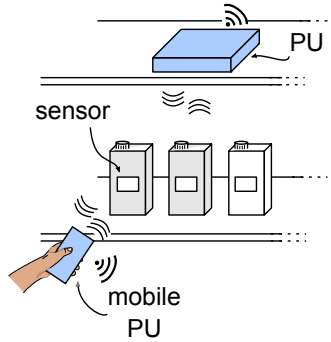
Source: The author.

Indeed, low-cost sensing is a subject in constant evolution as it is required in other scenarios similar to that of the supermarket juice box. From the technical aspects standpoint, research efforts are mostly focused on energy autonomy, increasing sensitivity and selectivity, new materials, miniaturization, and information security [13, 14, 15, 16, 17]. Among all the proposed solutions, passive wireless-powered sensors seem to be a viable path for low-cost passive implementations. Particularly, RadioFrequency IDentification (RFID)-enabled sensors have been presented in which low-power sensors are combined with commercial RFID tags in order to build passive wireless sensing tags which are compatible with commercial RFID readers [18]. In addition to the most recent studies on this topic [19, 20], this technology is also already being offered for humidity, thermal and strain sensing suitable for industrial applications or structural health monitoring [21, 22, 23, 24]. As this technology may attend the majority of applications, even the cost of the tag's chip can be an obstacle in the demand of ultra low-cost solutions.

Another limiting factor to the massive installation of sensors

within the IoT context, besides the cost, is the requirement of being unobtrusive. This issue is directly related to both the size and the appearance of the sensor. For this reason, miniaturization is a another important factor to be dealt with in sensor technology. For instance, due to its compatibility with CMOS standard technology, RFID-enabled wireless sensors are also a valid approach on the aim to miniaturized low-cost solutions [25, 14, 26]. Unobtrusiveness may also be facilitated by embedding the sensors within the monitored object, which makes them unnoticed. Therefore, compatible materials and fabrication processes for the sensors and the objects are required [14]. Moreover, integrating the sensor in the same productive process of the object may reduce even more the sensors relative cost compared to the object since they can be produced on a large scale [27].

Inspired on the RFID technology, another one, referred as *chipless RFID*, has recently appeared with the aim of tackling some of the above mentioned issues such as fabrication cost, miniaturization, and compatibility with alternative fabrication processes [28, 29]. The term *chipless* was coined in the last decade and alludes to silicon-less wireless tags, that is, without integrated or discrete semiconductor-based devices, which, evidently, alleviates the sensor cost attributed to the embedded electronics. At its earlier stages, chipless technology surged as a cheaper alternative for the already widespread chipped RFID tags used for objects identification [28]. More recently, chipless sensing tags, also known as *chipless sensors*, have been also proposed [29]. Moreover, due to its potential ultra-low fabrication cost, chipless ID and sensing tags have been fore-casted as being part of the huge growing market of RFID-based tags [30, 24].

Guided by the promise of achieving low-cost wireless miniaturized sensors through chipless sensing, this technology was chosen to be the main driver of the present research. Chipless technology imposes fresh technical challenges which have provoked an ever-increasing number of published research works in the last years [28, 29]. Consequence of this numerous scientific production, many different research branches have been outlined, which in some cases are tightly interrelated and may lead to confusion for the neophyte interested on this topic. For this reason, a brief discussion of these many branches embracing chipless technology is presented in the following subsection, and, after that, the specific scope of this research is revealed.

1.2   RESEARCH SCOPE

Chipless sensors are totally passive and the information is retrieved from the EletroMagnetic (EM) backscattering waves produced by the induced currents in the sensor after illumination from another radiating source [29]. These induced currents, and, thus, the backscattering waves, are dependent on the electrically conductivity and dielectric characteristics of the illuminated sensor. The desired information of the sensor is carried in the variation on these electrical characteristics when modified after the interaction with the surrounding environment.

The information from the backscattered waves can be acquired either after time-domain [31] or frequency-domain [32] reading techniques. For instance, chipless ID and sensing tags specifically designed for time-domain interrogation, referred as Time-Domain Reflectometry (TDR)-based tags, rely on the absence or presence of time-spaced backscattered pulses after being impinged by an EM RF pulse. Therefore, its design focuses on producing controlled time delays along the physical structure of the tag [33]. Surface Acoustic Wave (SAW)-based tags are considered precursors of these type of tags [34]. It is not the purpose of this research to address time-domain chipless tags, and a review of some recent works on this topic can be found in [35].

Alternatively, in frequency-domain tags, the information is usually interpreted through the Radar Cross Section (RCS), which characterizes the electromagnetic signature of an object by calculating the ratio between the intensity of the incident and the scattered EM wave power as a function of frequency [36]. Compared to time-domain tags, frequency-domain chipless tags usually allow fully-printable solutions and are, in general, capable of achieving more data density (for ID tags) and are more easily conceived into compact structures. Therefore, they are the most common reported type of chipless tags for both identification and sensing purposes [29, 37].

There are two common options for the interrogation of frequency-domain chipless sensors. In the first, the sensor is designed to carry the desired information in the variation of its RCS amplitude at a fixed frequency [38]. This method can be considered as an Amplitude-based Codification (AC) of the sensor information. In the second, the information is codified into the frequency variation of the RCS distinguishable(s) peak(s) or valley(s) within the observable frequency sweep range, which, in this way, corresponds to a Frequency-based Codification (FC) [39]. Both AC and FC are exemplified in Fig. 1.2. They are the

most common techniques used for codifying the information in chipless frequency-domain sensors, however, other phase- and polarization-based codifications have been also reported [40, 41, 42]. All these codifying approaches can be considered as analog, to mean that the sensing variable, that is, the RCS, changes its value continuously with respect to the variation of the monitored parameter. Nonetheless, any of these codification techniques could also be turned into digital as well, for example, based on threshold detection [43, 44].

From the interrogator point of view, the FC approach seems to be more robust than AC, since the interrogator does not need to keep a precise amplitude reference in the long-term. On the other hand, FC requires to sweep over the whole frequency range for interrogating the sensor, whereas in AC a narrower band can be employed once the exact working frequency of the sensor is defined.

Figure 1.2: Main information codification types for frequency-based chipless sensors: Amplitude-based Codification (AC) and Frequency-based Codification (FC).
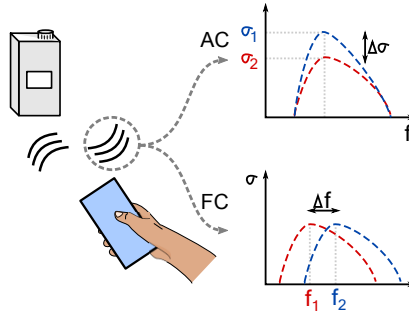
Source: The author.

In order to interrogate frequency-domain chipless sensors based on the backscattered response after EM illumination, reader's transmitter emit either a Continuous Wave (CW) or Ultra-Wide Band (UWB) pulses, as illustrated in Fig. 1.3. Readers based on CW interrogation employ common radar transceiver architectures, such as Frequency-Stepped Continuous Wave (FSCW) or Frequency-Modulated Continuous Wave (FMCW) radars [36]. In both architectures, the frequency of the signal carrier is swept and the backscattered wave from the tag is measured at each frequency step. Conversely, UWB pulsed interrogation is based on narrow RF pulses whose spectral power density usually extends from 3 to 10 GHz. In this way, the EM signature of the sensor is retrieved

from a single interrogation pulse, which is advantageous from the point
of view of the total reading time [45]. Nonetheless, UWB interrogation
require, in general, finer electronic components such as pulse generators
and high-speed analog-to-digital converters, which generally makes them
unsuitable for low-cost implementations [46], and are also prone to jitter
and synchronization issues [45].

Figure 1.3: Continuous-Wave (CW) vs Ultra-Wide Band (UWB) pulsed
interrogation
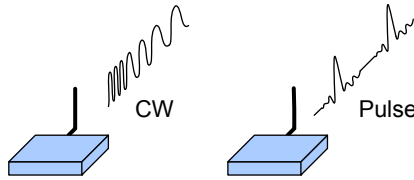
Source: The author.

Besides the reader architecture, antennas also play an important
role on the reading strategy of the whole system. Provided an applica-
tion, either bistatic or one- or two-antenna monostatic configurations
might be specified. In addition to this, the antenna type is selected
according to the main design parameters such as gain, bandwidth, and
size. Moreover, antenna polarization must be compatible to the tag
polarization-related strategy for information recovery. One can classify
these strategies into: co-polarization [47], dual polarization [48] and
cross-polarization [49]. Among the three, co-polarization interrogation
is the most common reading strategy reported in frequency-domain
chipless tags. In the case of dual polarization interrogation, the tag is
illuminated twice, with two orthogonally-polarized EM waves, and the
information is obtained with co-polarization interrogation from both.
This strategy is usually employed for doubling the amount of informa-
tion retrieved from the tag, while this must be designed appropriately
for this purpose. Finally, cross-polarization reading is used for reducing
the clutter interference [50]. Among these three polarization modes, co-
polarization interrogation is inherently compatible with single-antenna
monostatic configuration, which can be favorable to low-profile compact
readers. On the other hand, cross-polarization and dual-polarization
reading are often implemented with two antennas, although circular
polarization [51] or carefully designed two-port dual polarized antennas
may be a viable solution for reducing the reader size [52].

On the tag side, miniaturization and cost may be more easily

achieved through the usage of planar structures [53]. Planar chipless sensors are also suitable for additive fabrication processes which can reduce the fabrication cost, specifically in uniplanar (single-layer) designs [54]. Although, uniplanar tags may be more vulnerable to material-related drifts and environment compared to "grounded" structures, this issue might be controlled by considering these factors during the design stage or by tuning techniques [55]. In addition to this, additive processes allow the usage of flexible and low-cost substrates, which is favorable for fully disposable tags or even promotes the integration of the sensor with the object under monitoring [56].

Miniaturization is also directly related to the design approach adopted. According to their radiation properties, two main approaches can be distinguished. The first one refers to the ReTransmission (RT) tags [37]. Its design consider separated structures for the reception/transmission antennae and the sensing element. As the name reveals, after reception, the incident EM wave is guided along a transmission line and modified on its way by the sensing element before it is retransmitted back to the reader. The reception and the transmission are usually accomplished by two separated cross-polarized antennas, thus requiring cross-polarizing interrogation [57].

The tags regarding the second approach are known as radiofrequency Encoding Particle (EP), whose name refers to the fact of integrating in the same structure both the antennae and the sensing element [58]. In this manner, the EPs are more suitable for miniaturized structures, even though there is an inherent trade-off between size reduction and RCS magnitude which may limit the reading range of the tag. Examples of chipless sensors presented in literature which followed RT and EP approaches are shown in Fig. 1.4(a) and (b), respectively.

All of the subjects discussed above regarding chipless technology are summarized in the tree diagram of Fig. 1.5. The highlighted terms in this diagram point out the specific focus of this research, e.i., *frequency-domain frequency-coded uniplanar chipless sensors designed with the encoded-particle approach.* In particular, this research is aimed at working with this type of sensors looking forward implementing miniaturized chipless sensors by enabling the use of low-cost materials and additive fabrication processes.

Figure 1.4: Chipless sensors following the (a) Retransmission (RT) [59] and (b) the Encoding Particle (EP) [39] approaches.

(a)   (b)
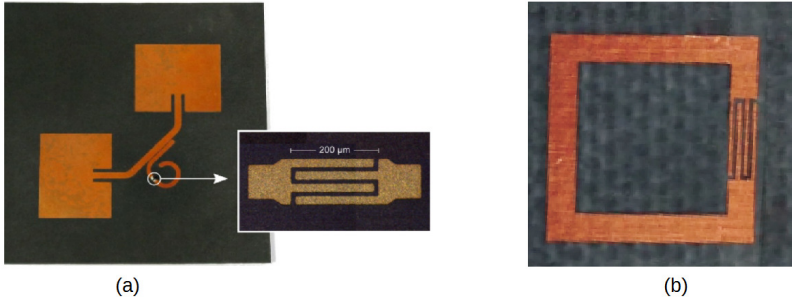
Source: The author.

Figure 1.5: Tree diagram showing the diversity of subjects regarding chipless technology and highlighting the scope of this research.
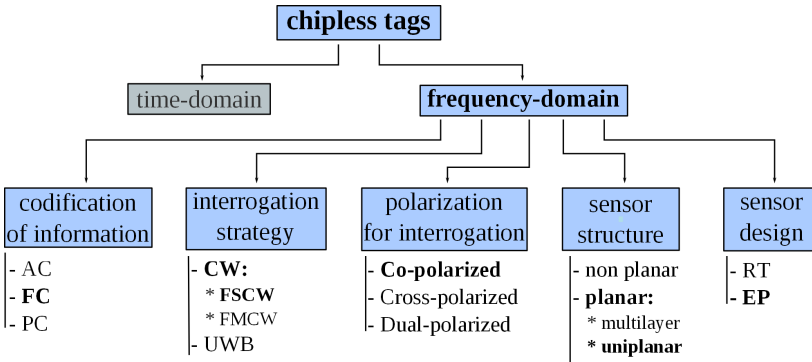
Source: The author.

1.3   RELATED STATE-OF-THE-ART STUDIES

The most relevant works found in literature regarding AC and FC chipless sensing tags are summarized in Table 1.1 and 1.2, respectively. They were classified according to its application, design approach, number of physical layers and polarization reading strategy. This list only includes planar structures, which are directly related to the scope of this research. A more extensive review on chipless sensors, not restricted to frequency domain and planar structures, can be found in [29, 60].

Several applications have been addressed such as the monitoring of temperature, strain, displacement, light, gas, resistance and Relative Humidity (RH), as well as angle and crack detection. Moreover, it must be mentioned that some structures include both identification and sensing capabilities on a single tag [61, 62]. Regarding the design approach, both RT and EP structures were reported. It can be also noticed that some of the listed sensors are implemented with a single conductive layer (uniplanar), all of them based on EP structures. Lastly, all three polarizations strategies were reported. Among them, co-polarization was the most frequent, while cross-polarization is mostly used in RT tags.

According to the research scope, it is interesting to center the attention on FC tags that follow the EP approach. For example, in [61], a mushroom structure build up by shorted-circuit patch antennas was used for monitoring strain. The sensing element is based on a Left-Handed (LH) Transmission Line (TL) whose equivalent capacitance based on the alongside metal plates varies according to the tension applied to it. The authors presented measured results of the implemented sensor working around $3.2\,\mathrm{GHz}$ obtaining 300 to $700\,\mu m$ of detection range which corresponded to frequency shift from 3.09 to 3.23 GHz approximately. The sensor occupied a total area of $20\,\mathrm{x}\,20\,\mathrm{mm}^2$ while achieving an RCS peak of -28 dBsm.

In [72] a half-wave dipole strip resonator based on a C-like structure is presented for monitoring RH. The sensitive material used for reacting upon humidity variations was based on silicon nanowires (Si-NW), which were deposited through chemical vaporization. The sensor was designed to work around 2.5 GHz. Experimental results showed a 25 MHz variation when the environment was changed from a 75 % RH (at 3° C) to 43 % RH (at 19° C). The sensor occupied a total area of $25\,\mathrm{x}\,10\,\mathrm{mm}^2$ while achieving an RCS peak of -29 dBsm.

In the study presented in [32], the authors demonstrate a RH

sensor based on electric-field coupled (ELC) resonator. Two prototypes were implemented, each one using a polyimide substrate and a PolyVinyl Alcohol (PVA)-based coating as sensitive materials, respectively. The second one achieved a higher frequency shift of approximately 600 MHz around 6.5 GHz when the RH was changed from 35 to 85%. The sensor occupied a total area of $7 \times 7\,mm^2$.

An open-ring resonator is used as RH sensor in [39] where, similarly to [32], PVA was also used as the sensitive material. This structure was designed at a center frequency of approx. 2.8 GHz, achieving a shift from 2.74 GHz to 2.85 GHz when the environment RH was varied from 14% to 19%. This sensor occupied a total area of $8 \times 8\,mm^2$.

In [62], a mirrored C-shaped slot resonator is used for monitoring temperature. The sensitive material used was a polyamide, which was added in the slot so to vary the equivalent capacitance of the resonator. The sensor worked around 5.5 GHz and achieved a RCS valley of approximately -50 dBsm from its -27 dBsm average value. This sensor presented a circular format with a radius of $6\,mm^2$.

Coupled rectangular-shaped loops were used as RH sensor working around 3.3 GHz in [74]. As in [72], Si-NWs were also used. The sensor was tested under a 78 to 98% RH variation presenting a frequency shift from 3.321 GHz to 3.297 GHz. The sensor occupied a total area of $34 \times 12\,mm^2$ while achieving an RCS peak in the range of -45 to -48 dBsm.

In [75] several square loop resonators operating between 3 to 10 GHz were implemented for electrical permittivity characterization of planar surfaces. The biggest resonator occupied a total area of $35 \times 1.8\,mm^2$.

A different approach from the rest has been used in [76], where a Van-Atta reflectarray working around 30 GHz is used as RH sensor. The array was implemented over polyamide substrate, which acted as the sensing material as well. For the tested RH range of 10 to 75%, a total shift from 28.4 GHz to 31.2 GHz was measured. The sensor occupied a total area approximately equivalent to a credit card ($50 \times 60\,mm^2$) while achieving an RCS peak of -23 dBsm.

Finally, following a similar concept based on elements array, three nested loops have been printed over a PolyEthylene Therepthalate (PET)-coated paper, which were then attached to a grounded substrate made of cardboard, building a resonant planar cavity with three different resonance frequencies [44] . The paper coating is sensitive to the humidity and, thus, changes the resonance frequency of each loop. The authors claim a frequency shift of up to a 270 MHz (in the band around 7 GHz)

when varying the %RH from 50 to 100%.

All these cited works are listed in Table 1.3, where, additionally to the the features already discussed, the test conditions were also included. Particularly, the physical size was presented as the maximum equivalent diagonal and area both normalized by the wavelength at central resonance frequency. Sensitivity was also calculated from the frequency shifts obtained from the reported measurements.

As it can be observed, most of these works were focused on monitoring RH. Moreover, all the sensors were fabricated with rigid substrates, except for [75, 76, 44] which used some plastic films or coated paper. Also, the majority of the sensors presented an uniplanar structure except for [61, 76, 44], which may be exploited to be fully fabricated by using direct additive fabrication processes such as printing [47, 67, 104, 56]. In addition, it is also observed that most of the sensors operated at the 2 to 6 GHz band, whereas higher frequencies were explored in a few cases.

All the sensors can be considered compact structures (relative to the wavelength), being the most compact the one reported in [39]. The work in [76] did not followed the same miniaturization approach since the design was based on an array of reflectors to increase the RCS for increasing the reading range, while keeping a reasonable total size by operating at a much higher frequencies. This can be verified from the RCS peak which is higher than all the other implementations. A similar approach was used in [44], where a 3×3 array of resonators was used, which increased mainly the difference between the RCS values at resonance (valleys) and not resonance frequencies. The works in [61, 72] presented similar RCS peaks, which are about 5 to 6 dB lower than the one in [76]. The lowest reported peak was that of the work in [74].

All of the sensors carried its information on the shift of frequency where RCS peak occurred, except for the work in [62], which is based on slots resonators, and the work in [44], based on grounded loop resonators. Both tracks the frequency shift of the RCS valleys.

Regarding the sensitivity among the RH sensors, the best result was achieved by the sensor in [32] followed by the one in [76]. Since the sensitivity is also a matter of the material used for interacting with the environment, it is difficult to make a fair comparison between structures that used different materials and fabrication processes. Moreover, materials do not have a linear relation upon the monitored parameter but a piecewise response along its range of change.

Table 1.1: Frequency-domain planar AC chipless sensors found in literature

Reference	Application	Design	Polarization	Uniplanar?
[63]	Temperature	EP	co	n
[64]	Angle	EP	co	n
[47]	Resistance	EP	co	y
[65]	Strain	EP	dual	y
[66]	Light	RT	cross	n
[67]	Strain / Crack	EP	co	y
[104]	Gas & Temp.	EP	co	y
[69]	Angle & Resistance	EP	co & cross	y

Table 1.2: Frequency-domain planar FC chipless sensors found in literature

Reference	Application	Design	Polarization	Uniplanar?
[70]	Displacement	RT	cross	n
[61]	Strain	EP	co	n
[71]	RH	RT	cross	n
[38]	RH & Temp.	RT	cross	n
[59]	Temperature	RT	cross	n
[40]	RH	RT	cross	n
[32]	RH	EP	co	y
[39]	RH	EP	co	y
[72]	RH & Temp.	EP	co	y
[73]	Temperature	RT	cross	n
[62]	Temperature	EP	co	y
[74]	RH	EP	co	y
[75]	Elect. Permittivity	EP	co	y
[76]	RH	EP	co	n
[44]	RH	EP	co	n

Table 1.3: Frequency-domain planar EP chipless sensors main performance metrics

Reference	Struct.	Central freq. [GHz]	Diag./λ	Area/λ²	RCS [dBsm]	Sens. [Δf/ΔΨ]	Subst. / sensitive mat.	Test cond.
[61]	Mushroom patch (LH-TL)	3.2	0.302	45.5e-3	≈-28 (peak)	0.35 [MHz/μm]	Rogers 5880 / -	VNA / monostatic / horn ant. / ndr /steel sphere as ref.
[32]	ELC	6.5	≈ 0.214	23e-3	n.r.	12 [MHz/%RH]	Taconic TLX0 / PVA	VNA / bistatic horn ant. /ndr
[39]	ORR	2.8	0.106	5.57e-3	n.r.	1.42 [MHz/%RH]	Rogers 5880 / PVA	VNA / monostatic / horn ant. /ndr
[72]	C-like strip resonator	2.5	0.2244	17.4e-3	-29 (peak)	0.78 [MHz/%RH]	FR-4/ SiNW	VNA / bistatic horn ant. / 50 cm
[62]	C-shaped slot resonators	5.5	≈ 0.22	48.4e-3	Δ RCS ≈ 23 dB	n.r.	Duroid 5880 / Polyamide (Stanyl)	read. distance 57 mm
[74]	coupled squared loops	3.3	0.39661	49.4e-3	≈ -45 (peak)	1.2 [MHz/%RH]	n.r. / SiNW	VNA / bistatic horn ant. / nr
[75]	squared loop (C-shape CPS)	[3 - 10]	0.3506	6.3e-3	n.r.	-	n.r. substrate, Ni / -	VNA / bistatic / open boundary wideband quad ridge antenna / 35 cm
[76]	Van-Atta reflectarray	30	7.8	30	-23 (peak)	43.1 [MHz/%RH]	Polyamide (Kapton)	VNA / bistatic / cross-polarized conical horn ant.
[44]	Nested loops over ground layer	3, 5.8, 7.1	[0.636 - 1.5]	[0.2025 - 1.134]	Δ RCS ≈ 20 dB	<5.4 [MHz/%RH]	photo paper on grounded cardboard, Ag ink	VNA/ monostatic / horn ant.

1.4   THESIS OBJECTIVES

The purpose of this study to contribute to the research field of chipless technology, in particular to the chipless sensors subject, by studying its fundamental limitations and proposing improvements in order to achieve an ultra-low cost solution suitable for wireless monitoring. Based on the reviewed state of the art, and lined up with the scope of this research, it is the main objective of this study to focus in frequency-coded chipless sensors that operate in the Industrial, Scientific and Medical (ISM) band, specifically, at the 2.45 GHz ISM band.

The specific objectives of this thesis include:

- Analyze the system requirements of a RFID chipless system, that is, the reader and sensing tag, to identify the most critical variables that influence on the reading range. Particularly, concentrate the analysis considering a system consisting of a low-profile dynamic reader and a miniaturized tag.

- Study the trade-off between miniaturization and RCS of a uniplanar EP-based chipless sensor and propose an alternative structure based on this understanding in order to maximize the reading range while keeping the sensor size compact.

- Study the aspects that influence on the sensitivity of these chipless sensors and understand the trade-off between sensitivity and miniaturization. Specifically, explore the case in which lossy materials are used.

- Provide a methodology to design a chipless sensor based on the proposed new structure and the study of its sensitivity according to a given set of materials and fabrication process.

- Study and propose improvements on the reader side as well, specifically for low-profile readers.

1.5   DOCUMENT ORGANIZATION

This document is organized as follow. In Chapter 2, the main terms and concepts used along the document are briefly presented. Then, the idea of the proposed chipless sensor is presented in Chapter

3, together with an electrical model from which its main figure of merits are estimated. Chapter 4 and 5 present the simulation and experimental results of prototypes implemented in FR-4 and flexible substrates, respectively. The results are discussed and compared to the state-of-the-art chipless sensors reported in literature. The analysis and experimental results of the effect of self-interference in low-profile chipless readers are left for Chapter 6. Finally, the main conclusions and contributions from this study, the proposed future work and the list of publications presented during the execution of the research are presented in Chapter 7.

2 CONCEPTS AND DEFINITIONS RELATED TO CHIPLESS SENSORS

In this document, a chipless monitoring system, which will be referred from now on as *chipless system*, is defined as the set consisted by an interrogator, also known as *chipless reader*, and a sensing tag, from now on referred as *chipless sensor*. Both elements are separated at a certain distance and communicate through a specific communication channel. An illustration of a typical chipless system is shown in Fig. 2.1. The environment surrounding the chipless sensor causes the change in the electrical characteristics of the materials used for the construction of the sensor, therefore, these changes can be interpreted by the chipless reader through the backscattering.

An important metric of the chipless system is the maximum reading distance at which the backscattered EM waves reach the chipless reader with enough power to be correctly interpreted. Understanding the factors that influence on this distance is of concern of this research. Therefore, in this chapter, several concepts related to chipless sensors are briefly introduced and discussed, since they are crucial to address the requirements responsible for the improvement of this important metric.

Figure 2.1: Elements of a chipless system.
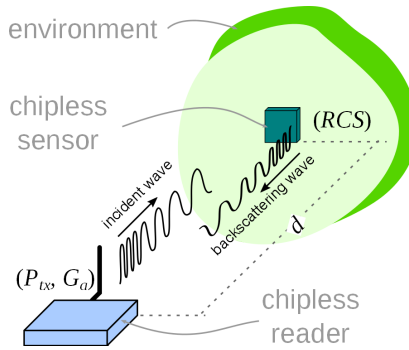
Source: The author.

2.1 READING RANGE

In free-space, the backscattered power received at a monostatic reader (P_{rx}) from an impinged object at a certain distance is derived from the Friis equation as [77]:

$$P_{rx} = \frac{P_{tx}G_a^2\lambda^2}{(4\pi d)^2}\frac{RCS}{4\pi d^2}. \tag{2.1}$$

This relation, known as the *radar equation*, relates the distance (d)-to-wavelength (λ) ratio to the reader settings, i.e. the transmitted power (P_{tx}) and the antenna gain (G_a), and to the object radar cross section (RCS).

From the radar equation, the maximum reading range in a a chipless system can be expressed as a function of the reader and sensor parameters:

$$d_{(max)} = \underbrace{\sqrt[4]{\frac{P_{tx}}{S_r}\frac{G_a^2\lambda^2}{(4\pi)^2}}}_{\text{reader}}\underbrace{\sqrt[4]{\frac{RCS}{4\pi}}}_{\text{sensor}}, \tag{2.2}$$

where $S_r = P_{rx(min)}$ is the reader sensitivity, i.e., the minimum resolvable input signal power.

The optimization on the reading range depend on the specific context of the application: Does the reader size matters? Does the operating frequency selection depends on any particular regulation? Assuming a fixed operating frequency and fixed parameters for the reader, that is, the maximum transmitted power is defined, the reader sensitivity is also given and a specific antenna type is used, it could be stated that the sensor RCS is the key factor for maximizing the reading range. Therefore, this research focuses, in the first place, on the study of how to maximize the radar cross section of miniaturized chipless sensors.[1] In the second place, the relation between the parameters in the reader is studied, and particular attention is given to low-profile chipless reader.[2]

---

[1]This would be subject of Chapters 3 to 5.
[2]This subject is covered in Chapter 6.

2.2 RADAR CROSS SECTION OF AN ANTENNA

As highlighted in Section 1, it is of particular interest to study uniplanar EP-based sensors. For this matter, wire-type antennas are a starting point for the RCS analysis since they are compatible with uniplanar designs. Moreover, they could easily be adapted for de-polarizing structures which facilitates the clutter suppression [50].

From the the IEEE definition of the radar cross section of an object impinged by an EM wave [78], the following expression can be deduced:

$$RCS = \lim_{d \to \infty} 4\pi d^2 \frac{|E_{scat}|^2}{|E_{inc}|^2} \quad [\text{m}^2]; \tag{2.3}$$

where d is the distance between the reader in and the object in meters, and E_{scat} and E_{inc} are the scattered and incident electric fields, respectively. According to the position where these fields are measured, three cases are distinguished: backscattering (monostatic scattering), forward scattering and bistatic scattering [79]. The impinged object is usually referred as *scatterer*.

It is also understood from the previous equation that the RCS is a far-field parameter, where the magnitude of the electric field squared corresponds to the wave power. Therefore, it is also true that:

$$RCS = 4\pi d^2 \frac{P_{scat}}{P_{inc}} = 4\pi d^2 \frac{S_{scat}}{S_{inc}} = \frac{P_{scat}}{S_{inc}} \quad [\text{m}^2]; \tag{2.4}$$

where P and S refers to the radiated power [W] and the power density [W/m^2], respectively.

Since he scattered power from a scatterer is given by $P_{scat} = S_{inc}RCS$, the RCS must be interpreted as the equivalent area that intercepts the incident power density reaching an illuminated object, making this intercepted power equal to the backscattered power. That is the reason why the RCS is also referred as the echo area (Section 3.2 of [79]), and it is usually expressed in dBsm units which refer to the logarithmic scale referred to one square meter (dBsm = 10log(RCS [m^2])).

It is useful to understand the backscattering phenomena as a result of induced currents formed after the object illumination, which consequently generate radiating fields. From this point of view, every scatterer can be seen as an antenna whose radiating pattern depend on the magnitude and phase component of these currents [79]. When the

scatterer is intentionally conceived as an antenna, its RCS may have different components which depends both on the object shape and the antenna-related radiating characteristics. Thus, the RCS of an antenna can be considered as the combination of two components, the *antenna mode* and the *structural mode.*

Figure 2.2: Circuit model representation of a receiving antenna.
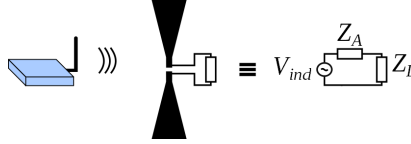
Source: The author.

As depicted in Fig. 2.2, assuming that the antenna have an electrical equivalent self-impedance Z_A Z_A and it is connected to a load impedance Z_L, the combination of the RCS modes can be expressed by

$$RCS = \left| \Gamma_A^* \sqrt{RCS_a} e^{j\Delta\phi} + \sqrt{RCS_s} \right|^2 , \qquad (2.5)$$

where RCS_a and RCS_r refer to the antenna and structural modes, respectively, $\Delta\phi$ is the relative phase difference between these modes, and $\Gamma_A^* = (Z_A^* - Z_L)/(Z_A + Z_L)$ is the complex reflection coefficient seen by the antenna toward the load.

The interpretation of both modes in (2.5) follows the well-diffused work of Green on antenna's RCS [80]. The antenna mode is a function of the radiation properties of the antenna, and is weighted by Γ_A^*. This is equivalent to a transmission line with a termination load when conjugated matching is ensured, that is, there is no wave reflection ($\Gamma_A^* = 0$). Thus, the RCS component due to the antenna load is null. However, one must recognize that at the conjugated matching condition, half of the collected power is delivered to the load ($\Re Z_L$) and half is dissipated by the antenna ($\Re Z_A$) as re-radiated power. The structural mode considers this re-radiated power plus the backscattered power due to surface-induced currents which depends on the complete antenna structure. Furthermore, it is important to emphasize that the structural mode is independent of the antenna load.

An equivalent expression of the total RCS in (2.5), at a fixed frequency, is given by[3]

---

[3]Refer to section 10 in [79] for further details

$$RCS = RCS_a(\phi, \theta) \left| A(\phi, \theta) + \Gamma_A^* \right|^2. \tag{2.6}$$

where A is a complex number related to the structural mode and is independent of the load impedance. Here, the RCS dependence on the azimuth (ϕ) and the elevation (θ) angles with respect to the illumination source was included in RCS_a and A. Those terms are also polarization dependent as well, even though it was not explicitly indicated.

Finally, as mentioned, the antenna-mode term of the RCS depends on the antenna radiation characteristics. This dependence is expressed as [81]

$$RCS_a(\phi, \theta) = \frac{\lambda^2}{4\pi} G^2(\phi, \theta), \tag{2.7}$$

where G is the antenna gain.

2.3   FIGURES OF MERIT OF CHIPLESS SENSORS

As already discussed, in frequency-mode frequency-coded (FMFC) chipless sensors, the backscattered EM waves are used to infer the RCS of the sensor as a function of frequency. The sensor is responsive to a particular stimulus from its surrounding environment because it includes in its fabrication a specific sensitive material whose electrical properties are dependent on the stimulus arising from the environment. These electrical properties, in the context of passive sensors, are basically divided into dielectric and conductive ones as depicted in Fig. 2.3.

On the one hand, dielectric properties, related to the electrical permittivity ($\varepsilon = \varepsilon' - j\varepsilon''$) of the sensitive material, have influence on the RF parameters of the sensor. Specifically, the real part of this electrical permittivity (ε') is directly linked to the resonance frequency of the sensor (f_{res}). For a specific design based on a wire-type antenna, this resonance frequency can be tracked from the RCS peak over the explored frequency range, since this peak occurs at resonance.

On the other hand, the electrical conductivity of the sensitive material (σ) have a direct impact on the maximum value of the RCS. The real part of the electrical permittivity (ε''), specially in very lossy dielectric materials, may also impact on this value.

As a result, both the resonance frequency and the radar cross section can be expressed as functions of the electrical permittivity and the conductivity of the sensitive material:

Figure 2.3: Working principle of chipless sensor due to the surrounding environment: Electrical interaction with the external stimulus causes changes to the sensor, which are monitored through its RCS and resonance frequency.
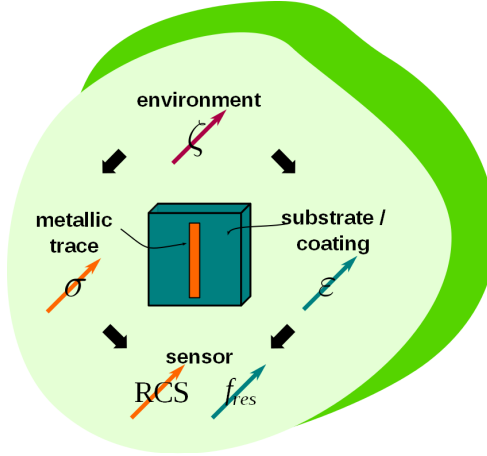
Source: The author.

$$f_{res} = F_1(\varepsilon'), \tag{2.8}$$

$$RCS_{(max)} = F_2(\sigma, \varepsilon''). \tag{2.9}$$

Based on these two relations, the sensor can be analyzed from two different, but equally critical, perspectives. The first is the sensor sensitivity, which, in this particular case, is related to how the resonance frequency changes with respect to a variation of the external stimulus. From a system point of view, this sensitivity must be high enough to satisfy the requirements of the chipless system. The second perspective is the radiation efficiency of the sensor, which is directly related to the maximum RCS of the sensor, and, as a consequence, determines the achievable reading range, as seen in Section 2.1. Both sensitivity and maximum RCS are discussed below.

2.3.1 Sensitivity

Frequency-coded chipless sensors are built with materials whose dielectric properties are sensitive to the monitored stimulus. Therefore,

the sensitivity of the chipless sensor can be calculated as the ratio of change of its output – in this case, the resonance frequency at which the RCS peak occurs– with respect to the change of the stimulus (measurand), which determines the sensor type. Hereon, this measurand will be referred in the following equations as ζ unless a particular stimulus (such as temperature, relative humidity, pressure, etc.) is specified.

If the sensor response is linear within the span of the measurand, the sensitivity can be calculated as the total variation in frequency due to the measurand variation. In a more general case, the sensitivity is defined as a partial derivative,

$$
\begin{aligned}
S &= \lim_{\Delta\zeta \to 0} \frac{\Delta f_{res}}{\Delta\zeta}, \\
&= \frac{\delta f_{res}}{\delta\zeta},
\end{aligned}
\tag{2.10}
$$

which is evaluated at a particular value within its variation range. The definition in (2.10) is also referred as *absolute sensitivity*. Alternatively, to be able to compare different sensors that operate at different frequencies and materials, it is also useful to calculate the *relative sensitivity* from the relative rate of change of each parameter:

$$
\begin{aligned}
S_\zeta^{f_{res}} &= \lim_{\Delta\zeta \to 0} \frac{(\Delta f_{res}/f)}{(\Delta\zeta/\zeta)}, \\
&= \frac{\delta f_{res}}{\delta\zeta} \frac{\zeta}{f_{res}}.
\end{aligned}
\tag{2.11}
$$

The sensitivity is an important figure of merit of a specific sensor as it can be used to measure its total *responsivity*. For instance, if the responsivity is to be evaluated within a the measurand span, then it is valid to consider that the total frequency shift can be expressed as infinite series of terms around the initial point of change ($\zeta = \zeta_0, f_{res} = f_{res0}$):

$$
\begin{aligned}
\Delta f_{res} &= \sum_{n=1}^{\infty} \frac{f_{res}^{(n)}}{n!}(\Delta\zeta)^n, \\
&= (\Delta\zeta) \left.\frac{\delta f_{res}}{\delta\zeta}\right|_{\zeta_0} + \frac{(\Delta\zeta)^2}{2} \left.\frac{\delta^2 f_{res}}{\delta\zeta^2}\right|_{\zeta_0} + ...,
\end{aligned}
\tag{2.12}
$$

where $\Delta f_{res} = f_{res} - f_{res0}$ and $\Delta\zeta = \zeta - \zeta_0$.

For small changes in ζ, only the first term in (2.12) may be considered. Thus, using the expression of the sensitivity in (2.11), the total relative change in the resonance frequency can be approximated as:

$$\frac{\Delta f_{res}}{f_{res0}} \approx \frac{\Delta \zeta}{\zeta_0} \left. S_\zeta^{f_{res}} \right|_{\zeta_0}. \tag{2.13}$$

It is also important to notice that since the variation of the equivalent effective electrical permittivity of the sensitive material in the sensor changes due to the measurand, then the expression of the resonance frequency shift can also be expressed in terms of the change of the permittivity. Defining ε_e as the real part of the equivalent effective electrical permittivity, by considering that $\Delta \varepsilon_e \approx \Delta \zeta \frac{\delta \varepsilon_e}{\delta \zeta}$, then, (2.12) can be also expressed as

$$\Delta f_{res} = (\Delta \varepsilon_e) \left. \frac{\delta f_{res}}{\delta \varepsilon_e} \right|_{\varepsilon_{e0}} + \frac{(\Delta \varepsilon_e)^2}{2} \left. \frac{\delta^2 f_{res}}{\delta \varepsilon_e^2} \right|_{\varepsilon_{e0}} + ..., \tag{2.14}$$

which resembles the relation established in (2.8). Finally, by approximating it to the first term and using the definition of relative sensitivity, (2.14) can be rewritten as

$$\frac{\Delta f_{res}}{f_{res0}} \approx \frac{\Delta \varepsilon_e}{\varepsilon_{e0}} \left. S_{\varepsilon_e}^{f_{res}} \right|_{\varepsilon_{e0}}. \tag{2.15}$$

Differently than (2.12) and (2.13), expressions (2.14) and (2.15) present the sensitivity of the sensor in terms of the effective electrical permittivity of the sensitive material. This expression is useful as the sensor output can be analyzed only as a function of its building materials and then combine these results with the response of the sensitizing material to the particular measurand.

As a conclusion, from a design perspective, the total resonance frequency shift must be specified. Therefore, estimating $S_{\bar{\varepsilon}}^{f_{res}}$ from the sensor structure and materials is required.

2.3.2 Maximum RCS

Recalling (2.6), the RCS depends on the radiation characteristics of the sensor, so a careful design should be considered to maintain both compactness and proper radiation. Even though not as evident as in

the case of RT chipless tags, EP-based chipless sensors can also be divided and analyzed considering two different elements, the radiator and the transducer, which are physically combined into a single compact structure. Based on the representation of Fig. 2.2, the transducer can be modeled either as part of the antenna or as the antenna load.

In the particular case of wire-type antennas, such as a half-wave dipole, the structural-mode term in (2.6) approximates unity ($A \approx 1$) [81], which can be understood as the structural mode given only by the re-radiated power from the antenna's impedance. In this case, we have that

$$RCS^n = \frac{\eta^2 D^2}{4\pi} \left| 1 + \Gamma_A^* \right|^2, \tag{2.16}$$

where $RCS^n = RCS/\lambda^2$ is the normalized RCS (with respect to the wavelength squared), and the gain definition of an antenna given in (2.17) has been used.

$$G(\phi, \theta) = \eta D(\phi, \theta). \tag{2.17}$$

Herein, η is the radiation efficiency and D is the antenna directivity.

It is important to note that (2.17) is evaluated at an specific frequency. As a result, it can be concluded from (2.16) that the RCS of an antenna at a given frequency is dependent on three parameters: η, D, and Γ_A^*.

Recalling Fig. 2.2, it can also be obtained that

$$\begin{aligned} RCS^n &= \frac{\eta^2 D^2}{4\pi} \left| \frac{2R_A}{Z_A + Z_L} \right|^2, \\ &= \frac{\eta^2 D^2}{\pi} \left(\frac{R_A^2}{(R_A + R_L)^2 + (X_A + X_L)^2} \right), \end{aligned} \tag{2.18}$$

where $R_A = \Re Z_A$, $X_A = \Im Z_A$, $R_L = \Re Z_L$, and $X_L = \Re Z_L$. It is evident that evaluating (2.18) at resonance ($X_A + X_L = 0$) leads to the maximum RCS.

From the definition of *radiation efficiency* [77],

$$\eta = \frac{R_r}{R_A} = \frac{R_r}{R_r + R_l}, \tag{2.19}$$

where R_r and R_l are the radiation and loss equivalent resistances of the antenna. Finally, from (2.18), at resonance, the following expression for the maximum (normalized) RCS is obtained:

$$RCS^n_{(max)} = \left(\frac{R_r}{R_r + R_l + R_L}\right)^2 \frac{D^2}{\pi}, \tag{2.20}$$

It can be noticed that the RCS maximum value is dependent on the relation between R_r and $R_l + R_L$. This value is maximized for a shorted load ($Z_L = 0$) and for $R_r \gg R_l$. As a conclusion, it is desirable to design the chipless sensor so that its radiation properties keep R_r and D as high as possible. The former is indeed more important from the design perspective if omnidirectional antenna-based scatterers are considered since D can be assumed constant. Moreover, it is important to remark that the electrical conductivity and the dielectric losses of the materials used for implementing the sensor will impact on R_l and, depending on the load, on R_L as well.

Finally, it is often the case that the interrogated antenna is shorted, meaning that there is no load connected to the antenna terminals ($Z_L = 0$).[4] Therefore, (2.20) can be re-expressed as

$$RCS^n_{(max)} = \frac{\eta^2 D^2}{\pi}, \tag{2.21}$$

2.3.3 Quality factor and bandwidth

From (2.21), (2.16) can also be written as:

$$
\begin{aligned}
RCS^n &= \frac{RCS^n_{(max)} \left|1 + Z_A^*/Z_A\right|^2}{4}, \\
&= \frac{RCS^n_{(max)}}{1 + (X_A/R_A)^2}.
\end{aligned}
\tag{2.22}
$$

If a series-LC network, formed by an equivalent inductance L_A and capacitance C_A, is considered to model the antenna self-impedance around its resonance frequency (ω_A), then $X_A = \omega L_A - 1/\omega C_A = \omega L_A(1 - \omega_A^2/\omega^2)$. Thus, (2.22) can also be written as

$$RCS^n = \frac{RCS^n_{(max)}}{1 + [Q_A(\omega/\omega_A - \omega_A/\omega)]^2}. \tag{2.23}$$

where $Q_A = \omega_A L_A/R_A = 1/(\omega_A C_A R_A)$ is the quality factor of the series-LC network [83].

---

[4]If there is a load, a shorted antenna can be still considered modeling the load as part of the antenna.

When the sensor is interrogated, the reader sweeps the frequency of the transmitted wave and tracks the frequency at which the maximum reflection occurs. It is important to predict the sharpness of this peak since it is related to its selectivity, that is, to how much frequency band is needed to accurately detect this peak. Evaluating the RCS around its resonance, so $\omega = \omega_A + \Delta\omega$, and considering $\Delta\omega << \omega_A$ in (2.23), it can be derived that:

$$RCS^n = \frac{RCS^n_{(max)}}{1 + (2Q_A \Delta\omega/\omega_A)^2}.$$
(2.24)

From this expression, the quality factor Q_A may also be defined as the ratio of the resonance frequency and the twice the frequency offset at which the RCS decays in $3\,\mathrm{dB}$, so:

$$Q_A = \frac{\omega_A}{2\Delta\omega_{3dB}}.$$
(2.25)

As a result, the quality factor of the antenna can be related to the $3\,\mathrm{dB}$ bandwidth of the RCS frequency response.

2.4 RADIATION EFFICIENCY IN MINIATURIZED DIPOLE-BASED ANTENNAS

Since wire-type antennas served as the basis for construction of the miniaturized scatterer of the sensor, it is convenient to start the analysis on the radiation properties of the most basic example of these type of antenna: the small dipole. Consider the dipole of length l illustrated in Fig. 2.4(a). When $\lambda/50 < l < \lambda/10$, where λ is the wavelength, the dipole is said to be small, and its radiation resistance can be calculated through [77]

$$R_{r(\text{small dipole})} = 20\pi^2 \left(\frac{l}{\lambda}\right)^2.$$
(2.26)

As noticed, its radiation resistance, and so its radiation efficiency, is dependent on the ratio l/λ, that is, the normalized dipole length over the wavelength. Typically, small antennas' radiation characteristics are mainly determined by its electrical and magnetic dipole moments [82]. Therefore, any other small antenna which follows a similar behavior of a dipole at its operating frequency is expected to present the same dependence on its normalized length.

Figure 2.4: Representation of a (a) thin-wire dipole antenna (of total length l) and a (b) circular meandered dipole (with radius r_s and slit angle ϕ_s antenna).

(a)   (b)
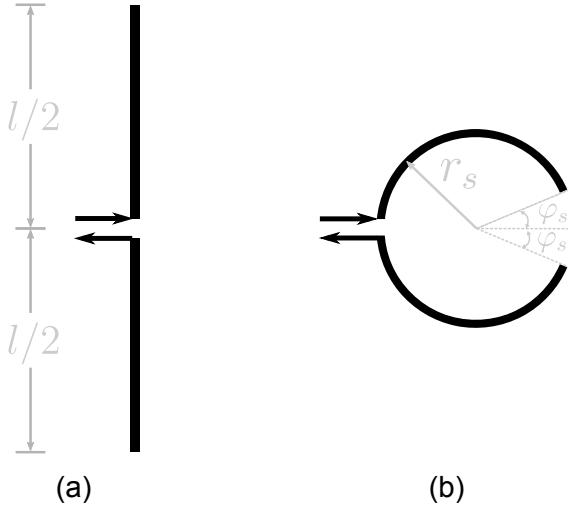
Source: The author.

For instance, let us consider the circular meandered dipole in Fig. 2.4(b). Since only one meander is assumed in this analysis, this structure is also referred along this document as the circular Open Ring Resonator (ORR). As demonstrated in Section A.1 of the Appendix, its radiation resistance may be calculated from its dipole moment, thus it can also be written as a function of its normalized total length. Since the circular shape of the ORR is better described by its radius, from (A.11), the radiation resistance of the circular ORR can be approximately expressed as

$$R_{r(\text{circular ORR})} = 1580 \left(\frac{r_s}{\lambda}\right)^2 \alpha_s^2, \qquad (2.27)$$

where r_s is the ORR radius and α_s is a factor that depends on the slit angle φ_s (shown in the figure).

As demonstrated in the Appendix, regarding the approximate resonance condition as the total length being equal to half-wavelength, then $2\pi r_s = 2k_s(\lambda/2)$, where $k_s = \frac{\pi}{2(\pi-\varphi_s)}$ accounts for the length reduction due to the slit, the following expression can be also used for the ORR radiation resistance:

Figure 2.5: Numerical evaluation from (2.28) of the radiation resistance of a circular ORR at resonance as a function of the slit angle and calculation of the radiation efficiency considering ohmic losses in conductive traces (width = 1 mm, height = $35\,\mu$ m) for two different values of electrical conductivities at different radius.
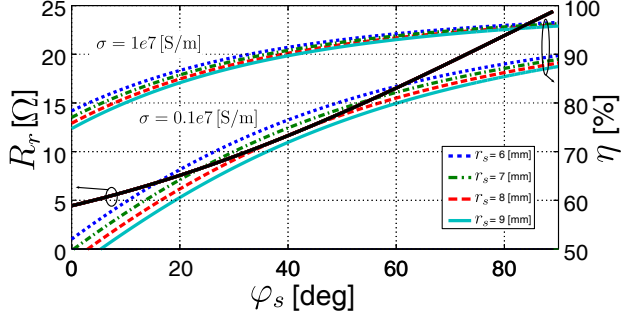
Source: The author.

$$R_{r(\text{circular ORR})} = 40\left(\frac{k_s^2\cos\left(\pi - \varphi_s\right)}{k_s^2 - 1}\right)^2. \tag{2.28}$$

Hence, it can be noticed that, at resonance, the radiation resistance of the circular ORR depends exclusively on the slit angle. A numerical evaluation of (2.28) is shown in Fig. 2.5 where this fact is evidenced. As φ_s increases from 0 to 90°, the radiation resistance increases from approximately 5 to 25 Ω. This is expected since as the slit increases, the ORR approximates a thin half-wave dipole which presents an approximate radiation resistance of 73 Ω [77].

In the same plot, the calculus of the radiation efficiency (η) of the ORR considering the conductor ohmic losses has also been included. The effect on the slit angle on the radiation efficiency is observed, which is more significant for low conductivity metals. For an electrical conductivity of 1×10^7 [S/m], the efficiency varies from approximately 80% to 95%, while for a conductivity ten times lower, the efficiency goes down to 50% and reaches almost 90%. Therefore, a considerable impact is expected when using higher slit angles specially with lossy conductors. Note that only ohmic and no dielectric losses have been considered for this efficiency estimation. Finally, it can also be noticed that, differently from the radiation resistance, the radiation efficiency presents a small dependence on the ORR radius.

The theoretical expression above is useful to predict the perfor-

mance of practical chipless sensors whose scattering characteristics are based on dipole-like small antennas. For instance, consider the squared version of the ORR shown in Fig. 2.6(a). Here, a copper-etched and a FR-4 substrate is considered, which is a common material used for low-cost electronics implementations. In this structure, the slit length of the ring (s_o) can be used for adjusting the resonance frequency (f_o) for a given lateral length (l_o). Some values for these lengths have been selected to include the 2.4 MHz ISM band as observed from EM simulation results shown in Fig. 2.6(b). Moreover, it is important to notice that increasing the slit length and keeping fixed the lateral length in the squared ORR is equivalent to increasing the slit angle of the circular ORR. Thus, analogously to what was predicted before, it is expected that its radiation resistance increases proportionally to the ratio s_o/l_o. This is verified in 2.6(c), where the simulated results of the radiation efficiency are shown as a function of s_o/l_o at several lateral length dimensions. These results present similar behavior as the ones in Fig. 2.5, where the radiation efficiency increases with s_o/l_o, i.e., the slit angle.

Figure 2.6: (a) Squared ORR and its (b) resonance frequency and (c) radiation efficiency as a function of the lateral length (l_o) and slit (s_o) dimensions, extracted from EM simulations with method of moments of the ORR self-impedance in a FR4 substrate ($h = 1.6\,\mathrm{mm}, \varepsilon_r = 4.1, \tan\delta = 0.017$).
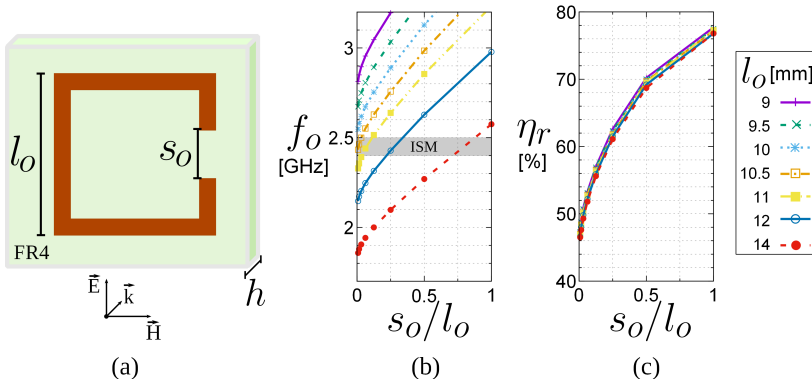
Source: The author.

From the previous results it can be concluded that to increase the radiation efficiency of a ORR, the ring slit should be maximum. However, to keep a fixed operating frequency, this implies increasing its

total length and consequently the total occupied area. Therefore, it is also evident that an inherent trade-off between radiation efficiency and size exists. Both variables should be evaluated according to the system requirements.

2.5   SPLIT-RING RESONATOR

The *Split-Ring Resonator* or SRR is a structure that became well-known after the work of Pendry et al. [84] in which the authors described how an array of SRRs could be used for the implementation of negative-permeability artificial media. Moreover, when combined with other structures array, this array could be used for synthesizing artificial metamaterials [85].

Even though there are many variants on the SRR physical configuration and ring shapes [86], its basic format consists of two concentric metallic rings with slits on opposite sides, as shown in Fig. 2.7(a) [87]. Non-magnetic metals are used for the rings and these are usually etched on a dielectric substrate.

Figure 2.7: Split-ring resonator (a) basic structure and (b) charge distribution when excited.
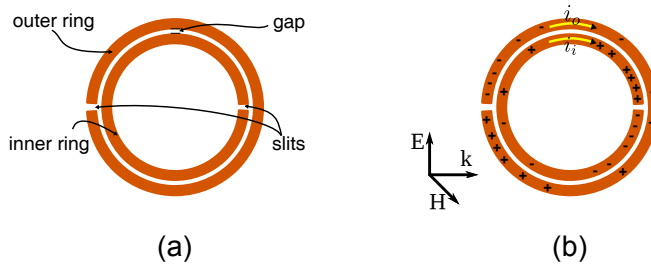
Source: The author.

When the SRR is excited by a time-varying magnetic field perpendicular to its surface, an electrical current is induced along its rings as illustrated in Fig. 2.7(b). At a specific excitation frequency, referred as the SRR fundamental or first resonance frequency, the current distribution is characterized by having minimum values near the slits and maximum on the opposite sides. This originates the accumulation of opposite charges between the rings, so a high capacitance distributed along the structure is attributed, specially when the rings are strongly

coupled [87]. The high capacitance value causes the SRR to resonate at a much lower frequency than the one corresponding to its physical length. This makes of it a very compact structure, which has also been explored in the construction of electrically small antennas [88, 89, 90].

As analyzed in [91], the radiation resistance is very low at the fundamental resonance compared to higher order resonances modes.[5] This means that its use as an antenna may no be convenient at its first resonance. Consequently, this structure has been rather explored in the construction of high quality filters [85].

Excitation of the SRR fundamental resonance may be achieved either by a time-varying perpendicular magnetic field or by a electrical field parallel to the slits [92]. At this resonance, the SRR can be analyzed using a quasi-static approximation, and thus, it can be modeled with an LC tank, whose elements can be calculated from the rings dimensions [93].

All of the above mentioned features of the SRR can be also explored in the integration of uniplanar miniaturized backscattering based sensors in which high sensitivity is required and where specific radiation properties should be well understood.

---

[5]In [88], the authors deduced both electrical and magnetic dipole moments at first resonance, being the magnetic moment the most significant. However, the associated radiation resistance due to this dipole moment is still an order of magnitude lower compared to the radiation resistance at the second resonance.

3 NOVEL MINIATURIZED CHIPLESS SENSOR

In this chapter a new structure for miniaturized chipless sensors based on magnetically coupled sensitized resonator is proposed. First, the concept of the sensor structure is described and its advantages to other approaches used in miniaturized chipless sensors are highlighted. After this, an electrical model is presented from which theoretical expressions of the critical figures of merit are derived. Moreover, numerical evaluation of each of this figures of merit are done. Finally, it is evidenced how the analysis based on this model helped in the understanding of the sensor and served as a general guideline for the sensor design.

3.1 SENSOR CONCEPT

Reported uniplanar chipless sensors follow two general approaches. The first is based on TL which are coupled to resonators, hereon referred as *sensitized resonators* given their responsivity to the desired monitored parameter. [66]. The typical implementation of this type of sensors is illustrated in Fig. 3.1(a). Here, a TL is connected to two cross polarized antennas at both ends, as it is done in retransmission-based tags [57]. To operate as a chipless sensor, a resonator is included along the TL where the received signal passes through. Thus, its RCS presents a valley (local minimum) at the same frequency of the resonator's resonance frequency. The sensitized resonator is designed to be responsive to a specific stimulus, usually through its equivalent capacitance, so the monitored information can be obtained by tracking the frequency shift of the RCS's valley. This approach is very suitable for large reading distances, since the reception of the incoming wave and its re-transmission relies on cross-polarized antennas, which improves the readability of the sensor. Nonetheless, the fact that the antennas are designed as a separated part of the sensing element makes this approach unsuitable for miniaturized structures at the frequencies of interest of this work. Single metallic layer structures are achieved by using Coplanar Wave Guide (CPW) TLs [66].

Aiming at miniaturization of the sensor, the next approach uses EP-based designs [32, 39, 47, 67, 104]. In this approach, the scatterer is usually based on a shorted dipole-like antenna, which presents a RCS

Figure 3.1: Different approaches for chipless sensors: on the left, the retransmission-based tag with a resonator as a filter, the capacitive approach with a miniaturized dipole-like scatterer with parallel capacitance; on the right, the proposed approach based on a magnetically coupled resonator.

TL plus resonator

(a)

capacitive

(b)

mag. coupled resonator

(c)
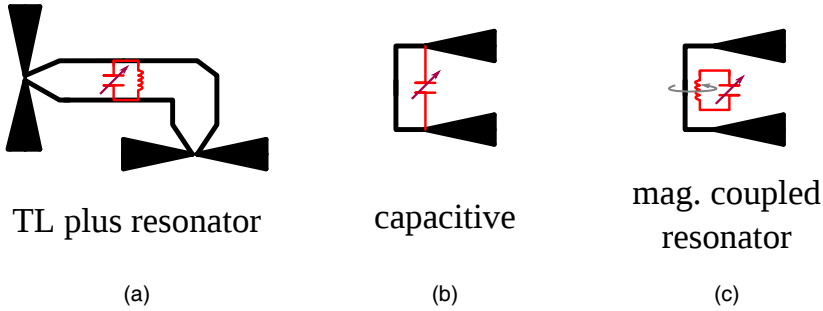
Source: The author.

peak at its resonance frequency.[1] As shown in Fig. 3.1(b), a capacitive transducer is included whose construction is facilitated by the folding of the dipole, taking advantage of the proximity of the antennas endpoints [39]. Therefore, similar as in the first approach, frequency coding can be used, however, this time, not by tracking the RCS's valley but peak. It should be noticed that this approach establishes an inherent trade-off between the sensor's radiation performance, size, and sensitivity, in the sense that, to increase the sensitivity, the capacitance needs to be large, which is directly related with reducing the size of the sensor. Consequently, there is also a reduction of the radiation efficiency, as discussed in Section 2.4.

In this work, a third approach is proposed for miniaturized chipless sensors, whose concept is depicted in Fig. 3.1(c). The scatterer is also based on a shorted folded-dipole antenna. However, an LC tank, built from a capacitive transducer and an inductor, is magnetically (inductively) coupled to the main scatterer. The tank is a sensitized resonator, since the capacitive transducer changes its resonance frequency as an external stimulus varies.

Differently from the previous approaches, two advantages can be envisaged. First, the sensitivity is not strongly tied to the radiation

---

[1]Resonators based on slots are another type of EP-based sensors but they were not included in this review since they relay on larger areas of metallic traces, leading to higher fabrication costs.

efficiency since the transducer capacitance does not depend on the scatterer shape. Second, for a given specification of maximum occupied area, the scatterer size can be adjusted to maximize the radiation performance of the sensor. In the case of the capacitive approach, this is not possible since increasing the radiation efficiency implies reducing the capacitances which degrades the sensitivity.

It should be mentioned that inductively-coupled resonators have been intensively studied in the context of wireless power transfer. The coupling between the antennas and resonators have been also analyzed in the context of RFID tags [94]. However, inductively-coupling between a resonator and a main scattering structure has not been yet studied in the context of miniaturized chipless sensors.

Considering the idea of the proposed sensor, it is expected that the resonance frequency, that is, the frequency at which the RCS peak occurs, depends on the efficiency of the magnetic coupling and on its own resonance frequency. Moreover, it is of utmost relevance to understand how sensitive is the structure upon those parameters. To be able to estimate the response of the sensor, which in turn determines the overall sensor performance, an analysis based on the electrical model of the sensor is proposed. This model is helpful for predicting the impact of each of the sensor design variables and formulate a general design flow of the sensor. However, before presenting the cited model, an early prediction of the effect of the resonating coupling in the scatter may be done at this point.

Let us assume that the chipless reader sends a CW whose frequency equals the intrinsic resonance frequency of the scatterer. If the scatterer were coupled to the resonator, and the resonator's resonance frequency were lower than the one of the scatterer, the resonator would behave mostly inductive at that reading frequency. To the scatterer, this would be equivalent to have a shorted inductor, thus, causing a decrease of the magnetic flow around it and reducing the total inductance (self-inductance plus mutual inductance). Therefore, this would result in a new shifted resonance frequency (of the whole structure) higher than that of the scatterer. The new resonance frequency value would be such that the total inductance were equal the self-capacitance of the scatterer.

The contrary would be expected at frequencies below the resonator's resonance. In this case, the LC tank would be more capacitive, producing a magnetic flow that enhances the one of the scatterer, thus, increasing the total inductance. Then, the new resonant frequency would be shifted to a lower value.

As a conclusion, it can be expected that by coupling a resonator, the value of its resonance frequency determines the resultant resonance frequency of the sensor, at which the RCS peak occurs. If the resonator is sensitized, making its resonance frequency to vary with the parameter to be monitored, the resonance frequency of the sensor will vary as well. The initial relation between the resonance frequency of the scatterer and the sensitized resonator, and the magnitude and sign of the rate of change of the sensitized with respect of the monitored parameter will determine the direction and rate of change of the sensor's resonance frequency.

3.2   EQUIVALENT ELECTRICAL MODEL

The proposed sensor structure consists of a resonant scatterer inspired on a meandered half-wave dipole coupled to a sensitized resonator. This concept is illustrated in Fig. 3.2(a), where the scatterer is represented by the ORR and the resonator by a LC tank. The responsiveness of the resonator to the desired stimulus is represented by a variable capacitor.

Assuming that a vertically polarized plane wave impinges the sensor, as shown in the figure, the self impedance is equivalent to the input impedance measured at the center of the scatterer. This impedance is represented by Z_A in Fig. 3.2(b). By modeling the scatterer, the sensitized resonator, and their interaction through the magnetic coupling, an expression to Z_A can be obtained and, from it, the response of the sensor can be further estimated.

An equivalent lumped-circuit model of the structure is shown in Fig. 3.3(a). Here, both the ORR and the sensitized resonator are modeled as two magnetically coupled lossy LC series resonators. The ORR and the sensitized resonator were divided into two equal parts resembling their symmetric structures. It should be also mentioned that modeling the ORR with an LC tank is consistent if the sensor is expected to operate around the ORR first resonance, that is, near the half-wavelength condition.

The model can be further simplified to the one shown in Fig. 3.3(b). The scatterer is reduced to a series resonator with an impedance given by

Figure 3.2: (a) Idea of the proposed sensor: an ORR magnetically coupled to a sensitized resonator and (b) its equivalent self-impedance.

(a)   (b)
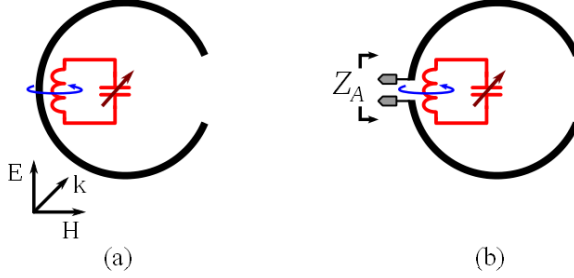
Source: The author.

Figure 3.3: Circuit model of the proposed sensor.

(a)   (b)   (c)   (d)
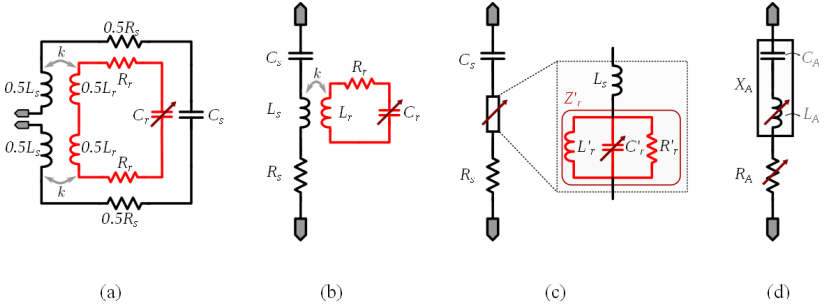
Source: The author.

$$Z_s = R_s + j\omega L_s + \frac{1}{j\omega C_s},$$
$$= R_s + j\omega L_s \left(1 - \frac{\omega_s^2}{\omega^2}\right),$$

(3.1)

where R_s, L_s and C_s represent the correspondent resistance, inductance, and capacitance, which values were considered independent of the frequency, and $\omega_s = \sqrt{(L_s C_s)}^{-1}$ is the fundamental angular resonance frequency of the scatterer at which the total impedance reduces to R_s. The real and imaginary parts of the scatterer impedance can be expressed separately as

$$\Re(Z_s) = R_s = \frac{\omega_s L_s}{Q_s}, \tag{3.2}$$

and

$$\Im(Z_s) = -\omega L_s \left(\frac{\omega_s^2}{\omega^2} - 1 \right), \tag{3.3}$$

where $Q_s = \omega_s L_s / R_s$ is the scatterer quality factor from the definition of a series-LC network [83]. Notice that the imaginary part is negative for $\omega < \omega_s$, so a capacitive behavior is predominant at low frequencies. When $\omega > \omega_s$, the imaginary part becomes positive and the inductive behavior prevails.

Similarly, the sensitized resonator can be modeled as a lossy series LC resonator around its fundamental frequency, with an impedance given by:

$$\begin{aligned} Z_r &= R_r + j\omega L_r + \frac{1}{j\omega C_r}, \\ &= R_r + j\omega L_r \left(1 - \frac{\omega_r^2}{\omega^2} \right), \end{aligned} \tag{3.4}$$

were $\omega_r = \sqrt{(L_r C_r)}^{-1}$ is the fundamental angular resonance frequency. Also, the real and imaginary parts of the impedance can be expressed separately as

$$\Re(Z_r) = R_r = \frac{\omega L_r}{Q_r}, \tag{3.5}$$

and

$$\Im(Z_r) = -\omega L_r \left(\frac{\omega_r^2}{\omega^2} - 1 \right), \tag{3.6}$$

where $Q_r = \omega_r L_r / R_r$ is the resonator quality factor.

Both series resonators are magnetically coupled through its inductive components, which is represented by the magnetic coupling coefficient k. By equating the induced current and voltage relations after this coupling, the effect of the sensitized resonator can be reflected at the scatterer. It can be demonstrated that this reflected impedance is given by

$$\begin{aligned} Z_r' &= \frac{(\omega M)^2}{Z_r}, \\ &= \frac{(\omega M)^2}{j\omega L_r + \frac{1}{j\omega C_r} + R_r}, \end{aligned} \tag{3.7}$$

where $M = k\sqrt{L_s L_r}$ is the mutual inductance between inductors L_r and L_s. An alternative expression of the reflected impedance may help to gain insight of the effect of the coupling. By re-expressing (3.7) as in (3.8), it can be seen that this impedance can be interpreted as a parallel resonator as shown in Fig. 3.3(c), whose equivalent inductance, capacitance, and resistance are given by (3.9), (3.10), and (3.11), respectively, and which resonates at the same frequency as the sensitized resonator (ω_r) [85].

$$Z_r' = \frac{1}{\frac{1}{j\omega L_r'} + j\omega C_r' + \frac{1}{R_r'}}, \qquad (3.8)$$

$$L_r' = C_r(\omega M)^2, \qquad (3.9)$$

$$C_r' = \frac{L_r}{(\omega M)^2}, \qquad (3.10)$$

$$R_r' = \frac{(\omega M)^2}{R_r}. \qquad (3.11)$$

At frequencies below resonance, the inductive behavior of the resonator prevails, so the total inductance increases as L_s sees an additional inductance in series. Conversely, at frequencies above resonance the capacitive behavior prevails, and C_s sees a series capacitor which reduces the total capacitance. These results are in accordance with the predictions made at the end of the previous subsection.

Rearranging the terms in (3.7), the real and imaginary parts of the reflected impedance can be also expressed, separately, as

$$\Re(Z_r') = \omega L_s k^2 \left(\frac{\omega_r/(\omega Q_r)}{\omega_r^2/(\omega^2 Q_r^2) + (1 - \omega_r^2/\omega^2)^2} \right), \qquad (3.12)$$

and

$$\Im(Z_r') = -\omega L_s k^2 \left(\frac{1 - \omega_r^2/\omega^2}{\omega_r^2/(\omega^2 Q_r^2) + (1 - \omega_r^2/\omega^2)^2} \right). \qquad (3.13)$$

Finally, the resultant self-impedance of the whole structure, represented in 3.3(d), can be calculated. From (3.2) and (3.12), the real part, $\Re(Z_A) = R_A$, results in

$$R_A(\omega) = \Re(Z_s) + \Re(Z_r'),$$

$$= R_s + \omega L_s k^2 \left(\frac{\omega_r/(\omega Q_r)}{\omega_r^2/(\omega^2 Q_r^2) + (1 - \omega_r^2/\omega^2)^2} \right). \qquad (3.14)$$

Therefore, it can be stated that the real part of the sensor is the sum of a fixed component, which value is determined by the scatterer resistance, plus another extra component which depends on the frequency and the parameters of the sensitized resonator (Q_r and ω_r), as well as on the coupling factor (k).[2] Evaluating (3.14) at lower frequencies with respect to the resonance of the sensitized resonator ($\omega \ll \omega_r$), the effect of the extra component is reduced and the value of R_A tends to R_s.

It is also interesting to examine (3.14) near the resonance of the sensitized resonator. By using using a Taylor series expansion around $\omega = \omega_r$, it can be obtained that:

$$R_A(\omega) \approx R_s + R_r' \left(1 - 4Q_r^2 \left(1 - \omega/\omega_r\right)^2\right) + \dots \quad , \qquad (3.15)$$

where R_r' is given by (3.11) evaluated at ω_r. From this result, it can be seen that the effect of the coupled resonator is an increment of the real part. This value reaches its peak value at $\omega = \omega_r$, where $R_A \approx R_s + R_r'$. The same result can be also obtained from (3.14).

In addition to this, from (3.3) and (3.13), the imaginary part, $\Im(Z_A) = X_A$, results in:

$$\begin{aligned}
X_A &= \Im(Z_s) + \Im(Z_r') \\
&= \left(\omega L_s - \frac{1}{\omega C_s}\right) - \omega L_s k^2 \left(\frac{1 - \omega_r^2/\omega^2}{\omega_r^2/(\omega^2 Q_r^2) + (1 - \omega_r^2/\omega^2)^2}\right) \\
&= \omega L_A - \frac{1}{\omega C_A},
\end{aligned}$$
$$(3.16)$$

where the resultant capacitance equals the intrinsic capacitance of the scatterer ($C_A = C_s$), and the total inductance is expressed by

$$L_A(\omega) = L_s \left(1 + \frac{k^2 \left(\omega_r^2/\omega^2 - 1\right)}{\omega_r^2/(\omega^2 Q_r^2) + (1 - \omega_r^2/\omega^2)^2}\right). \qquad (3.17)$$

This value tends to L_s when evaluating it at lower frequencies far from the resonance frequency of the sensitized resonator.

Finally, as with the real part, (3.17) can be examined near ω_r. Then,

---

[2]Since the capacitive transducer is responsive to the external stimulus, then ω_r changes with it and so will R_A. This effect is illustrated in the figure with a variable resistor.

$$L_A(\omega) \approx L_s \left(1 + 2k^2 Q_r^2 \left(1 - \omega/\omega_r\right)\right) + ... \quad . \tag{3.18}$$

When $\omega < \omega_r$, the inductance of the sensor increases, and vice-versa. The ratio of change around ω_r depends on a weighting factor determined by the product kQ_r squared. Also, it is seen that at $\omega \approx \omega_r$, the antenna inductance remains equal to the scatterer inductance ($L_A = L_s$). This result is consistent, since the reactance of the sensitized resonator is null at its resonance. The same can also be obtained from (3.17).

3.2.1 Resonant frequency of the sensor

The main figure of merits of the sensor, such as the peak RCS and its sensitivity, are to be evaluated at the resonance frequency of the sensor. Therefore, it is of utmost importance to estimate the resonance frequency of the structure from the electrical model.

As demonstrated before, the resonator coupling changes the equivalent inductance, or, equivalently, the total reactance of the self-impedance of the sensor. As a result, it is expected that the resonant frequency of the sensor changes as well. The resultant resonance frequency of the sensor, referred as f_A ($f_A = \omega_A/2\pi$), can be found by solving $X_A = 0$ for the variable ω. From (3.16), it follows that:

$$0 = \left(1 - \omega_s^2/\omega^2\right) + \frac{k^2 \left(\omega_r^2/\omega^2 - 1\right)}{\omega_r^2/(\omega^2 Q_r^2) + \left(\omega_r^2/\omega^2 - 1\right)^2}. \tag{3.19}$$

Expanding this equation, the sixth-order polynomial in (3.20) is obtained, where the coefficients A, B, C, and D are given by (3.21)–(3.24). Since there are no terms with even exponential in (3.20), the solution can be calculated as in a cubic equation instead, whose general solution is known. From the three roots obtained, the desired solution (ω_A) corresponds to the square root of the one that is less than unity, as this is the one that would represent the resonance frequency of the sensor.[3]

$$0 = A\omega^6 + B\omega^4 + C\omega^2 + D, \tag{3.20}$$

$$A = 1 - k^2, \tag{3.21}$$

---

[3]If $\omega_r > \omega_s$.

$$B = \omega_r^2 \left(k^2 - 2 + \frac{1}{Q_r^2} \right) - \omega_s^2, \tag{3.22}$$

$$C = \omega_r^2 \left(2\omega_s^2 + \omega_r^2 \left(1 - \frac{1}{Q_r^2} \right) \right), \tag{3.23}$$

$$D = -\omega_s^2 \omega_r^4. \tag{3.24}$$

As a result of the solution of the third-degree polynomial, the resonance frequency can be expressed in terms of a function that depends on the scatterer and resonator parameters:

$$\omega_A = F \left(\omega_s, \omega_r, Q_r, k \right). \tag{3.25}$$

Looking forward a more intuitive analysis of the sensor, it was convenient to re-express (3.20) by using a normalized frequency as the variable. For this purpose, the scatterer resonance frequency was chosen, so the new variable of the equation ω_n ($\omega_n = \omega/\omega_s$) was used. Making this substitution leads to the expressions in (3.26)–(3.30), where β is the normalized resonance frequency of the sensitized resonator ($\beta = \omega_r/\omega_s = f_r/f_s$). The solution to this equation corresponded, this time, to the normalized resonance frequency α ($\alpha = \omega_A/\omega_s = f_A/f_s$), and was found in the same manner than in (3.20). Expressing the problem in terms of normalized frequencies allows evaluating of all the parameters that influence on the sensor resonance independently of the value of the operating frequency.

$$0 = A'\omega_n^6 + B'\omega_n^4 + C'\omega_n^2 + D', \tag{3.26}$$

$$A' = A, \tag{3.27}$$

$$B' = \beta^2 \left(k^2 - 2 + \frac{1}{Q_r^2} \right) - 1, \tag{3.28}$$

$$C' = \beta^2 \left(2 + \beta^2 \left(1 - \frac{1}{Q_r^2} \right) \right), \tag{3.29}$$

$$D' = -\beta^4. \tag{3.30}$$

Finally, (3.25) can also be written as

$$\alpha = \frac{f_A}{f_s} = G \left(\beta, Q_r, k \right), \tag{3.31}$$

where G is an analytical function which depends on β, Q_r, and k.

An example of the evaluation of the results from (3.31) is shown in Fig. 3.4(a). The horizontal axis refers to the normalized sensitized resonator resonance frequency (β) and the vertical axis refers to the normalized resonance frequency of the sensor (α) found from the roots solution. Also, a fixed value of $Q_r = 100$ and four values of k were considered. Fig. 3.4(b) and (c) show two derived parameters, $\psi = \beta/\alpha$ and $\upsilon = \psi^2 - 1$, which will be useful in some expressions to appear later on the document. Notice that the plots show only the results for $\beta > 1$, that is, they only present the cases in which the sensitized resonator resonates at a higher frequency than the scatterer ($\omega_s < \omega_r$)[4].

It can be noticed that α is always less than unity, which corresponds to a downshift of the resonance frequency of the sensor with respect to the original case in which no resonator was coupled. Moreover, it is observed than α is proportional to β. Both observations lead to a general understanding of the effect of the sensitized resonator. Assuming an initial state in which $\omega_r > \omega_s$, if the sensitized resonator is responsive to an external stimulus in such a way that it shifts its resonance frequency, the sensor's resonance frequency will suffer a proportional shift. As the sensitized resonator's resonance frequency gets closer to the scatterer's resonance frequency (so $\beta \approx 1$), the resultant downshift effect in the sensor is maximum. It can be also observed that this effect is larger for higher values of k.

The effect of the sensitized resonator quality factor in the resonance frequency can be observed in Figs. 3.5(a)-(c). Lower values of Q_r reduces the sensor's resonance frequency downshift. It was also observed that for $k^2 Q^2 < 2$, there was no more frequency downshift ($\alpha = 1$). This means that, if the sensitized resonator responding to a desired stimuli reduces its quality factor due to the dielectric losses of the material, there will be a point at which the sensor stops responding.

3.2.2 Quality factor of the sensor

The scatterer near its resonance was modeled as a lossy LC resonator. The losses are due to both the ohmic and dielectric losses of the materials and the radiating losses. In fact, since it is desirable that the scatterer re-radiates when impinged by an EM wave, the radiation

---

[4]The cases concerning $\omega_s > \omega_r$ are not evaluated here, since it was demonstrated that this condition is not ideal for the sensor design. This fact becomes more evident in next subsections.

Figure 3.4: (a) Normalized resonance frequency of the loaded scatterer ($\alpha = f_A/f_s$) and derived variables ((b) $\psi = \beta/\alpha$, (c) $v = \psi^2 - 1$) as a function of the normalized resonator resonance frequency ($\beta = f_r/f_s$) for different values of k, at $Q_r = 100$.

(a) (b) (c)
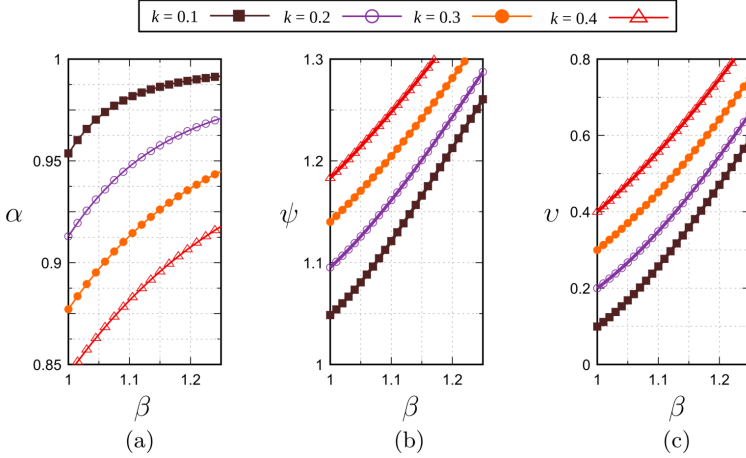
Source: The author.

losses are, in that sense, "necessary". Furthermore, the quality factor of the scatterer (Q_s) can be used to quantify these losses. However, after coupling the scatterer to the sensitized resonator, the resultant quality factor will be modified. The new quality factor of the sensor (Q_A) is expressed by

$$Q_A = \left. \frac{\omega L_A(\omega)}{R_A(\omega)} \right|_{\omega = \omega_A}, \tag{3.32}$$

where R_A and L_A were estimated in (3.14) and (3.17), respectively. Substituting those expressions in (3.32) and dividing it by the scatter quality factor, a normalization of the quality factor of the sensor can be obtained (Q_A/Q_s). A simplified expression in terms of v (see Fig. 3.4) is written below.

$$\frac{Q_A}{Q_s} = \frac{\alpha \left(1 + \left(1 + k^2 Q_r^2\right) v + Q_r^2 v^2\right)}{1 + k^2 \beta Q_s Q_r + v + Q_r^2 v^2}. \tag{3.33}$$

Numerical results from (3.33) are shown in Fig. 3.6. It can be observed that, as β increases, the normalized quality factor tends to unity. This is expected since at those frequencies, the resonator resonates

Figure 3.5: (a) Normalized resonance resultant frequency ($\alpha = f_A/f_s$) and derived variables ((b) $\psi = \beta/\alpha$, (c) $\upsilon = \psi^2 - 1$) vs normalized resonator resonance frequency ($\beta = f_r/f_s$) as a function of Q_r at $k = 0.2$.
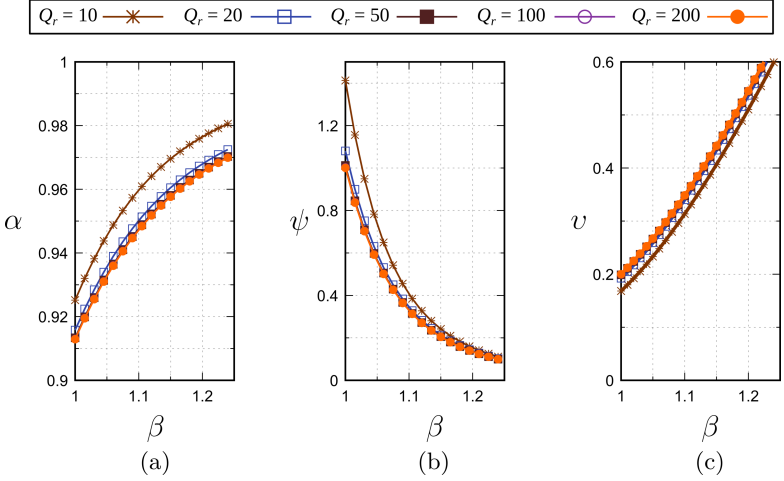
Source: The author.

far from the scatterer, thus, both the inductance and resistance values remain almost equal to the scatterer values, which was already seen from (3.14) and (3.17). As β approaches unity, the results are notoriously dependent on the Q_r/Q_s ratio. When $Q_r/Q_s < 1$, the resultant quality factor is reduced in comparison the scatterer quality factor. This is due to the more significant augment of the real part of the self-impedance of the sensor around resonance in comparison to the imaginary part. The reduction is controlled to some degree as Q_r exceeds Q_s. It can be noticed that when $Q_r/Q_s \gg 1$, the resultant quality factor may be even higher than the scatterer's, Which corresponds to a reactive term contribution to the total sensor impedance. Finally, for all cases, the results are intensified as the coupling factor k is increased.

From these results, it can be stated that, from the point of view of the quality factor of the sensor which is related to the bandwidth of the RCS peak, as discussed in Section 3.2.2, it is desirable that $Q_r \gg Q_s$. This may not be difficult to achieve if the sensor is implemented with non-lossy materials. The contrary is expected when using low-cost materials since they are particularly lossy in the radiofrequency band.

Figure 3.6: The ratio Q_A/Q_s for estimating the quality factor of the loaded scatterer.
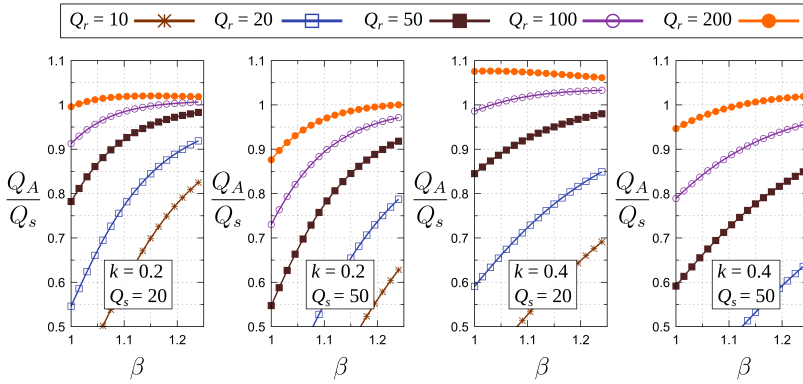
Source: The author.

3.3 SENSITIVITY ANALYSIS

3.3.1 General expression of the resonance frequency variation in all the sensor range

Let us consider that the sensor is responsive to a certain measurand through the change on the dielectric properties of the sensitizing material. Hence, the total variation of resonance frequency during the measurement can be expressed as

$$\Delta f_A = f_A|_{\zeta_b} - f_A|_{\zeta_a}, \tag{3.34}$$

or equivalently as

$$\Delta f_A = f_A|_{\varepsilon_b} - f_A|_{\varepsilon_a}, \tag{3.35}$$

where $f_A|_{\zeta_{a(b)}}$ and $f_A|_{\varepsilon_{a(b)}}$ refer to the initial(final) measurand state and electrical permittivity value, respectively, related to the environment in which the sensor is contained.

From the definition in (3.31), (3.35) can also be expressed as

$$\Delta f_A = (\alpha f_s)|_{\varepsilon_b} - (\alpha f_s)|_{\varepsilon_a}. \tag{3.36}$$

Assuming that the scatterer is not responsive to the measurand, so its resonance frequency is unvarying, this expression reduces to

$$\Delta f_A = f_s \left(\alpha|_{\varepsilon_b} - \alpha|_{\varepsilon_a} \right), \tag{3.37}$$

which can also be rewritten in terms of the relative variation of the sensor resonance frequency:

$$\frac{\Delta f_A}{f_A|_{\varepsilon_a}} = \frac{\alpha|_{\varepsilon_b}}{\alpha|_{\varepsilon_a}} - 1, \tag{3.38}$$

or equivalently, from (3.31), as

$$\frac{\Delta f_A}{f_A|_{\varepsilon_a}} = \frac{G\left(\beta|_{\varepsilon_b}, Q_r, k \right)}{G\left(\beta|_{\varepsilon_a}, Q_r, k \right)} - 1, \tag{3.39}$$

where Q_r and k were assumed to be invariant to ε for the sake of simplicity. Therefore, it can be stated that to estimate the total variation of the resonance frequency of the sensor, $\beta|_{\varepsilon_a(b)}$ must be estimated first.

3.3.1.1   Alternative expression based on relative sensitivity

If the total resonance frequency variation variation occurs within an small range, recalling (2.12), the relative variation of the resonance frequency with respect to ζ can be approximated to

$$\Delta f_A \approx \Delta\zeta \left. \frac{\delta f_A}{\delta\zeta} \right|_{\zeta_a}, \tag{3.40}$$

where $\Delta\zeta = \zeta_b - \zeta_a$. Furthermore, since the variation of the equivalent effective electrical permittivity that surrounds the sensor is related to the stimulus, similar to (2.15), it is true that

$$\Delta f_A \approx \Delta\varepsilon \left. \frac{\delta f_A}{\delta\varepsilon} \right|_{\varepsilon_a}, \tag{3.41}$$

where $\Delta\varepsilon = \varepsilon_b - \varepsilon_a$. Both (3.40) and (3.41) can be used interchangeably according to the previous knowledge on the dielectric material response. In particular, (3.41) can be directly used by obtaining the rate of change of the resonance frequency due to a variation on the permittivity through EM simulations.

In terms of the sensitivity, as defined in Section 2.3.1, (3.41) can be rewritten as:

$$\frac{\Delta f_A}{f_A} = \frac{\Delta \varepsilon}{\varepsilon} S_\varepsilon^{f_A}. \tag{3.42}$$

Different to (3.39), it is observed that (3.42) expresses the relation between the electrical permittivity change and the resonance frequency directly through the sensitivity term.

3.3.2 Sensitivity from equivalent electrical circuit model

Based on the electrical circuit model of the sensor, the sensitivity $S_\varepsilon^{f_A}$ in (3.42) can be expressed in terms of the sensitivity of the total inductance L_A to the permittivity variation. Therefore, it can be expanded as

$$\begin{aligned} S_\varepsilon^{f_A} &= S_{L_A}^{f_A} S_\varepsilon^{L_A}, \\ &= S_{L_A}^{f_A} S_{f_r}^{L_A} S_\varepsilon^{f_r}. \end{aligned} \tag{3.43}$$

Recalling that $f_A = \sqrt{2\pi L_A C_s}^{-1}$, the first term results in $S_{L_A}^{f_A} = -0.5$. Moreover, $S_\varepsilon^{f_r} = S_{C_r}^{f_r} S_\varepsilon^{C_r}$ can be obtained either by simulation, given the physical dimensions of the resonator, or from approximated mathematical formula that describe the sensitized resonator capacitance C_r as a function of ε. Finally, the sensitivity $S_{f_r}^{L_A}$ can be calculated from the expression in (3.17) and evaluating it at the resonance frequency. Following these steps leads to

$$S_{f_r}^{L_A}\Big|_{\omega=\omega_A} = \frac{-2k^2 Q_r^2(v+1)\left(Q_r^2 v^2 - 1\right)}{\left(1 + v + Q_r^2 v^2\right)\left(1 + v\left(1 + k^2 Q_r^2\right) + Q_r^2 v^2\right)}. \tag{3.44}$$

In addition to the previous results, it is useful to quantify how much of the "capacitive" responsiveness of the resonator (through C_r) is perceived as an inductive effect, that is, in L_A. This can be done by calculating $S_\varepsilon^{L_A}/S_\varepsilon^{C_r} = -0.5 S_{f_r}^{L_A}$. As an example, this normalized sensitivity, derived from (3.44), is plotted in Fig. 3.7(a) for different values of k and, in Fig. 3.7(b), of Q_r. As seen from the plot at the right (high Q_r), as β approaches unity, that is, the resonator's and scatterer's resonance frequencies are approximately equal, the normalized sensitivity approaches unity, which means that almost all the sensitivity due to the resonator capacitance is effectively perceived as an inductive effect in the sensor. On the contrary, if β is kept a bit far from unity, the total

sensitivity may reach only a percentage of the sensitivity of C_r (40% to 80% for $\beta \approx 1.05$). Larger sensitivity levels correspond to higher values of k.

From the plot in the left, it can be better observed that as the quality factor of the resonator decreases, the sensitivity reduces. According to the kQ_r values, at β near unity, the sensitivity starts decaying and it distances from the 100% value.

Figure 3.7: Normalized sensitivity as a function of β: (a) for different values of k and $Q_r = 100$, (b) for different values of Q_r and $k = 0.2$.
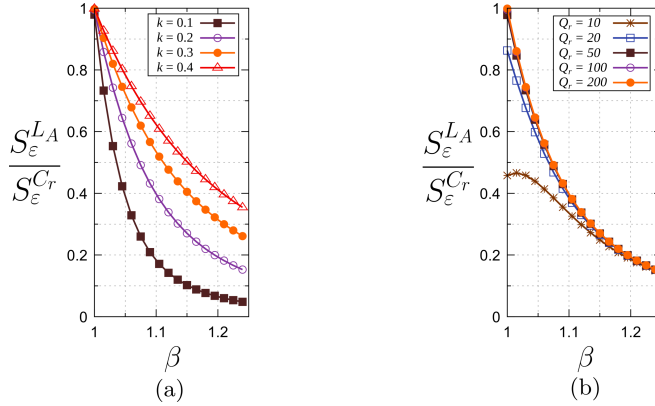
Source: The author.

3.4 RADIATION EFFICIENCY ANALYSIS

3.4.1 Radiation efficiency calculation

According to the definition given in Section 2.3.2, the radiation efficiency is determined by

$$\eta_A = R_A^{rad}/R_A, \tag{3.45}$$

where R_A^{rad} is the term regarding the radiation resistance of the total resistance of the sensor (R_A). Based on the electrical model of the sensor, the complete real part of the sensor's self-impedance would be given by (3.14). By isolating R_s, the real part can be re-expressed as

$$R_A = R_s \left(1 + k^2 Q_r^2 \left(\frac{\omega_r Q_s / \omega_s Q_r}{\omega_r^2 / \omega^2 + Q_r^2 \left(1 - \omega_r^2 / \omega^2 \right)^2} \right) \right), \qquad (3.46)$$

where R_s is the equivalent total resistance of the scatterer which includes both radiation terms, R_s^{rad} and R_s^{loss}, respectively ($R_s = R_s^{rad} + R_s^{loss}$). After substituting (3.46) in (3.45), and since $R_A^{rad} = R_s^{rad}$, the radiation efficiency of the sensor can be found.

$$\eta_A = \eta_s / \left(1 + k^2 Q_r^2 \left(\frac{\omega_r Q_s / \omega_s Q_r}{\omega_r^2 / \omega^2 + Q_r^2 \left(\omega_r^2 / \omega^2 - 1 \right)^2} \right) \right), \qquad (3.47)$$

where $\eta_s = R_s^{rad} / R_s$ is the radiation efficiency of the scatterer. The total radiation efficiency can also be expressed in the form $\eta_A = \eta_s / \gamma$. This factor γ represents the impact of coupling the resonator to the scatterer on its radiation efficiency. When the evaluating the efficiency at the resonance frequency, then:

$$\gamma = 1 + k^2 Q_r^2 \left(\frac{\beta}{1 + \upsilon + Q_r^2 \upsilon^2} \right) \frac{Q_s}{Q_r}. \qquad (3.48)$$

As it is observed, the efficiency i dependent on the product kQ_r, on the resonance frequencies of both resonator and scatterer, and on the ratio of its quality factors (Q_s / Q_r).

The factor γ is plotted in Fig. 3.8 for different values of k, Q_r and Q_s. Indeed, due to the increment of the equivalent real part of the scatterer, as noticed from the results in the plots results and the expression in (3.46), it should be expected that the radiation efficiency decreases. In general, as β approximates unity, γ rises and the efficiency is reduced. On the contrary, when β increases, the total resistance is reduced and the efficiency is less influenced. Particularly, when $Q_r = Q_s$, γ's maximum value (at $\beta = 1$) is 2, so the radiation efficiency is decreased in 50%. Finally, when the resonator's quality factor exceeds the one of the scatterer ($Q_r \gg Q_s$), then $\gamma \approx 1$ and the radiation efficiency remains almost the same as the one of the scatterer.

3.4.2 Effect on maximum RCS

As shown in (2.21), the peak value of the normalized RCS of the sensor –which occurs at resonance– can be expressed as

Figure 3.8: γ factor in (3.48), which corresponds to the impact of the resonator coupling to the radiation efficiency of the sensor.
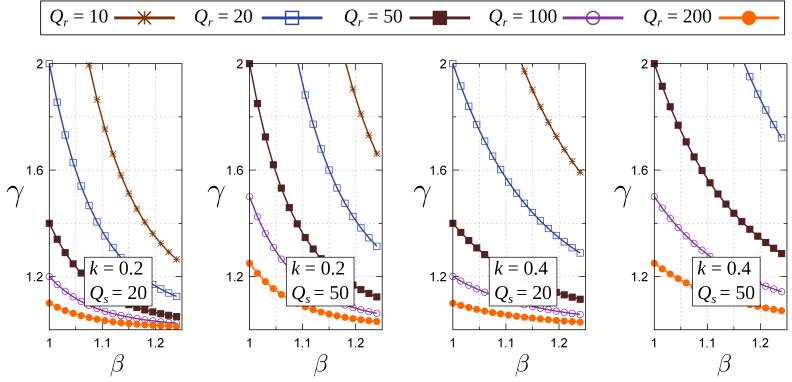
Source: The author.

$$RCS^n_{(max)} = \frac{\eta_A^2 D^2}{\pi}. \tag{3.49}$$

Therefore, $RCS^n_{(max)} \propto \eta_A^2$ or, equivalently, by considering (3.47), $RCS^n_{(max)} \propto \eta_s^2/\gamma^2$. In other words, the RCS decays proportionally with γ^{-2} due to the effect of coupling the scatterer to the sensitized resonator. By examining the radar equation, this relations are equivalent to a dependence of the reading range on the square root of the inverse of γ.

The results shown in Fig. 3.8 are replotted in terms of the total RCS decrement in Fig. 3.9. It is observed that, for expected values of Q_s, Q_r and k, there may be a potential decrement of 15 dB in the maximum RCS approximately. Nonetheless, by guarantying that $Q_s \geq Q_r$, this decrement should be limited to 6 dB, in accordance with the 50% factor described earlier. Also, the reduction on the RCS may be controlled by guarantying that the resonator resonates at an enough high frequency compared to the scatterer, that is, keeping β slightly higher than unity.

Figure 3.9: RCS decrement factor, obtained through the results in Fig. 3.8 for the factor γ.
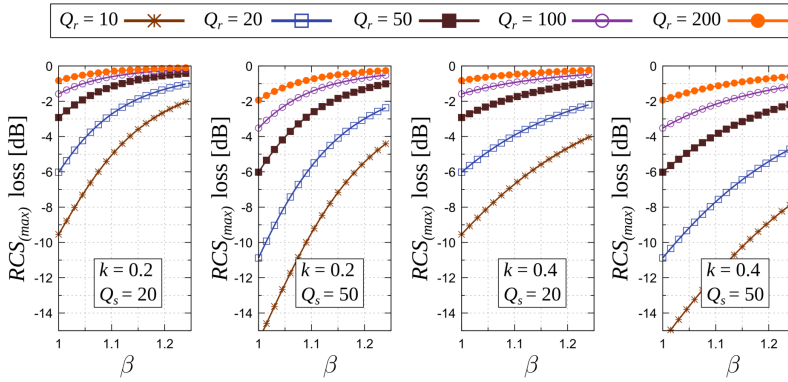
Source: The author.

3.5 CHAPTER CONCLUSIONS

First of all, with respect to the proposed structure of the sensor, it can be said that it permits to maximize the radiation efficiency focusing on the the scatterer design independently on the design of the transducer, at least to a first order. For example, if it is the case that the chosen radiating particle is an ORR for miniaturization purposes, its radiation efficiency can be controlled through the slit size. Other form factors may be used for the scatterer design if distance range should be prioritized rather than tag miniaturization.

A simple electrical model has been proposed to estimate the impact of the effect of the sensitized resonator in the main figure of merits of the chipless sensor, that is, maximum RCS, the quality factor and the total sensitivity, and compare to the case of the scatterer itself. Regarding the RCS, it was confirmed that there would exist a degradation on the RCS due to the losses added by the inclusion of the resonator (both a combination of ohmic and dielectric losses due to fabrication materials). In addition to this, an expression was obtained to estimate the total sensitivity of the sensor as a function of the sensitivity of the resonator. This expression revealed that a percentage and not the wholeness of the resonator's sensitivity would be effectively used in practical scenarios. Finally, an expression for the quality factor was

also deduced.

In particular, it was revealed that the relation between resonator and scatterer resonance frequencies impacts on all the figure of merits. Regarding the RCS, for example, it was estimated that its reduction is more pronounced as the resonance frequency of the resonator gets closer to the scatterer resonance. From the RCS point of view, it is then important to keep those resonances far from each other. Nonetheless, at the same tame, the results obtained for the sensitivity indicated the contrary. The sensor would take more advantage of the sensitivity of the resonator as both resonances, of the scatterer and the resonator, are closer. Therefore, a trade-off between both RCS and sensitivity exists, which implies choosing to design the sensitized resonator to resonate in a frequency band which is slightly higher than the resonance frequency of the scatterer. This band should take into account the resonators' resonance frequency rate of change due to the monitored measurand.

Other important factor to be considered while designing the sensor is the kQ_r product. From the standpoint of the sensitivity, this factor should be maximized. Since the quality factor of the resonator is restricted by both fabrication process and the materials used to implement the sensor, the structure must be designed to maximize k, specially in the case of very lossy materials. Here another evidence on the trade-off between sensitivity and efficiency arose, since the RCS loss is expected to be more critical at a higher kQ_r product.

Finally, there is another important parameter which is the ratio of the scatterer and resonator quality factors (Q_s/Q_r). For example, the last issue about the loss in the RCS can be compensated if the quality factor of the resonator is greater than the one of the scatterer ($Q_r \gg Q_s$). Moreover, this is also positive from the point of view of the quality factor of the sensor as a whole.

By following these guidelines, it is expected that a miniaturized sensor with high RCS and good quality factor is achieved. It is also expected that the sensitivity is a little reduced compared to the whole sensitivity of a capacitive transducer itself, however, it is important to recall that, in practical scenario, what matters is that the sensor is sensitive enough to perform according to the required application.

4 PROOF-OF-CONCEPT IMPLEMENTATION

This chapter intends to show the performance of a physical implementation of the sensor theorized in the previous chapter. For this purpose, the layout design chosen for the sensor is first presented. Then, a set of electromagnetic simulations results are shown, from which the functioning of the proposed sensor was unveiled regarding its RCS and its sensitivity. Finally, the experimental results of the implemented prototypes in FR-4 substrate are presented, discussed, and compared to other sensors reported in literature.

4.1 STRUCTURE LAYOUT AND SIMULATION

4.1.1 Layout

For the purpose of miniaturization, the physical size of the sens was reduced by merging both the radiator and the transducer into a single structure. Reported capacitive-based approaches used miniaturized loop-like structures as scatterers [95]. Among them, the Open-Ring Resonator or ORR is an area-efficient scatterer which has been reported in some uniplanar chipless sensors [39, 104]. It is basically a folded version of a resonant half-wave dipole. Therefore, the proposed sensor in this work also includes a ORR as the main scatterer.

In addition to the scatterer, a magnetically coupled resonator was included as the main sensing mechanism. The Split Ring Resonator (SRR) was used for this purpose since it is a very compact structure whose first resonance occurs at a very low value compared to the expected value from the wavelength related to the rings size. This is originated from the fact that the rings are strongly coupled, thus, there is a high distributed capacitance between the rings.

The layout of the proposed structure is depicted in Fig. 4.1. As noticed, the design is aimed at achieving a single-layer area-efficient layout, so as to be compatible with fabrication through low-cost additive printing processes. Squared versions of both the ORR and SRR where chosen, in part, since they facilitated the fabrication of the prototypes, but more importantly, since this was favorable for a better usage of the available area.

Figure 4.1: Layout of the proposed sensor.
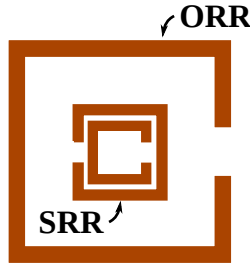
Source: The author.

4.1.2   Currents and EM fields distribution

Before the implementation of the first prototypes of the sensor, a set of simulations were performed to gain a better insight of the functioning of the sensors. For all the simulations, we used commercial software tools from Keysight Technologies, specifically Advanced Design System (ADS®) and Electromagnetic Professional (EMpro®).

The first sets of simulations were executed to corroborate the current and fields distribution in the structure nearby its resonance. For the current analysis, the layout of the sensor was built in ADS and the Method of Moments (MoM) was used as the solving method. A differential input port was included at the middle of the conductive trace of the ORR, which emulated the response of the sensor after interrogation with a vertically polarized EM wave. To distinguish the resonance frequency of interest, the input impedance at this port was observed after processing the scattering parameters, and the region in which the imaginary part of this impedance was null was tracked.

The currents distribution was investigated for three different orientations (rotation angle) of the SRR with respect to the ORR, aiming at understanding the coupling effect of both elements in each case. The results of the sensor current distribution for rotations of $0°$, $90°$ and $180°$ are shown in Figs. 4.2, 4.3, and 4.4, respectively. In each of the plots, the current distribution are shown for three frequency values, more specifically, under, close to and over the resonance frequency of the sensor (f_A). In all cases, the SRR was designed to resonate at a higher frequency than the ORR.

It can be observed that for all angles of rotation, the subplots (a) and (b) present a very similar current distribution, that is, the currents

in all traces curl with the same orientation. This was expected from the circuit analysis where (3.1) was derived from, which had shown that, when the operating frequency was lower that the resonance frequency of the resonator, the current flow in the resonator was contrary to the flow that would have been expected in the case of two coupled inductors with resistive loads. Thus, it can be stated that a constructive flux due to the resonator occurs at those frequencies since it is mostly capacitive. In addition, it can be also observed that the main difference between subplots (a) and (b) resides in the higher intensity of the currents at the resonance case.

Additionally, it is seen that in all (c) subplots, which correspond to a frequency slightly above the SRR self-resonance, the current orientation in the SRR rings are equally oriented, but contrary to the ORR's. This behavior was expected since the SRR is more inductive at those frequencies. In fact, it should be observed that the current orientation in the SRR rings are always equal to each other, independently of the ORR current orientation, which is compatible to the expected results of the SRR below its second resonance frequency [87].

Finally, it is also observed that the highest current magnitudes in all rings occur at the middle of each traces, that is, opposite to their slits. Since the SRR is almost symmetrical in all their axes, it is expected that the total magnetic flux originated by the induced currents is homogeneous long the SRR surface. Conversely, this should not be expected in the ORR case, where the magnetic flux is more concentrated at its center (around the feed port in this simulation). The distribution of the magnetic flux serves as an important indicator for the magnetic coupling and the obtained resonance frequencies values in each of the angle rotations. The simulation results showed that, at a higher rotation angle, the resonance frequency increases. This result is better understood from the visual inspection of the the current distributions at resonance, which is shown in Fig. 4.5. It is seen from these results that the SRR presents the highest current intensities in the 0° case. Therefore, it can be stated that, in that case, the coupling between the ORR and the SRR is achieves the highest value, producing a larger downshift in the sensor frequency.

The electric and magnetic fields distribution were computed by the Finite Element Method (FEM) in ADS. As in the MoM case, a feed port was located at the middle of the conductive trace of the ORR. Moreover, the specification of the dimensions for the bounding box was required for the mesh volume. In general, a a bounding box of at least a quarter of the wavelength corresponding to the lowest simulation

94

Figure 4.2: Current distribution in the sensor conductive traces obtained with MoM solver with 0° rotation of the SRR (Dynamic range scale in this plot is 117.25 dB). Considered parameters for simulation: $l_{ORR} = 9\,\mathrm{mm}$, $l_{SRR} = 6\,\mathrm{mm}$, FR-4 lossless substrate and sheet copper traces. Mesh: 100 cells/max. wavelength. Max. freq. simulation: 4 GHz.

(a) @ $0.873 f_A$ (b) @ $0.999 f_A$ (c) @ $1.262 f_A$
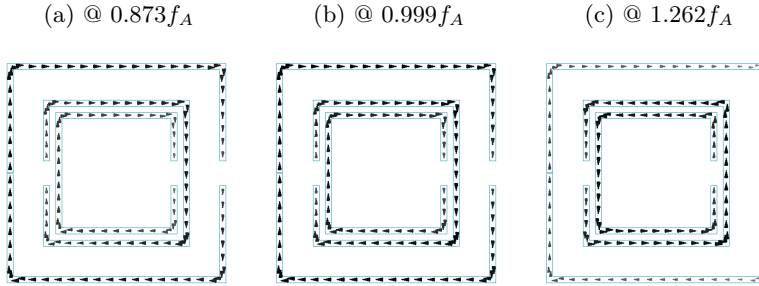
Source: The author.

Figure 4.3: Current distribution in the sensor conductive traces obtained with MoM solver with 90° rotation of the SRR (Dynamic range scale in this plot is 121.39 dB). Considered parameters for simulation: $l_{ORR} = 9\,\mathrm{mm}$, $l_{SRR} = 6\,\mathrm{mm}$, FR-4 lossless substrate and sheet copper traces. Mesh: 100 cells/max. wavelength. Max. freq. simulation: 4 GHz.

(a) @ $0.828 f_A$ (b) @ $0.999 f_A$ (c) @ $1.261 f_A$
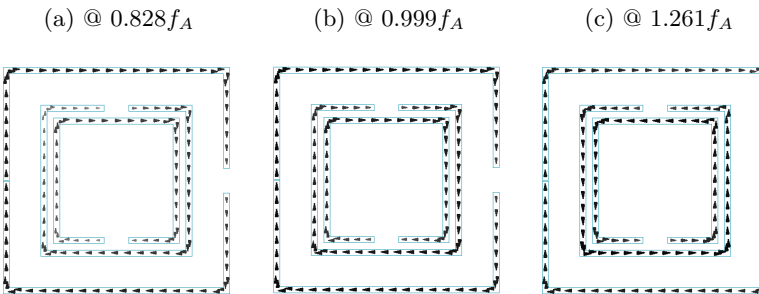
Source: The author.

Figure 4.4: Current distribution in the sensor conductive traces obtained with MoM solver with 180° rotation of the SRR (Dynamic range scale in this plot is 126 dB). Considered parameters for simulation: $l_{ORR} = 9\,\text{mm}$, $l_{SRR} = 6\,\text{mm}$, FR-4 lossless substrate and sheet copper traces. Mesh: 100 cells/max. wavelength. Max. freq. simulation: 4 GHz.

(a) @ $0.956 f_A$ (b) @ $0.999 f_A$ (c) @ $1.178 f_A$
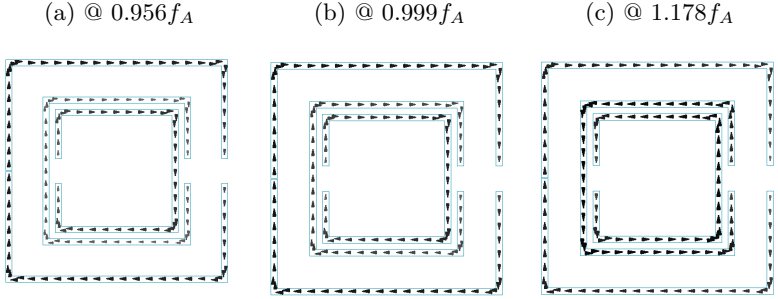
Source: The author.

Figure 4.5: Current distribution in the sensor conductive traces obtained with MoM solver comparing three angle rotations of the SRR at resonance.

(a) $0°(f_{A(0°)})$ (b) $90°(1.02 f_{A(0°)})$ (c) $180°(1.08 f_{A(0°)})$
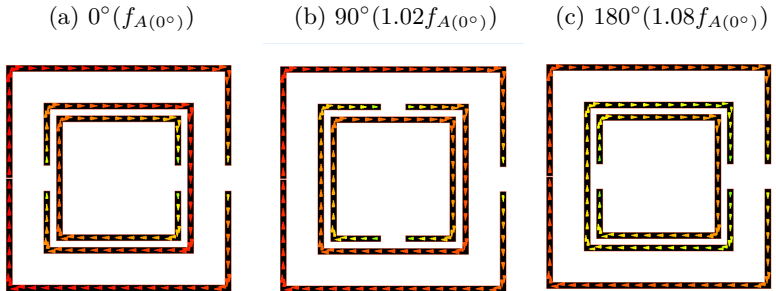
Source: The author.

frequency was required to obtain an accurate value of the resonance frequency.[1]

The results of the electric field distribution in the case of 0° SRR rotation angle are shown in Fig. 4.6. Here, again, the results are presented for three different frequencies related to the sensor's resonance. A pair of subplots are shown for each frequency corresponding to the field intensity distribution, at the left column, and the field vectors, at the right. Higher intensities are registered in the first two pairs of subplots which correspond to frequencies below and close to the resonance frequency, respectively (4.6(a)-(d)), compared to the above-the-resonance subplots (4.6(e) and (f)). Moreover, it should be noted that in those cases of higher field intensities the field lines start(end) at the ORR trace and end(start) in the outer ring of the SRR. Differently, in the above-the-resonance subplots, they start(end) at the ORR, but end(start) at the inner ring of the SRR. This behavior corresponds to the change in the currents orientation, which generates a different charge distribution along the traces.

Besides, it should be noted that the intensity in the gap between the rings of the SRR is more intense in the last pair of subplots compared to the rest. This was expected due to the proximity to the SRR's resonance frequency, where the field intensity between rings is intensified.

Furthermore, the correspondent magnetic field intensity distribution and vector orientations are shown in Fig. 4.7. A different cut-plane was chosen for the field vectors (right column) to highlight the interaction between ORR and SRR at the feed port location.

It is noticed that the field distributions are the same in the first two pair of subplots (4.7(a) to (d)), however, higher field intensities are observed in the near-resonance case. The field intensity caused by the ORR is higher at its mid-point, which was expected from the current analysis. As a result, it can be stated that a higher magnetic coupling factor can be obtained, not only at the 0° rotation scenario, but by getting the SRR as close as possible to the ORR mid-point.

Finally, it is seen that in the third frequency case (above resonance), the field distribution is modified and the intensity is reduced. This behavior is explained given the change of the orientation of the currents in the SRR with respect to the ORR.

---

[1]This was the reason that most of the rest of simulations were done with MoM solver since they converged much faster. Nonetheless, for this specific case, FEM was necessary to compute the EM fields at the near-field region.

Figure 4.6: Electric field distribution in the sensor obtained with FEM solver. Considered parameters for simulation: $l_{ORR} = 9.5$mm, $l_{SRR} = 6.5$mm. Lossless substrate of 50 mm height with $\varepsilon_r = 2$ and sheet copper traces. Max. freq. simulation: 4.5 GHz.

(a) XY-plane @ $0.884f_A$

(b) YZ-plane @ $0.884f_A$

(c) XY-plane @ $0.957f_A$

(d) YZ-plane @ $0.957f_A$

(e) XY-plane @ $1.331f_A$

(f) YZ-plane @ $1.331f_A$
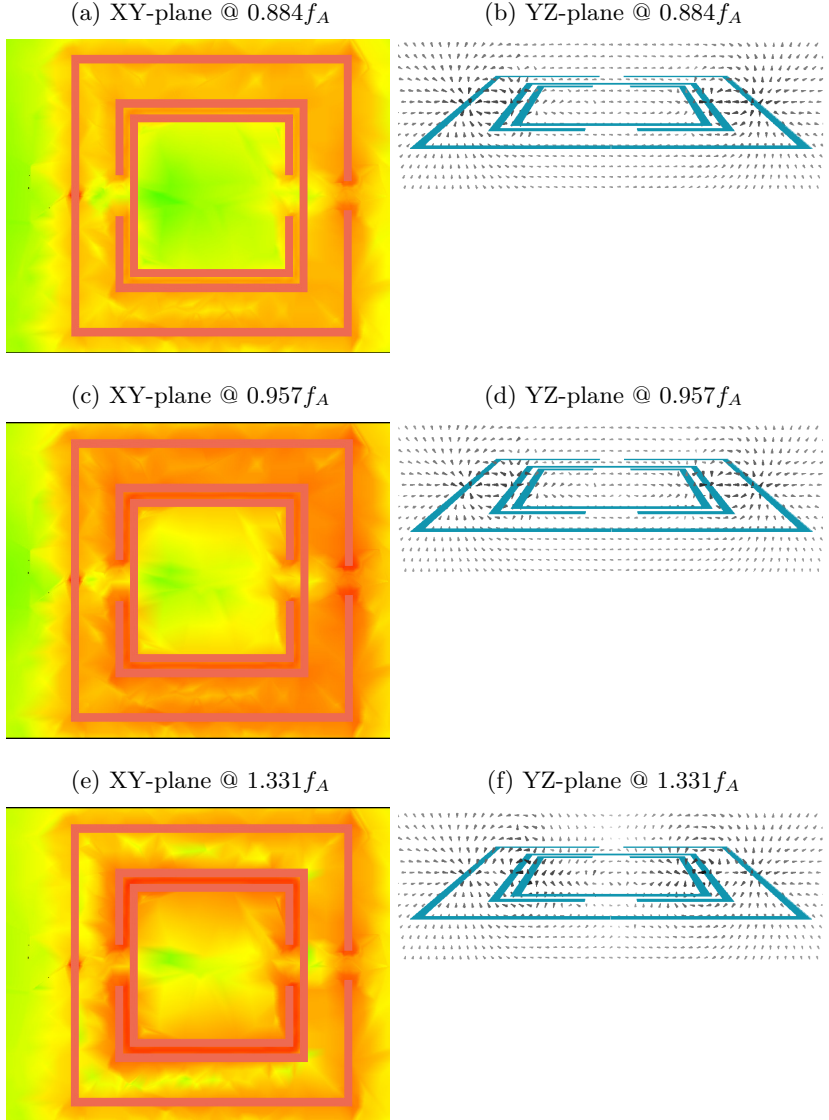
Source: The author.

Figure 4.7: Magnetic field distribution in the sensor obtained with FEM solver. Considered parameters for simulation: $l_{ORR} = 9.5$mm, $l_{SRR} = 6.5$mm. Lossless substrate of 50 mm height with $\varepsilon_r = 2$ and sheet copper traces. Max. freq. simulation: 4.5 GHz.
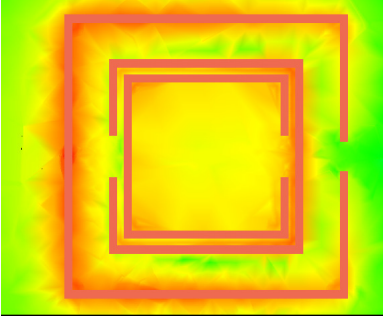
(a) XY-plane @ $0.884 f_A$

(b) XZ-plane @ $0.884 f_A$

(c) XY-plane @ $0.957 f_A$
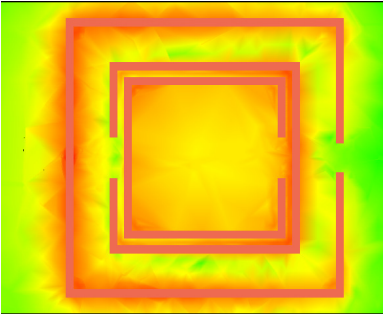
(d) XZ-plane @ $0.957 f_A$

(e) XY-plane @ $1.331 f_A$
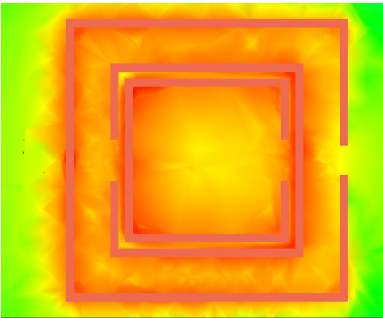
(f) XZ-plane @ $1.331 f_A$
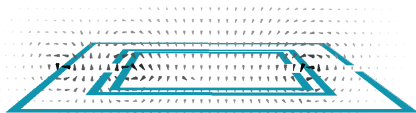
Source: The author.

4.1.3   Electrical model vs EM simulation

To validate the proposed circuit model described in Section 3.2, the results from a lumped-circuit simulation was compared to the EM simulation from the a 2.5-D model of the sensor simulated with the MoM solver. The values for the resistance, inductance, and capacitance of the model were obtained based on the quality factor extraction method of an LC resonator described in [128], which was adapted to the case of the proposed sensor as described in Section A.2 of the Appendix. The results of the input impedance from both the circuit and the EM simulation are compared in Fig. 4.8.

It is seen that both results match precisely up to the anti-resonance point, at which the real part reaches its peak value. This peak occurs very close to the sensitized resonator self-resonance. More importantly, the first resonance, which occurs below this anti-resonance point, is very well predicted by the proposed electrical model. This result supports the computed numerical results of the sensor figure of merits derived from the analysis of the model described in the Sections 2.3.1 and 3.4.

In addition, it can be observed that the second resonance, after the anti-resonance point, is not accurately described by the proposed model. This may be explained since at those frequencies the model used for the ORR around its self-resonance is not longer valid and a higher order model or distributed-parameter based model should be used instead. This second resonance was not critical for the purpose of the sensor's design regardless.[2].

Finally, it is worth commenting on the value of the magnetic coupling factor extracted as a function of the SRR's angle of rotation. After the parameter extraction procedure, it was corroborated that the model represented well the effect on the resultant resonance frequency of the sensor by adjusting the k value. More precisely, the k resulted in a higher value for the $0°$ case. For instance, considering the same simulation set for the results in Fig. 4.8, $k = 0.38$ in the $0°$ case, while $k = 0.18$ in the $180°$ case.

---

[2]This may be subject for future work though

Figure 4.8: Real and Imaginary parts of the sensor self-impedance obtained from lumped-circuit model and EM simulations.
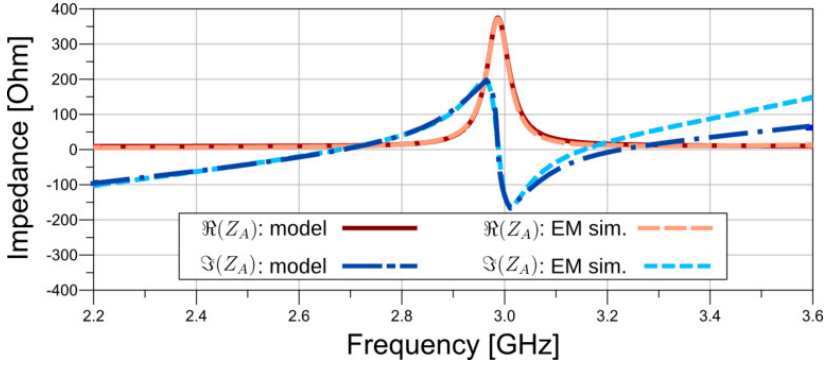
Source: The author.

4.1.4 Sensitivity to electrical permittivity

The implementation of the proposed sensor implies planar metallic structures which, depending on the fabrication process, can be etched from a metallic covered substrate, similarly to the common PCB fabrication, or by depositing the metallic traces as in additive process such as printing. In either case, the structure is made responsive to the desired parameter (stimulus) by sensitizing the electrical permittivity of the materials surrounding the metallic structure. This can be done in different manners. The most common include adding an extra sensitive layer on top of the planar structure, for example by coating a sensitive material, or using substrates whose dielectric properties are already sensitive to the desired stimulus. Therefore, it was important to predict the behavior of the resonance frequency, that is, the responsivity of the sensor, in both of these scenarios. In particular, since the resonance frequency of the sensor depended on the individual sensitivities of the ORR and the SRR, their response to the change of the electrical permittivity of the sensitive material was investigated.

Parametric EM simulations using the MoM solver by changing the electrical permittivity of the sensitized layer were performed. The results were obtained by varying either the relative electrical permittivity of the coating layer (ε_c) or of the substrate layer (ε_s), and plotting the results according to the normalized values, that is, with respect to the

default values ε_{c0} and ε_{s0}, respectively. Both the total cumulative shift of the sensor resonance (Δf) and the sensitivity were obtained, the latter defined as $S_{\varepsilon_i}^f = \frac{\Delta f}{\Delta \varepsilon_i} \frac{\varepsilon_{i0}}{f_0}$ (where $i = c, s$).[3]

In Fig. 4.9, the variation of the resonance frequency of both SRR and ORR for the case of a sensitive coating layer is shown for two different coating heights.[4] The SRR and ORR dimensions were selected for similar resonance frequencies at the default (initial) value electrical permittivity. Also, the ORR was shaped so the slit dimension was equal to the slits of the SRR (1 mm). For this simulation, a fixed non-sensitive $1.6\,\mu$m substrate layer ($\varepsilon_s = 4.4$) was considered and a default value of the relative electrical permittivity of the coating layer $\varepsilon_{c0} = 1$.

It is seen that, for both the coating layer heights, the change in the SRR resonance frequency is larger than in the ORR. This result is explained from the distributed capacitance within the rings of the SRR (for strong coupled rings). As the thickness of the coating layer increases, the frequency shift also increases since the shift is indeed dependent on the average resultant electrical permittivity, which includes the substrate, the coating and the air layers. A dependence on the coating layer thickness is expected up to the point in which that dimension is comparable to the metallic traces width and, in the case of the SRR, to the gap between rings. The results indicate that, even with a very small slit, the ORR achieves a lower sensitivity than the SRR. In fact, worse sensitivities are expected at bigger slits. Moreover, it is important to highlight that the sensor design needs to guarantee that most of the sensitivity of SRR is effectively used so the sensor does not underperform the ORR.

The corresponding sensitivity curves for the ORR and SRR in each subplots also show the higher responsivity of the latter. According to the used expression for the sensitivity, it is seen that it is higher for smaller values of change in the permittivity.

In Fig. 4.10, the results due to a sensitized substrate (no coating layer) are shown, for two different substrate heights and $\varepsilon_{s0} = 4.4$. Similar conclusions can be drawn for this case compared to the coating layer previous case. Since the substrate layer was considered thicker than the coating layer, the shifts on the resonance frequencies are also larger.

---

[3]Refer to the term $S_{\varepsilon_r}^{fr}$ in (3.43).

[4]Lower heights than those used in the plots resulted in convergence issues during the simulations.

Figure 4.9: ORR and SRR sensitivity to electric permittivity: coating case, for two coating thickness values (t_c)

(a) $t_c = 100\,\mu\mathrm{m}$ (b) $t_c = 10\,\mu\mathrm{m}$
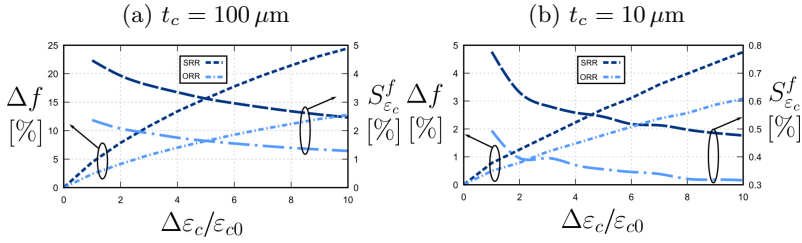
Source: The author.

Figure 4.10: ORR and SRR sensitivity to electric permittivity: substrate case, for two substrate thickness values (t_s).

(a) $t_s = 1.6\,\mathrm{mm}$ (b) $t_s = 160\,\mu\mathrm{m}$
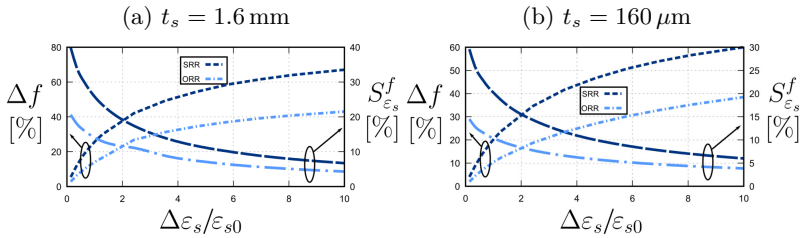
Source: The author.

4.1.5 Frequency dependence on dimensions

The resonance frequency of the ORR and SRR were also explored as a function of the ring length. Since both are shaped in square format, the lateral length was varied. The simulation results for the case of a fixed slit size are shown in Fig. 4.12(a). Lengths from 5 to 30 mm were used to cover the ISM frequency bands around 900 MHz and 2.45 GHz. These first results were useful to determine the size ranges of both resonators, so that the SRR resonate at a higher frequency than the ORR and it would be able fit within the ORR as well.

Based on the previous results, the sensor was simulated for some ORR and SRR lateral lengths. An example of these results for the 2.45 GHz ISM band are shown in Fig. 4.12(b). Those plots are valuable as an starting point to determine the dimensions for both the SRR and ORR according to the specifications of the sensor, which include maximum total area, sensitivity and radiation efficiency.

Figure 4.11: Resonance frequency for different lateral lengths (in [mm]).
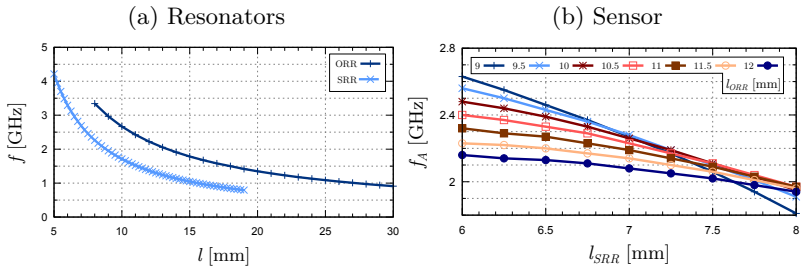
Figure 4.12: Resonance frequency for different lateral lengths (in [mm]).

Source: The author.

4.1.6 RCS and radiation efficiency

Electromagnetic simulations were used to compare the radiation performance of the proposed sensor to unloaded ORRs and to ORRs loaded with different capacitive transducers, such as the vertical-plate capacitor [39] and the horizontal-plate capacitor with plates centered at the slit [32] and in hairspin shape. Those structures are illustrated in

Fig. 4.13. The RCS was extracted from plane-wave excitation in EMPro with Finite-Difference Time-Domain (FDTD) simulations. For a fair comparison, the slits for all structures were fixed at the same value, since they are related to the achievable sensitivity.[5]

Figure 4.13: Three structures with same slit dimensions (g_s) for the RCS comparison with the proposed sensor through FDTD simulation. From left to right: horizontal-plate capacitor in hairspin shape, centered horizontal-plate capacitor, and vertical-plate capacitor
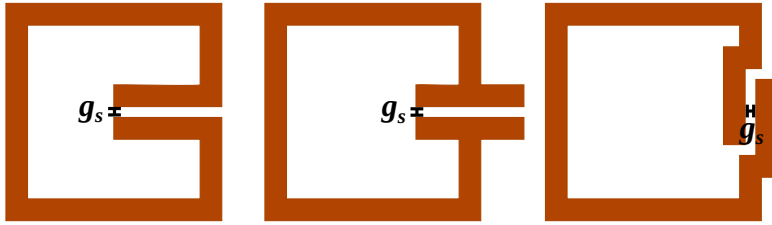
Source: The author.

The results from the FDTD simulation were complemented with the radiation efficiency calculated from the input impedance obtained in ADS using the MoM solver. All the results are summarized in Table 4.1.

The first lines in the table correspond to the case of the ORR (no transducer). It is seen that this structure would achieve the highest radiation efficiency. Also, its results depend on the slit size (s_o), as expected (see Section 2.4). However, since there is no explicit capacitive transducer, this structure would achieve the lowest sensitivity.

Even though the proposed structure presented a lower RCS than the ORR (as predicted in Section 3.4.1), compared to the rest of the structures based on capacitive transducers, it showed the best radiation performance. This is due to a higher achievable total ring length with respect to the resonance wavelength (l_o/λ). The results were obtained for two specified values of l_o/λ. In accordance to the ORR case, its RCS was higher for a larger slit. This result also demonstrates the capability to adjust the ring size according to the application size requirements.

---

[5]In practice, the slit dimension are limited by the fabrication procedures.

Table 4.1: Simulated radiation performance of ORRs with different transducers with same gap dimensions: Radiation resistance (R_r), radiation efficiency (η_r) and radar cross section. FR-4 substrate was used for simulating all the structures, and all were tuned to resonate at approx. 2.47 GHz with the MoM solver.

Transducer	l_o/λ	s_o/l_o	$R_r\,[\Omega]$ (MoM)	$\eta_r\,[\%]$ (MoM)	RCS [dBsm] (FDTD)
None (ORR)	0.09	0.02	4	49.5	-31
	0.12	0.97	12.8	76.4	-23
Horiz. parallel plate	0.06	0.04	0.6	16.4	-47
Horiz. parallel plate (hairspin)	0.06	0.04	0.7	16	-48
Vert. parallel plate	0.06	0.04	0.6	14.6	-50
Magnetically-coupled SRR (proposed)	0.08	0.11	2.3	28.3	-42
	0.11	0.96	8.4	56.6	-34

4.2 IMPLEMENTATION

The proposed sensor was first validated through the implementation of prototypes with typical materials and fabrication processes used for electronics boards. Thus, FR-4 epoxy substrates with single-layer copper were selected. A milling machine was used for producing the conductive traces of the sensor.

First of all, the substrate dielectric properties around the desired frequency band were characterized by using the two transmission line method [96]. Based on this information, similar EM simulations to the ones presented in Section 4.1.5 were performed to estimate the resonance frequencies of the ORR and the SRR. Based on the guidelines from the sensor modeling, a set of dimensions for both ORR and SRR were selected. Since a good conductive material (etched-copper) was used for the traces, and the substrate presented a relatively moderate loss factor ($\tan \delta \approx 0.017$ @ 2.45 GHz), miniaturization was the first goal for those

prototypes. Therefore, a minimum slit of the ORR was considered.Based on the chosen dimensions set and also previewing possible inaccuracies during the fabrication process of the structures, the final dimensions were chosen (shown in Table 4.2). A photo of the prototypes is shown in Fig. 4.14. As observed, besides the sensor structures, their corresponding ORRs (without coupled SRR) were also built for comparison purposes.

Table 4.2: FR4 tags dimensions (in mm.): l_o is the ORR lateral length, l_s is the SRR lateral length. All traces width and gap between rings were set to $w = 1$ and $g=0.25$, respectively.

tag	l_o	l_s
A	9	6
B	9	6.5
C	9.5	6
D	9.5	6.5

Figure 4.14: Photo of the prototypes in FR-4 substrate.

(a) some prototypes (b) ORR and sensor
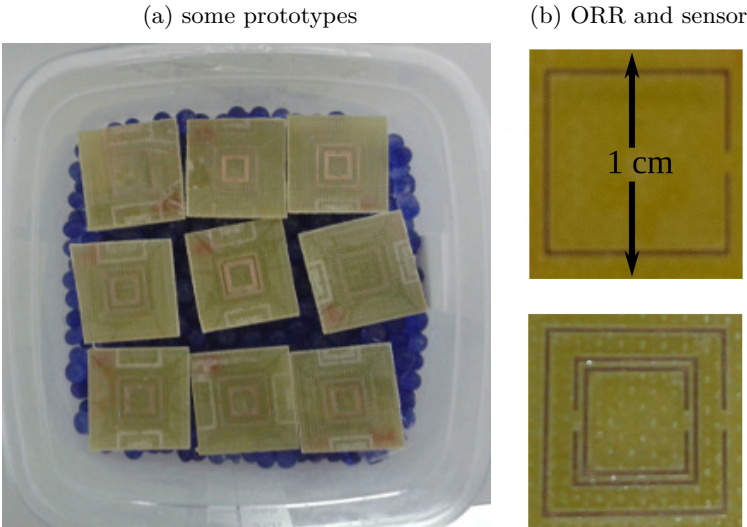
Source: The author.

The SRR was sensitized to the humidity of the environment; in other words, the sensor was configured as a RH sensor. For instance, there are different materials which can be used for this application. Materials

such as PEDOT [97], Kapton [98], PVA [32] and silicon nanowires [72] have been used in reported wireless RH sensors. Particularly, PVA is a hygroscopic polymer which has demonstrated to present good responsivity and it is practical for rapid prototyping. Therefore, this was the material selected for implementing the sensors.

PVA was diluted in 1:3 water ethanol solvent with a 1:10 proportion (1 g of PVA to 10 ml solution). This solution was left to magnetic stirring during 3 hours at about 70°C. Then, the solution was poured over the sensor (over the conductors face of the FR-4 substrate) and spin-coated. After that, it was cured with the use of a hot plate for 10 minutes approximately.

Initially, it was intended to only sensitize the SRR by applying a a PVA coating in the gap between rings region. However, from the observation on the sensitivities curves in 4.9, it was decided to take advantage of both ORR and SRR sensitivities. In this way, the total sensitivity would be the sum of both scattered and resonator. This is equivalent to adjust (3.43) as:

$$S_\varepsilon^{f_A} = \underbrace{S_{C_s}^{f_A} S_\varepsilon^{C_s}}_{\text{scatterer}} + \underbrace{S_{L_A}^{f_A} S_\varepsilon^{L_A}}_{\text{resonator}}. \tag{4.1}$$

where both terms add constructively. In this way the total sensitivity can be enhanced.

In addition to this, sensitizing both the resonator and the scatterer narrows the range of values of the ratio between their resonance frequencies, that is, the β parameter presented in the previous chapter. This is explained given that the sensor will respond to the environment RH, causing a shift on both resonance frequencies instead of only the resonator's. The importance of β as a design criteria was evidenced earlier.

4.3   EXPERIMENTAL RESULTS

4.3.1   Measurement setup

All prototypes were measured with the use of the three-step procedure described in [99] which has been frequently employed to characterize chipless sensors in literature. Several issues arose from the fact that the measurements were not executed inside an anechoic chamber, thus, some cautions due to the dynamism of the environment

were taken into consideration, as detailed in Section B of the Appendix. Some other issues regarding the antenna radiating pattern, the metallic scattering reference, the power of the excitation, among others, are also discussed there.

In particular, for the sensitivity analysis, the sensor was enclosed into a plastic chamber in which the RH level was controlled. The measurement setup is illustrated in Fig. 4.15. The chamber size and the type of antenna used varied according the specific measurement. Particularly, for the comparison between the responsivity of the sensor and the ORR, a transition from silica-gel to water inside the closed plastic container was employed. A commercial hygrometer was also included as a reference for verifying the RH change.

Another set of measurements were performed for determining the sensitivity of the sensor in which specific RH references were generated inside the chamber based on saturated salt solutions [100].[6] For each reference, the salt solution was left at least 24 hours within the container for stabilization of the environment.

Figure 4.15: Sensor RCS measurement setup.
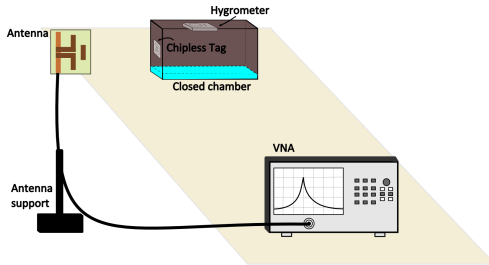
Source: The author.

4.3.2   Results

The RCS of the sensor and its corresponding ORR (without coupled SRR) were measured before the PVA coating was applied. The results are compared in Fig. 4.16(a) and (b) (only one sample per dimension set is shown). It is observed that the SRR inclusion affects both the resonance frequency, the peak RCS and the quality factor. It is also noticed that, in both figures, the sensor that includes the bigger

---

[6]All salt solutions water activity were previously verified.

SRR presented the lowest resonance frequency, which was due to the lower self-resonance of the SRR. Finally, the difference between the resonance frequencies in the figures resided in the fact that the second set consisted of a bigger ORR, which means that all resonances occurred at lower frequencies.

Figure 4.16: Measured RCS of the sensor and corresponding ORR for different set of dimensions (only one sample of each is shown).

(a) $l_{ORR} = 9\,\mathrm{mm}$ (b) $l_{ORR} = 9.5\,\mathrm{mm}$
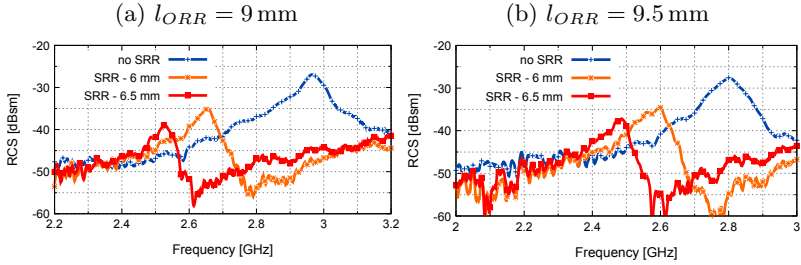
Source: The author.

The RCS of the samples with the same set of dimensions were also compared. Variations among them were expected from measurement repeatability, but, mainly, from the fabrication process. The analysis for one of the sets is shown in Fig. 4.17(a). Variations in both the ORR and the sensor samples were noticed, where the frequency shift was more notorious in the case of the sensor. This fact is related to the SRR variation from one sample to another. Indeed, fabrication inaccuracies were expected from the PCB milling machine, since the height of the substrate was not constant at the drilling plane, making the effective penetration of the drill bit vary from sample to sample. These differences led to different gap dimensions between rings which changed the total capacitance of each sample.

The effect of the fabrication process was confirmed after a closer inspection by using optical microscopy, as shown in Fig. 4.17(b). Through these images, it was verified that the sample #3 had the smallest gap dimension and trace-width-to-gap ratio with respect to the others, thus, leading to a lower self-resonance frequency and to the lowest sensor resonance frequency. In practice the variations due to fabrication errors can be anticipated if the process is known. For example, EM simulation results confirmed that a variation of 0.1 mm in a 0.25 mm gap can cause up to 5% of resonance variation of the SRR, which causes about 1% variation of the sensor resonance frequency.

The sensitivity characterization results obtained with the salt solution references are shown in Fig. 4.19. Both the absolute and relative variations of the resonance frequency are shown. A total variation of 104.4 MHz was measured, which covered the 2.45 GHz ISM band. The measurements was done in a RH range of 8.2 to 90.5%.

The comparison between the response of the RCS of the sensor and the ORR over time, both coated with PVA, obtained from the silica-to-water transition is shown in Fig. 4.18(a) and (b). It was observed that the total frequency shift (relative to its initial value) of the sensor is higher than in the ORR case. Therefore, it was confirmed that the sensitivity of the sensor was superior, even for higher period of exposure of the ORR to the humid environment. Explicitly, these results are summarized in 4.18(c). It can be seen that the frequency shift of the sensor resulted in approximately twice that of the ORR.

Another interesting fact from these measurements is observed from the RCS peak and quality factor changes over time. The RCS peak, in both cases, was diminished with time, approximately in 7 to 8 dB. Moreover, the quality factor was also reduced in both cases, resulting in a total approximate change from 40 to 22, in the sensor case, and from 30 to 9, in the ORR case. Both RCS and Q reduction are related to the loss factor increment of the PVA coating at higher RH [101]. In the case of the sensor, this effect is combined with the proximity of the resonance frequency of the SRR to the ORR as the RH increases, since the SRR is more sensitive.

4.3.3   Discussion of the results

From the previous results, it can be said that adding the sensitized resonator to the scatterer, which in this case corresponded to coupling the SRR to the ORR, caused better results from the sensitivity point of view. Moreover, for the chosen set of dimensions, the quality factor improved, which means that the 3-dB band around the RCS peak was narrowed which facilitates the interrogating procedure. Nonetheless, it was also verified that there was a reduction in the RCS peak.

Regarding the sensitivity of the implemented sensor, the measurement results were compared to other reported uniplanar frequency-shift coded capacitive chipless sensors. For instance, the sensors reported by Amin et al. [32] and Lu et al. [39] are also PVA sensitized. The measurements regarding the resonance frequency variation are shown in Fig. 4.20. It is worth mentioning that even though the sensitizing

material is the same in those examples, making an exact comparison between the results are not possible since they depend on the exact dose of the PVA coating.

The implementation reported by Amin et al. [32] used a much thicker PVA layer, which is related to its much higher relative frequency variation. The proposed sensor based on a magnetic coupled resonator exhibited comparable results to the work of Lu et al. [39] in a similar RH range. Derived results from these measurements are shown in Fig. 4.21, where the resonance frequency shift, absolute and relative sensitivity within each range of RH is shown.

The previous results are listed in Table 4.3. A summary of the results in a wider %RH range was include as a way of observing their mean values. In fact, two ranges of %RH were considered since the PVA electrical permittivity exhibits a nonlinear behavior with the %RH. Besides the previous cited works, another implementation of a chipless sensor presented by Vena et al. was also included for comparison [74]. This sensor was sensitized with a silicon nanowires (SiNWs)-based coating. The authors only reported their measurements for a narrow %RH range, in which its sensitivity was below the rest considering similar %RH ranges.

By comparing the relative size (l_o/λ) of the sensors, it is evident that the proposed sensor allows for a miniaturized design, also allowing for size optimization through the control of the ORR slit size. The sensor in [32] presents a doubled (mirrored) structure of a hairspin C-shape resonator to raise the RCS and sensitivity, therefore, it presented a higher relative size. On the other hand, the sensor in [39] is the smallest. However, it is expected that a very low RCS is achieved with this structure.[7] Finally, it is seen that the sensor in [74] is not optimized for miniaturization, as observed from the high l_o/λ value, since it is also based in several coupled loops so to increase the RCS and quality factor.

About the RCS issue it must be mentioned that, in fact, a reduction on the RCS was previewed from the analysis made in Section 3.4.1. It was also previewed that the ratio between the ORR and the SRR resonance frequencies influenced on this issue, as seen from the results in Fig. 4.16 where two sensors with different SRR dimensions were compared. Moreover, this ratio was dynamic, as it followed the RH variation. That is why sensitizing the whole sensor structure, the SRR and the ORR, was considered, to reduce its span and kept its value

---

[7]This might be inferred also by the very low reading distance reported in their work ($< 15\,\mathrm{cm}$).

more controlled.

Although there was a reduction in the RCS, it must be remembered that the implemented prototypes considered a very small slit in the ORR, so better radiation efficiencies are expected from bigger slits. This in fact was demonstrated with the EM simulations whose results were summarized in Table 4.1. In this table, it was also shown that the other sensor structures based on capacitive transducers would have achieved even lower RCS due to its reduced dimensions (total lateral length with respect to the wavelength). Also, very thin traces (0.25 mm) were used in the implemented sensors, so wider traces can also be used to reduce the ohmic losses.

From the measurements, it was noticed that the absolute values of the reduction in RCS were in accordance with the range previewed in Section 3.4.2. For example, the results shown in Fig. 4.18 revealed that, at low RH levels, the difference between the RCS peak from the ORR to the sensor was about 5 dB, while for higher values, it reached 8 dB approximately. Supported on the analysis based on the electrical model, the increment on the difference at higher levels can be interpreted as a gradual reduction of the SRR quality factor compared to the ORR, passing from the initial condition at low RH levels in which $Q_{SRR} > Q_{ORR}$ to the condition in which $Q_{SRR} < Q_{ORR}$ at high RH levels. Moreover, since the SRR was expected to have a higher sensitivity, the fact that their resonance frequencies were getting close to each other along the measurement intensified this RCS reduction.

In theory, it was expected that the RCS decrement reached 6 dB when the SRR quality factor equaled the ORR quality factor. This, on the contrary, was not in accordance with the theoretical analysis of the quality factor described in Section 3.2.2. Since all the estimated quality factors from the measurements of the sensor were higher than the one obtained for the ORR (without SRR), it was expected that the SRR quality factor were much larger than of the ORR.

Furthermore, from the quality factor results, it was observed that the sensor achieved a much higher value than the ORR. In the numerical calculations shown in Section 3.2.2, a maximum increment factor of approximately 1.1 was expected for a coupling factor of 0.4 (near the simulated values of k). Therefore, it seems that the theoretical predictions of the quality factor must be reviewed. It must be mentioned though that some changes in the quality factor were detected after subsequent set of measurements and tests were done with different

reading distances.[8]

---

[8]There was evidence that the coupling between the reading antenna and the sensor was influencing the results.

Figure 4.17: Comparison between implemented samples due to variability in the fabrication process ($l_{ORR} = 9.5\,\text{mm}$, $l_{SRR} = 6.5\,\text{mm}$).

(a) samples RCS
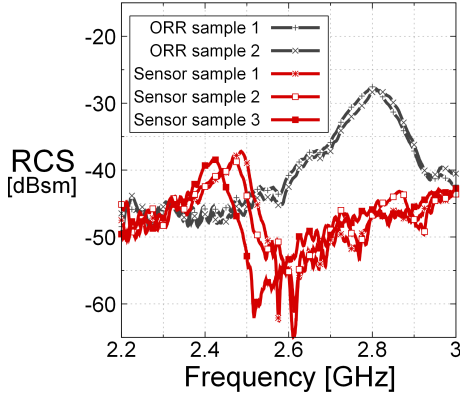
(b) SRR gap photo
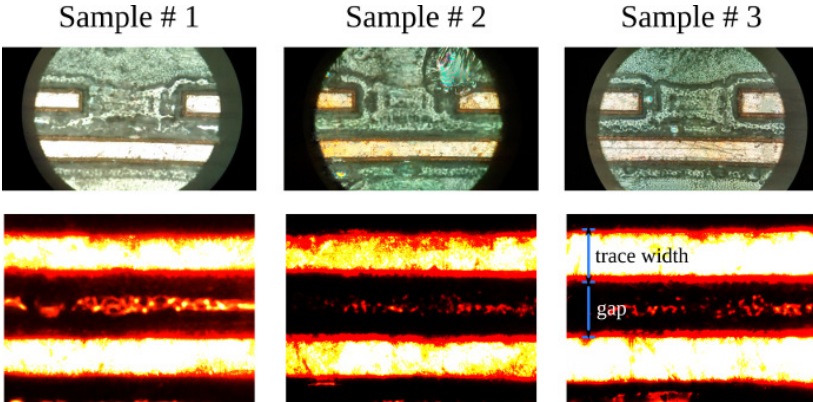
Source: The author.

Figure 4.18: Measured RCS vs time of both sensor and ORR from the silica-to-water transition experiment.

(a) Sensor

(b) ORR
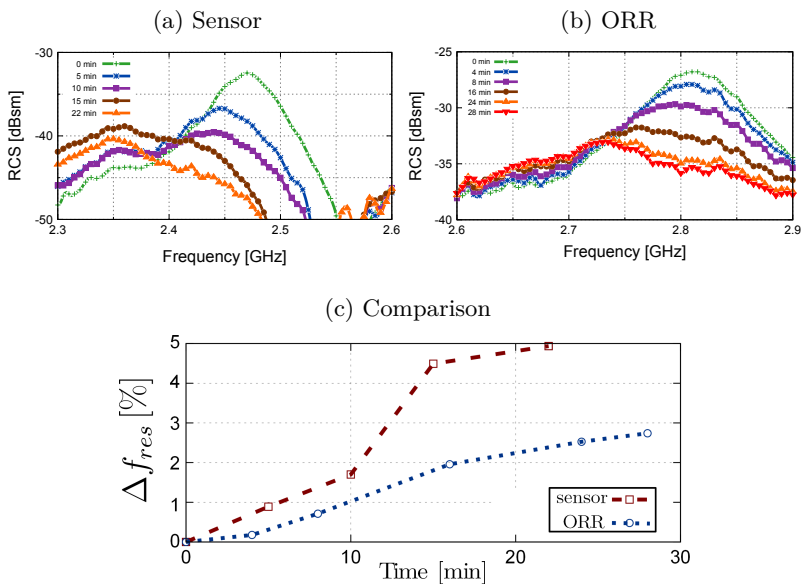
(c) Comparison

Source: The author.

Figure 4.19: Freq. response with different salts.
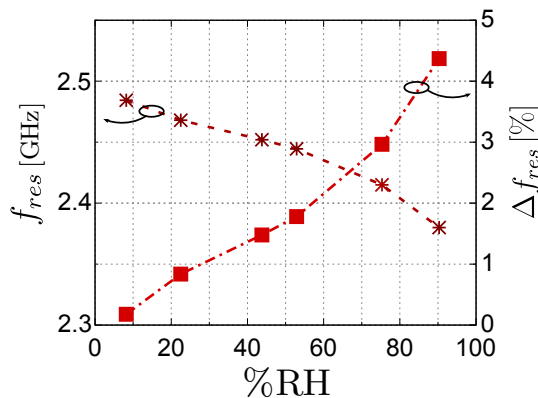
Source: The author.

Figure 4.20: Comparison between the proposed sensor and two other PVA-based capacitive chipless sensors: (a) resonance frequency and (b) normalized resonance frequency as a function of the environment relative humidity.
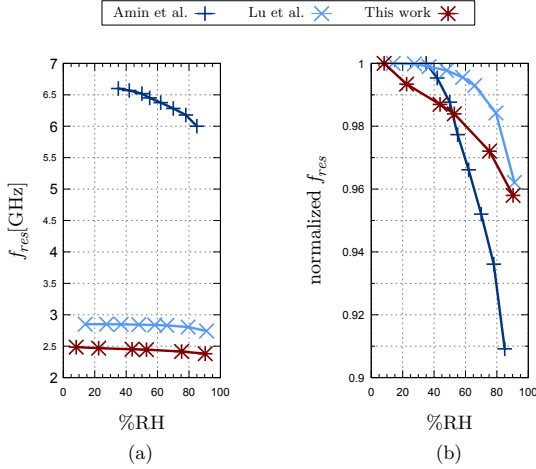
Source: The author.

Figure 4.21: Comparison between the proposed sensor and two other PVA-based capacitive chipless sensors: (a) relative resonance frequency shift, (b) absolute sensitivity, and (c) relative sensitivity at each %RH range.
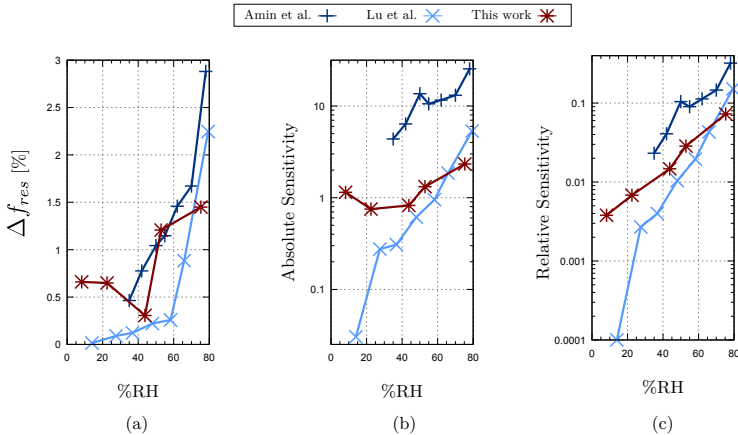
Source: The author.

Table 4.3: Comparison between reported RH chipless sensors size and sensitivity.

Sensor	l_o/λ	f_{res0} [GHz]	$\Delta\%RH$	Δf_{res} [%]	Abs. Sens.	Rel. Sen.
This work (PVA)	0.08	2.48	$8-75$ $8-90$	2.8 4.2	1.03 1.27	3.4e-3 4.2e-3
			$8-22.5$	0.66	1.15	3.8e-3
			$22.5-43.8$	0.65	0.75	6.9e-3
			$43.8-52.9$	0.31	0.82	1.5e-2
			$52.9-75.3$	1.21	1.32	2.9e-2
			$75.3-90.3$	1.45	2.33	7.3e-2
Amin et al. [32] (PVA)	0.26	6.6	$35-70$ $35-85$	4.7 9.1	8.86 12	4.7e-2 6.4e-2
			$35-42$	0.46	4.37	2.3e-2
			$42-50$	0.78	6.38	4.1e-2
			$50-55$	1.04	13.6	1e-1
			$55-62$	1.15	10.57	9e-2
			$62-70$	1.46	11.63	1.1e-1
			$70-78$	1.67	13.12	1.5e-1
			$78-85$	2.89	25.43	3.2e-1
Lu et al. [39] (PVA)	0.07	2.85	$14-71$ $14-91$	1.1 3.9	0.53 1.43	2.6e-3 7e-3
			$14-27.5$	0.01	0.03	1.5e-4
			$27.5-36.8$	0.09	0.28	2.7e-3
			$36.8-48$	0.12	0.31	4e-3
			$48-58.2$	0.22	0.61	1e-2
			$58.2-65.9$	0.26	0.95	2e-2
			$65.9-79.4$	0.88	1.85	4.3e-2
			$79.4-91.2$	2.25	5.34	1.5e-1
Vena et al. [74] (SiNWs)	0.37	3.32	$78-98$	1.01	1.68	3.9e-2

4.4 CHAPTER CONCLUSIONS

The aim of this chapter was to study the proposed sensor structure from EM simulations and RCS measurements of implemented prototypes. To this means, a layout for this sensor was presented, which is based on a square-shape ORR coupled to a SRR. EM simulations helped to understand the currents and fields distribution of this design.

Regarding the self-impedance simulation results, they showed good agreement with the electrical model proposed in Section 3 and gave support for the theoretical estimations on the sensor figures of merit. Moreover, parametric simulations of the ORR and SRR resonance regarding resonance frequency versus dimensions and sensitivity due to permittivity change were presented and discussed. Finally, simulations were also used to compare the radiation efficiency of the proposed sensor to other chipless sensors structures based on capacitive transducers.

With respect to this last issue, it was also important to notice that the proposed sensor can achieve better radiation performance that typical capacitive-based miniaturized chipless sensors, since it can control its effective length according to the size requirements of the applications. As a result, higher RCS and larger reading ranges are expected from this sensor.

Some prototypes were implemented in FR-4 substrate, which were sensitized for %RH monitoring. They showed that these sensors were capable of covering the whole ISM 2.4 GHz band, achieving similar sensitivities to other sensors implemented for the same purpose. These results were also discussed and compared to theoretical and EM simulation results.

A final comment about the sensor performance sensitivity upon fabrication process variations should be made regarding the implementation in a real application. It is known that, as in all fabrication process, there are variability issues. Therefore, repeatability in resonance-dependent structures are strictly determined by the variations of the process. However, in practice, fabrication process and material properties are well known (or controlled), so the variations and tolerances are properly characterized and quantified and thus can be taken into consideration during the design stage of the sensor. With a previous knowledge of process and materials variation, the designer should mainly guarantee that the sensors will operate within the required operating frequency band, with a given uncertainty on the absolute values. Then, calibration during the production of the sensor and also in-field calibration would

be required before using the sensor.

Taking into considerations a practical scenario, another alternative of usage of the proposed sensor would be employing it as a threshold-value detector. For example, the RCS peak of the sensor can be designed to be within a specific frequency band at relative low values of RH, and to be shifted out from this band when the RH exceeds certain value (or vice-versa). In this scenario, a good sensitivity is still important so the sensor guaranties that the peak is out of the band when required. In the case of the implemented sensor, the achieved sensitivity could be enough to cover the 2.4 GHz ISM band.

5 IMPLEMENTATIONS USING FLEXIBLE SUBSTRATES

This chapter describes the implementation of the proposed sensor structure using flexible substrates. Combinations of some substrates and conductive materials were used with the aim of gradually analyzing the effect of each element to the sensor performance, that is, to its sensitivity and, with a higher emphasis, to its radiation efficiency. The results of the prototypes implemented with paper substrate are compared to other chipless sensors presented in literature fabricated with flexible substrate. Finally, based on the results, some improvements in the design of the sensor are proposed and some experimental results are presented.

5.1 READING RANGE CONSIDERATIONS FOR THE DESIGN

The design of a FD-FC low-cost chipless sensors should start with the specification of the RCS peak (at resonance) for the desired reading range according to the application requirements. A rapid estimation can be done from the radar equation (presented in Section 2.1). It can be calculated that a minimum RCS of -50 dBsm is necessary to interrogate a chipless tag from a 1 m distance at 2.45 GHz by using a low-cost RF reader with expected sensitivity around -80 dBm.[1] As a comparison to this result, it is illustrative to estimate the case in which interrogation is made with a more sophisticated reader (e.g. a VNA whose sensitivity is expected to be better than -100 dBm). In that case, the minimum RCS reduces to -70 dBsm.

According to the previous estimations, considering the low-cost RF reader and a 10 dB safety margin, the minimum RCS peak target for the chipless sensor should be -40 dBsm for at least a 1 m interrogation distance at 2.45 GHz. Furthermore, considering the theoretical analysis of the proposed structure developed in Section 3 and the experimental results presented in Section 4, it may be convenient to add an extra 10 dB for the scatterer only, since the reduction of the RCS is previewed after coupling the sensitized resonator. In other words, the scatterer structure mus be carefully selected, so its RCS peak, within the frequency band

---

[1]This estimation considers a monostatic setup with a transmitted power of 10 dBm and a 6 dBi antenna gain.

of interrogation and within the measurand span, is 20 dB higher than the minimum required -50 dBsm RCS, that is, -30 dBsm.

It was already demonstrated that choosing a square-shaped ORR as the scatterer, even designed with a very small slit, can achieve this RCS value considering an implementation in a FR-4 substrate. However, this might not be the case if conductive materials with lower conductivity are to be used for the metal traces. Also, some low-cost substrates such as paper present higher dielectric losses. Therefore, either an adjustment on the ORR slit or a different shape must be considered in order to increase the radiation resistance and thus the RCS peak.

5.2 MATERIALS CHARACTERIZATION AND SIMULATIONS

Flexible substrates are usually low-cost, conformable, and, in some cases, biodegradable. These characteristics open the possibility to using chipless sensors in specific scenarios where RFID-based chipped sensors might not be adequate. Nonetheless, these materials are generally lossy, so it is expected that they degrade the sensor RCS and quality factor due to the dielectric losses. Moreover, additive processes for the conductive traces, which are suitable for flexible substrates, commonly generate traces with more resistivity than with common etching processes used in PCB fabrication. This means that the ohmic losses of the resonant structures that conform the sensor will also increase.

In this work, two flexible substrates were studied, one based on plastic and one based on cellulose. Specifically, for the plastic substrate, polyethylene (Melinex ST584) was used since this is suitable for printed electronics and was previously reported in similar works. For the cellulose substrate, a glossy photo-quality paper for inkjet printing from Epson was used. This choice was done after tests performed in several papers regarding inkjet printing, which are detailed in Section C of the Appendix.

Regarding the conductive traces, three cases were studied. In the first, copper conductive tape was used, as it is an interesting technique for constructing low-cost flexible circuits. The copper tape was applied both in PET and paper by following the sacrificial layer method [102] where etching was done with ammonium persulfate ((NH4)2S2O8).

In addition, inkjet printing with nanoparticle silver ink was used[2], as this emulates an industrial large-scale process of the proposed sensors

---

[2]Refer to Section C.1 in the Appendix.

[103]. Finally, an additive process based on silver paste was explored, which is also a rapid-prototyping alternative for circuits and was useful for experimental purposes where the performance of the inkjet prototypes were desired to be estimated.

In summary, four different combinations were studied from these fabrication materials and processes. These combinations are listed in Table 5.1.

Table 5.1: Combinations of substrates and conductive traces materials studied in implementation of low-cost flexible chipless sensors.

combo	substrate	conductive trace
C1	plastic	copper sheet
C2	paper	copper sheet
C3	paper	silver paste
C4	paper	silver ink

The choice of the combination C3, which uses silver paste instead of silver ink, was convenient to have a quicker and less expensive way of prototyping our sensors. However, the achievable conductivity was first investigated and compared. Several samples for this purpose were constructed for characterizing the conductivity. Even though, the silver paste prototypes were handmade which resulted in variations between samples, the best results of sheet resistance for one and two layers were 0.6 and $0.3\,\Omega/\text{sqr}$, respectively, which are comparable to the values obtained by inkjet printing. It must be also recalled that these values are at least 50 times less than etched copper used in FR-4 substrates.

The main characteristics of the flexible substrates are summarized in Table 5.2, where the FR-4 was included for comparison purposes. It is observed that the relative permittivity value of the plastic (PET) and the paper are very close. This means that resonators implemented in those substrates will present similar values of resonance frequencies. This is confirmed by EM simulations results of the SRR and the ORR as a function of their length and width dimensions, as shown in 5.1. The left and right columns show the results for the paper and plastic cases respectively. A small discrepancy between these cases are observed, which are caused by the small difference on the relative permittivity and the different thickness values. Particularly, this discrepancy is more evident in the SRR case, as expected.

Table 5.2: Main characteristics of the substrates used in the sensor prototypes. The electrical characteristics are considered at 2.4 GHz.

Subs.	Rel. Perm.	Loss tan.	Thickness [mm]
Paper	3.1	0.08	0.22
PET	2.9	0.02	0.127
FR-4	4.2	0.017	1.6

Another important difference revealed in the Table 5.2 between both substrates is that the paper presents a higher loss tangent. The larger losses and the higher thickness implies in more radiation losses for the paper prototypes.

Comparing both flexible substrates to the FR-4, it is seen that they present slightly lower values of relative permittivity. Moreover, they are much thinner. In addition, the plastic substrate presents a similar loss tangent to the FR-4. Due to its thickness, this implies in a flexible sensor implemented in plastic with less losses than in FR-4. This, indeed, does not considers the conductive traces, however, it is expected the same level of ohmic losses of combination C1 once the copper sheet conductivity is as high as in etched copper. As a conclusion. regarding radiation efficiency, one must expect that a sensor implemented with C1 combination outperforms a FR-4 prototype. Moreover, sensors fabricated with the C3 and c4 should achieved the worst performance.

Figure 5.1: Resonance frequency of ORR (maximum slit) and SRR from simulations, in PET and Paper substrate, as a function of length (l) and width (w) of the conductive trace (copper) and also gap between rings (g) in the case of SRR.
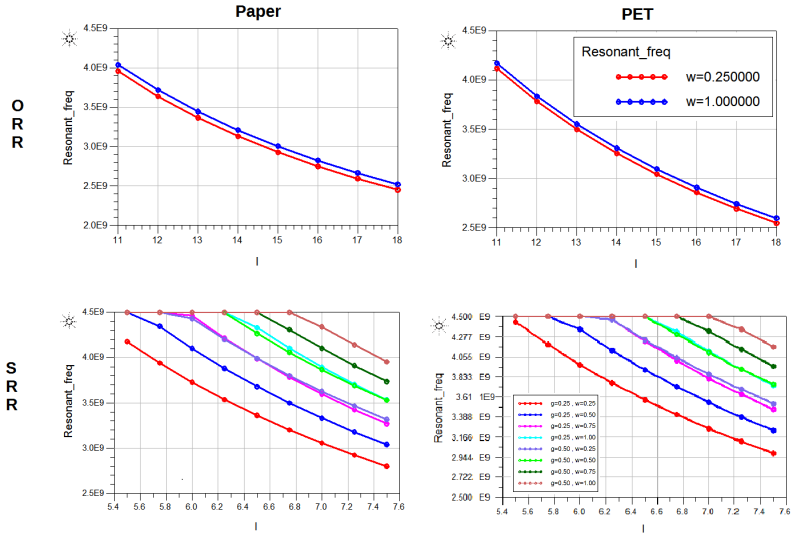
Source: The author.

5.3 IMPLEMENTATION AND EXPERIMENTAL RESULTS

5.3.1 Implementation

The first set of measurements were intended to verify if the RCS peak of the ORRs were above the specification (higher than -30 dBsm). To these means, the lossiest substrate/traces combinations, that is, C3 and C4, were chosen. Two sets of ORRs were designed to operate at very close frequencies, one with a 7.5 mm slit, and the other with maximum slit (1.5 mm), similar to the shape of a capital letter "c" (C-shape).

The same two sets of ORRs were also fabricated for combinations C1 and C2. Moreover, based on these ORRs, a SRR, designed to operate at a higher frequency, was coupled, generating the final sensor prototypes for all the four combinations. The referred prototypes are observed in

Figs. 5.2(a-d).

Figure 5.2: Some of the ORR and sensors prototypes implemented in flexible substrates (C1 sensors were placed on a black background for the photograph).

(a) C1   (b) C2

(c) C3   (d) C4
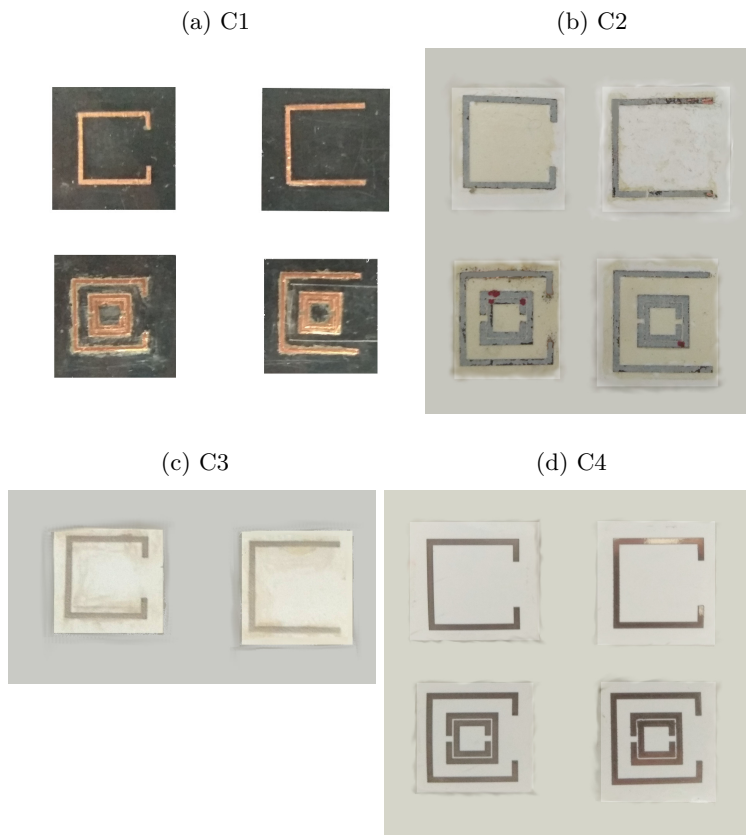
Source: The author.

5.3.2 Experimental results

5.3.2.1 RCS measurements

The following measurements results were obtained from a measurement setup similar to the one used for the FR-4 substrates. Most of the measurements were done at the same day, at the same room conditions (RH about 70%, room temperature at 25°C). The environment humidity was more critical in the case of the combinations that used paper as the substrate material, since this was more prone to variations of its electrical permittivity. A photo of the measurement setup is shown in Fig. 5.3

Figure 5.3: Photo of the measurement setup for the RCS measurement of the chipless sensors implemented with flexible substrates.

Source: The author.

The results from measurements of RCS comparing the inkjet printed ORR corresponding to combination C4, the other ORR with same dimensions fabricated with solder paste with 1 and 2 layers corresponding to combination C3, and an ORR with solder paste with C-shape (spms), also corresponding to C3, are shown in Fig. 5.4. All ORR implemented with the C3 combination resulted in higher RCS peaks. This was expected since the measured total resistance (between the ring endpoints) was 3 to 5 times lower than in the inkjet printed case. The quality factor of the printed ORR estimated from these curves resulted in 7.5[3], and in 11.5 (average) for the ORR fabricated with solder paste with the same dimensions. Furthermore, the C-shape ORR with solder paste achieved a quality factor of 10.5.

Figure 5.4: RCS measurements from ORR inkjet printed (ij), ORR of same dimensions in solder paste (sp) with 1 and 2 layers, and ORR in solder paste with maximum slit (spms).
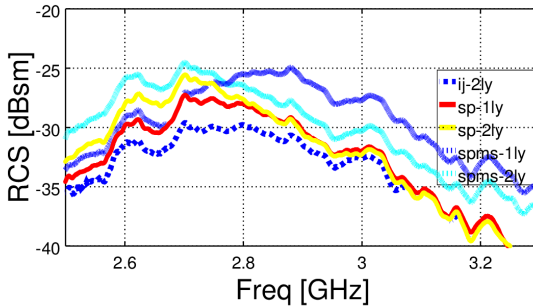
Source: The author.

In addition, the results from the ORRs implemented with combinations C1 and C2, which uses copper tape, are also shown in Fig. 5.5 for the two slit dimensions. It can be seen that the implemented resonators in paper resonate at lower frequencies due to the thicker substrate and slightly higher electrical permittivity. Nonetheless, the RCS peaks were very similar in both cases. That is, the higher losses in

---

[3]This quality factor was half of the obtained in previous measurements. The high relative humidity of the environment could have been the cause.

the paper does not present a representative impact in the case of the solely ORR's radiation resistance. Compared to the RCS levels in the tags implemented with silver paste and silver ink, it is clear that the higher resistivity of these traces impacted in a negative way. That is, there was a decay in the RCS of 5 to 10 dB only due to the ohmic losses in the conductive traces.

Figure 5.5: Measured RCS of the ORR with different substrate and conductive trace materials. Combination C1 (pet-Cu), C2 (paper-Cu) and C4 with one (paper-ip1l) and two (paper-ip2l) printed layers.
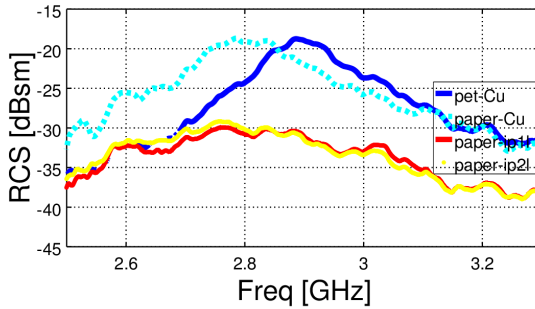
Source: The author.

The results for the sensor (after coupling the SRR) were further investigated. The cases corresponding to all combinations and the two different ORR dimensions are shown in Fig. 5.6. First, regarding the combinations C1 and C2, the effect of the dielectric losses is evident given the notorious RCS-peak differences in the paper and in the plastic case. The reason is related to the dielectric losses associated to the capacitance of the ring gaps of the SRR, which contributes to a lower quality factor of the SRR of the sensors implemented in paper. In other words, the relation Q_{SRR}/Q_{ORR} is smaller in the paper case, which causes a higher RCS decrement as previewed in Section 3.4.1. Another effect of this relation is also appreciated in the lower quality factor of the sensors implemented in paper.

Regarding the combinations C2, C3 and C4, it is seen that there is a considerable impact due to the the ohmic losses of the traces. Comparing only these losses, a decrement around 10 dB occurred after

the SRR coupling. Moreover, compared to the implementation that used the combination C1, a reduction of more than 15 dB was read. It is seen then that both dielectric and ohmic losses present a considerable impact on the final reading range of the sensor. Fortunately, even in the worst case, the sensor achieved an RCS peak greater than -40 dBsm, which remained within the specifications. However, it is also seen that the quality factor is very degraded which could limit the readability. This means that tracking the RCS could be a challenging task if the reader bandwidth total maximum processing time is limited according to the specific application.

Figure 5.6: Measured RCS of the sensor with different substrate and conductive trace materials. Combination C1 (pet-Cu), C2 (paper-Cu) and C4 with one (paper-ip1l) and two (paper-ip2l) printed layers.
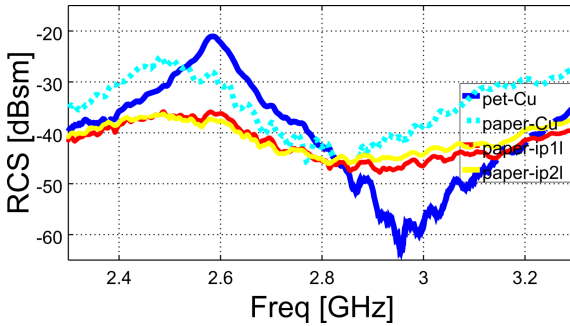
Source: The author.

The result from measurements are summarized in Tables 5.3 and 5.4. In general, the quality factor of the C-shape versions of the ORRs were smaller but with a higher RCS peak, as expected. Among all sensors, combination C1 resulted in the most distinguishable RCS peak. The performance of the copper-traces based sensors (C1 and C2) presented similar RCS values, however the losses of the paper substrate further degraded the quality factor of these correspondent implementations. Finally, it was verified that combination C4 is the worst case in terms of radiation efficiency, as expected.

In Table 5.5, a quantitative comparison of the effect o the SRR coupling obtained from the measurement is made. The maximum reduction on RCS was about to 7.3 dB, corresponding to the C4 case. This result is within the 10 dB range expected from the electrical model and previous experimental results with FR-4 substrate. Another interesting fact is that in the C1 and C2 sensor cases, the downshift was higher

Table 5.3: Measurement results summary of the ORRs implemented in flexible substrates.

Implementation	RCS_{peak}	f_{res} [GHz]	3 dB BW [MHz]	Q-fact.
C1	-18.7	2.886	125	23.1
C1 (C-shape)	-18.1	2.885	167	17.3
C2	-18.7	2.785	174	16
C2 (C-shape)	-17.1	2.784	198	14.1
C4 (2-lay)	-29.2	2.758	350	7.9

Table 5.4: Measurement results summary of the sensors implemented in flexible substrates.

Implementation	RCS_{peak} [dBm]	f_{res} [GHz]	3 dB BW [MHz]	Q-fact.
C1	-21.1	2.585	55	47.6
C1 (C-shape)	-21.5	2.678	147	18.3
C2	-25.2	2.483	115	21.6
C2 (C-shape)	-21.3	2.591	93	28
C4 (2-lay)	-36.5	2.482	290	8.6

for the non-maximum slit case. Considering that almost the same self-resonance of the ORR was obtained in both ORR sets, the C-shape case was expected to have a lower coupling factor k since the SRR was farther from the ORR midpoint. The effect on the bandwidth and quality factor was also included in the table through the correspondent calculated ratios from both cases, that is: BW_{SRR}/BW_{sensor} and Q_{SRR}/Q_{sensor}. A very high Q ratio (≈ 2) resulted from the C1 non-maximum slit case and the C2 C-shape case.[4]

Table 5.5: Effect of the SRR coupling in the proposed sensors, compared to the correspondent ORRs.

Implementation	ΔRCS_{peak} [dB]	f_{res} ratio (α)	BW ratio	Q-fact. ratio
C1	2.4	0.896	0.44	2.061
C1 (C-shape)	3.4	0.928	0.88	1.058
C2	6.5	0.892	0.66	1.35
C2 (C-shape)	3.2	0.931	0.47	1.986
C4 (2-lay)	7.3	0.899	0.83	1.089

5.3.2.2 Sensitivity measurements

Paper substrates present an inherent responsivity for humidity applications. Particularly, the photo-quality papers explored in this work present a porous plastic-based surface for better imaging quality when printing. These surfaces present some response to the humidity of the environment [44]. Therefore, tests with salt references were done for the sensors of combination C2 and C4 (7.5 mm ORR slit). Two salt solutions were used as RH% references for these tests, sodium hydroxide (NaOH) and Magnesium Nitrate (Mg(NO3)2), that correspond to 8 and 53 RH% at 25°C, respectively.

The results obtained with the sensor implemented with the C2 combination are shown in Fig. 5.7. Furthermore, the results for the C4 case are shown in Fig. 5.8. Some of the measurement results are presented in Table 5.6, which also includes the ORR with the C2 combination for comparison. The average values for each implementation are highlighted.

From the measurements, it was calculated an average normalized frequency variation of 1.5% and 0.46% for the C2 and C4 implementations, respectively. Moreover, these values corresponded to a relative sensitivity of 2.7e-3 and 8.3e-4, respectively. These results are on the same order of magnitude of the FR-4 implementation for the same %RH range (1.6% and 3e-3), however, the C4 paper implementation performance was inferior.

---

[4]These quality factor and BW results are not conclusive since further study of the effect of the reader antenna loading must be done.

Figure 5.7: Measured RCS of the sensor response implemented with C2 combination (copper tape trace and Epson paper substrate) at two different salt solution references.
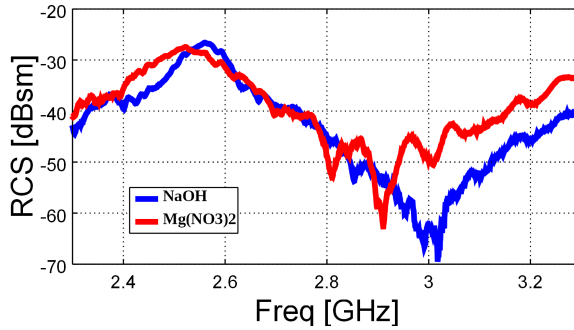
Source: The author.

5.3.3 Discussion of the results

First of all, the results from all prototypes implemented in flexible sensors confirmed what was expected from the material electrical properties. The results were also according to the theoretical analysis of the sensor based on its electrical model. This fact is important for the sensor design, as a complete characterization of the materials allows, up to certain degree of accuracy, to preview the sensor performance. Furthermore, it is interesting to compare the prototypes with other sensors presented in literature. From the reviewed state-of-the-art work presented in Section 1.3 of the first Chapter, only three references were found which presented FD-FC chipless sensors implemented with flexible substrates [76, 74, 44]. All of them were reported as humidity sensors.

The sensor presented in [76] was based on a Van-Atta antenna array. It was implemented in a polyimide film (Kapton HN - Dupont) with nominal relative electrical permittivity of 3.1 and loss tangent of 0.003. This flexible plastic substrate is also sensitive to humidity. The array was inkjet printed using 3 layers of silver nanoparticle (SNP - Suntronic) and a Dimatix DMP 2831 inkjet printed. Finally, the substrate was grounded with a copper tape.

The authors in [44] presented a chipless sensor based on three concentric loop resonators with the intention of monitoring the RH at three different frequency values. A 3×3 array of these resonators were inkjet printed in a humidity-sensitive paper (NB-P-3GU100 -

Figure 5.8: Measured RCS of the sensor response implemented with C4 combination (1 layer of silver nanoparticle ink and paper substrate) at two different salt solution references.
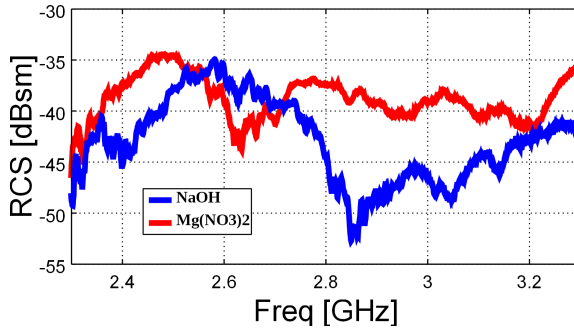
Source: The author.

Mitsubishi), and then glued to a grounded cardboard substrate. The silver nanoparticle ink (Mitsubishi) did not need any heating process for the sintering, and was printed with a conventional inkjet printer.

Finally, the work in [74], which was used as comparison with the FR-4 substrate in he previous section, was also cited here. This work showed a chipless sensor based on nested coupled loop resonators. Both the substrate and conductive traces materials were not specified. Only the sensitive material, silicon nanowires, is mentioned.

A comparison between these works and the implementations of the proposed sensor in paper is made in Table 5.7. It is seen that this work proposes a very miniaturized sensor, whose occupied are is a least one order of magnitude lower if it were normalized to the equivalent wavelength. All the rest of the works are based on arrays of the same structures in order to increase the RCS. Notoriously, the implementation in [76] is the biggest in size, which translates to the highest RCS average peak. This structure achieves a high relative sensitivity due to the patch antenna-based structure together with the plastic material employed.

Regarding the paper implementation presented in [44], this sensor does not present RCS measurements for that prototype. However, as the sensor structure is grounded, the sensing mechanism is based on detecting the RCS valley rather than its peak. So, the average RCS (no valley) value obtained from the simulation of a FR-4 implementation was used instead as reference in the table. This work achieved a good relative sensitivity for the range between 60 nd 90 %RH.

Finally, it is seen that the sensor presented in [74] is an alternative

for a good relative sensitivity and a reasonable size. Nonetheless, its RCS peak is the lowest among all the rest of the sensors, so its reading range should be compromised in practical applications.

Both implementations in paper of the proposed sensor achieved an RCS peak within the desired specifications. Even though, a sensitivity characterization of these prototypes within a wider %RH range was missing, regarding the relative sensitivity results obtained, it can be estimated that a total resonance frequency shift of 66 MHz and 20 MHz around 2.45 GHz would result from a 8 to 90 %RH range considering the C2 and C4 implementations, respectively.

With the intention of summarizing the main results cited previously, in the last two columns of the Table 5.7, two figure of merits were added. The first takes only into account the radiation efficiency in terms of the RCS for occupied unit of area (FoM_1 = RCS/area). The second complements this one with the relative sensitivity (FoM_2 = Rel.Sen. $\times$ RCS/area).

It is observed that both prototypes implemented in this work are superior regarding FoM_1. This is due to its miniaturization degree. Furthermore, when sensitivity is taken into consideration in FoM_2, only the implementation with combination C2 and C4 are the second and forth in performance respectively. Regarding this last figure of merit, the works in [44] and [76] achieved better results, however, it should be recalled that those designs require more fabrication steps due to the grounded structure and their relative cost due to fabrication process and conductive material per occupied area could be higher.

Finally, it is important reinforce the fact that not easy to make a fair comparison between all the cited works since neither the same measurement setup nor %RH and temperature range nor the sensitive material nor costs nor the operating frequency are considered. Therefore, the results from this comparison exercise should be carefully interpreted.

5.3.4 Improving performance of sensors in paper: increasing coupling factor and modifying scatterer shape

Based on the previous results, some techniques were considered to enhance the performance of the implementations of the sensor in flexible substrates, more specifically, in the case of paper as the substrate. The main goals were to enhance both the RCS and the sensitivity through specific modifications in the sensor design. These include increasing the coupling of the scatterer and the resonator, and increasing the radiation

efficiency of the scatterer. Both techniques were explored, as described below.

From the theoretical analysis of the sensor sensitivity made in Section 2.3.1, a higher sensitivity is expected from a higher coupling factor between the scatterer and the resonator (k). From EM simulations, it was already proved that a higher k resulted if the SRR's outer ring slit was oriented so it faces the midpoint of the ORR (0). Moreover, it was verified in Section 4.1.2 that getting closer the resonator to this midpoint increased the coupling factor.

Two prototype of the sensor were implemented with the C3 combination, which provided with a good estimation of the performance of the a printed sensor in paper (combination C4). A C-shape ORR was chosen to increase the RCS while keeping a miniaturized design. Also, the coupling factor was enhanced by placing the SRR closer to the ORR midpoint, as shown in Fig. 5.9(a). The RCS measurement results are shown in Fig. 5.9(b-c) for several distances from the reader.[5] These results confirmed that a higher coupling factor exists given the lower resonance frequency, compared to the previous C4 implementation. Moreover, the RCS peak values are also similar (see Fig. 5.6), which means that the effect of increasing the slit size balanced the losses increment expected from the higher coupling factor. As a result, a higher sensitivity compared to the previous implementation with paper is expected from this new design while keeping similar RCS values.

The second technique applied to enhance the sensor performance regarding its RCS was to modify the scatterer shape. It is known that the scatterer is more effective as it approximates to an ideal dipole.[6] Therefore, a new sensor design based on this idea was implemented, as shown in Fig. 5.10(a). It is seen that a rectangular ORR instead of an square-shape ORR was included. Moreover, the SRR was also designed to be close to the ORR midpoint to increase the coupling factor and enhance the sensor's sensitivity.

The measured RCS results are shown in Fig. 5.10(b). Much higher levels of RCS are observed compared to the implementation of Fig. 5.9. Nonetheless, also a lower quality factor was obtained, due to the new scatterer shape. As a result of its higher radiation resistance, this implementation shows the possibility of increasing the reading range, however, at the expense of more usable area for the sensor and higher RCS peak bandwidth.

---

[5]A discussion of the measurement setup and the reading distance is presented in Section B of the Appendix.

[6]Refer to Section 2.4.

Figure 5.9: Measured RCS at different distances of implemented sensor with C3 combination considering enhanced coupling factor.

(a) Implementation of higher k prototype
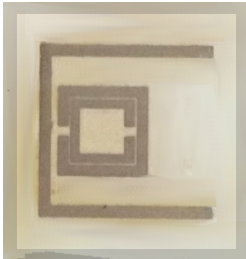
(b) 1 lay.
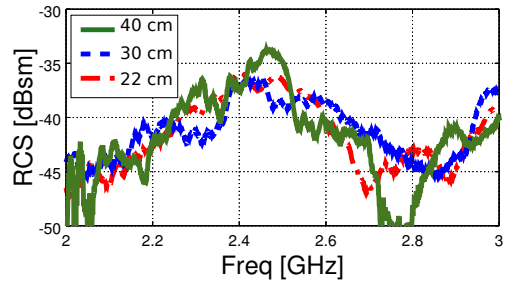
(c) 2 lay.
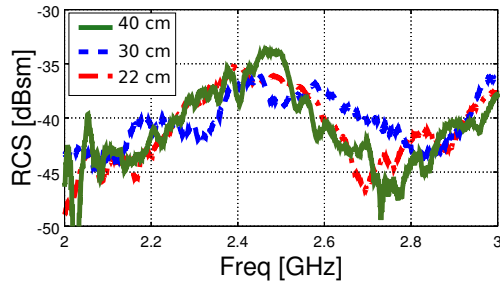
Source: The author.

Figure 5.10: Measured RCS at different distances of implemented sensor with C3 combination considering enhanced coupling factor and higher RCS scatter.

(a) Implementation of rectangle-shape ORR

(b) RCS
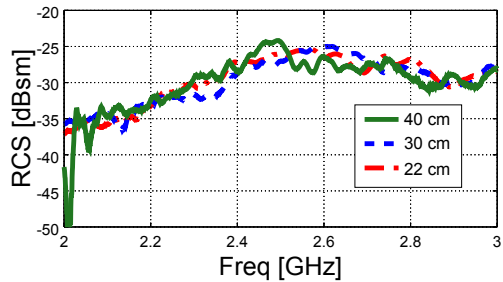
Source: The author.

Table 5.6: Some of the measurement results from tests with salts

Implementation	RCS_{peak}	f_{res} [GHz]	3 dB BW [MHz]	Q-fact.
ORR C2	-23.56	2.872	163	17.6
NAOH	-23.6	2.872	164	17.5
	-24.27	2.872	165	17.40
	-24.3	2.872	165	17.40
	-23.93	**2.872**	**164.25**	**17.5**
sensor C2	-26.59	2.56	87.5	29.3
NAOH	-26.44	2.56	86	29.8
	-26.63	2.563	85.5	29.9
	-26.45	2.56	84	30.5
	-26.53	**2.561**	**85.75**	**29.9**
sensor C2	-27.47	2.521	127	19.9
MgNO	-27.59	2.521	119	21.2
	-27.42	2.523	111.5	22.6
	-27.26	2.525	108.5	23.3
	-27.44	**2.522**	**116.5**	**21.7**
sensor C4	-34.93	2.581	114	22.8
NAOH	-35.05	2.584	117.5	22
	-35.32	2.56	148	17.3
	-34.82	2.561	133	19.3
	-34.57	2.571	125	20.6
	-34.94	**2.571**	**127.5**	**20.4**
sensor C4	-35.19	2.499	178	14
MgNO	-34.45	2.479	158.5	15.6
	-34.82	**2.489**	**168.25**	**14.8**

Table 5.7: Comparison between RH chipless sensors implemented in flexible substrates.

Sensor	Sens. material & subst.	dim. [mm^2]	area$/\lambda_0^2$	tested %RH range	$\overline{RCS_{peak}}$ [dBsm]	Rel. Sens.	FoM$_1$	FoM$_2$
This work (C2)	paper	12×12	0.01	$8-53$	-26.5	2.7e-3	16.3	4.4e-2
This work (C4)	paper	12×12	0.01	$8-53$	-34.9	8.3e-4	2.4	1.9e-3
[76]	plastic	50×60	26.9	$10-75$	-23	1.5e-2	1.9	2.7e-2
[44]	paper	45×45	0.2, 0.8, 1.2[a]	$60-90$	-20[b]	6.7e-2	0.83	5.6e-2
[74]	n.r., SiNWs	12×34	0.37	$78-98$	-46	3.9e-2	8.2e-3	3.3e-4

[a] For each of the frequency bands.
[b] Estimated from the simulated value presented.

5.4   CHAPTER CONCLUSIONS

The aim of this chapter was to show the performance of the proposed sensor structure when implemented with flexible substrates. For this purpose, different prototypes regarding four combinations between plastic and paper substrates and copper and silver traces were explored. Some design modifications were explored compared to the FR-4 implementation shown in the previous chapter. These included the use of wider conductive traces and the augment of the ORR slit dimensions.

Measurements confirmed that plastic implementations were the best in performance due to the reduced losses and thinner dimensions compared to paper substrate. Also, the reduced performance was expected from the silver traces, both based on nanoparticle ink and paste, compared to the copper conductive tape-based traces. Nonetheless, it was verified that even the sensor implemented with the lossiest materials (paper plus printed silver ink), presented a RCS peak above -40 dBsm, which means it could be able to be interrogated it from a 1 m distance using a low-cost reader operating at 2.45 GHz.

The two prototypes implemented in paper were compared to other sensors implemented with flexible substrates reported literature. These prototypes achieved a lower relative sensitivity performance for the tested RH range. However, if the size is considered, they achieved similar and, in some cases, higher performances than the rest.

An interesting fact was to confirm that only very few implementations of FC chipless sensors have been reported using flexible substrate. Specifically, only three citations were found in which paper was the substrate. Moreover, none of the reported sensors have presented such miniaturized structures as proposed in this work. Both facts are attributed to the difficulty of interrogating the sensor considering lossy materials.

Finally, it was verified that the sensor prototype which was printed on paper can be improved through some changes in the design. These include the enhancement of the SRR coupling and the modification on the ORR shape. Preliminary experimental results showed that those modifications could, indeed, improve the sensor performance.

6 EFFECT OF THE SELF-INTERFERENCE IN CW CHIP-LESS READERS

In a typical chipless radio-frequency identification system, the reader sends a modulated/unmodulated electromagnetic wave to the chipless tag and then measures the backscattering signal, which is modified by the tag's EM signature [37]. Despite many studies have been published about chipless tags, the reader, given its challenging role of detecting the weak unmodulated backscattered EM signal from the tag, remains an open subject of research. Consequently, most of the reported chipless tags, both for identification and sensing, have been characterized employing costly laboratory equipment and high-gain directive antennas, usually within well-controlled measurement environments [104]. Still, some reader architectures and signal-processing techniques have been proposed for reading chipless tags in real-life scenarios [105, 106, 28, 107, 104, 67, 108, 54, 40, 59, 61]. Recent implementations of these readers consist of off-the-shelf components [57, 46, 109, 110, 33, 111], high-cost dedicated Integrated Circuit (IC) [50, 112] or low-cost development boards [113, 114].

It is important to say that all the implementations cited above used either two-antenna monostatic or bistatic configurations. Particularly, single-antenna monostatic setups are preferred when compact implementations are needed [115]. Nonetheless, single-antenna setups are more prone to the *self-interference* effect,[1] due to the presence of a disturbance signal at the receiver chain caused by the leakage of the high-power output signal of the transmitter. This interference limits the sensitivity, and, thus, the reading range of the system [116, 117, 118]. In fact, this is a critical issue in a chipless RFID system, since the tag remains static and no Doppler effect occurs, differently to a traditional continuous wave (CW) radar application. Therefore, monostatic chipless RFID systems require the implementation of a Self-Interference Cancellation (SIC) technique, not only in single-antenna but also in two-antenna setups where large reading distances are desired [119].

In this chapter, the sensitivity performance of monostatic chipless readers applied to frequency-domain tags in which the reader architecture include a SIC technique is studied. Previously reported analyses on the distance range for detection of a chipless tag have only con-

---

[1]Also known as self-jamming.

sidered bistatic and two-antenna monostatic configurations in which self-interference was neglected [120, 37]. However, in monostatic architectures, the sensitivity term in the radar equation becomes now a function of the transmitted power. Therefore, new theoretical expressions for the maximum reading range as a function of the SIC circuit performance when the reader is limited either by its noise floor, specifically the transmitter leakage noise, or by the dynamic range due to the transmitter leakage signal are necessary. Finally, as a case study, a single-antenna monostatic reader based on a Software Design Radio (SDR) platform and a dedicated SIC circuit was implemented and measurement results are compared to the expected theoretical calculations.

6.1 INTERFERENCE SOURCES IN CHIPLESS READERS

In a typical reader with FSCW radar architecture as the one represented in Fig. 6.1, when the chipless tag is assumed static, the downconverted signal at the receiver produces a DC signal. This fact may limit the readability of the tag due to the large DC-offsets and low-frequency noise caused by the front-end circuit elements. To surpass this issue, a sub-carrier modulated CW signal can be used instead, so the downconverted baseband signal is shifted to a higher frequency.

Nonetheless, in a real-life scenario, the signal at the receiver is composed of the sum of the signal retrieved from the tag plus others caused by interferers, as represented in Fig. 6.2. Therefore, the downconverted signal of the chipless tag (at each frequency step) can be expressed as

$$V_b(t) = V_{tag}(t)e^{j\omega_m t} + V_{int}(t), \qquad (6.1)$$

where ω_m is the sub-carrier angular frequency. The first term $V_{tag}e^{j\omega_m t}$ refers to the downconverted signal information from the tag, where $V_{tag}(t)$ is given by

$$V_{tag}(t) = A_{tag}e^{j\phi_{tag}}, \qquad (6.2)$$

that is, it is proportional to the tag EM signature which is related to the amplitude (A_{tag}) and phase (ϕ_{tag}) information at each frequency step. The second term, $V_{int}(t)$, refers to the signals originated from interferers which can be either external or internal to the reader.

On the one hand, the main external sources of interference are the random signals from other communication systems working at near frequencies and the backscattered echo from the environment or object

Figure 6.1: FSCW chipless reader architecture and main signals. A: RF transmitted signal; B: RF received signal; C: downconverted received signal.
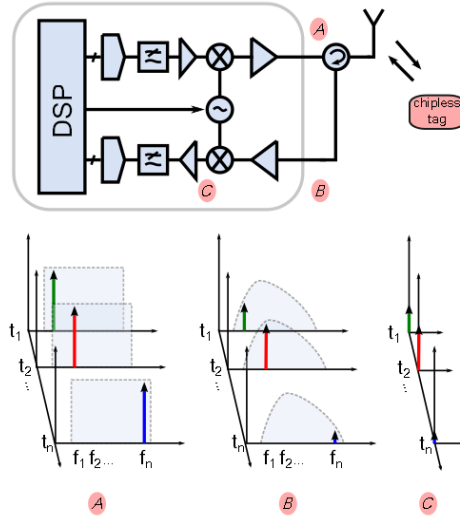
Source: The author.

attached to the tag, known as the *clutter*. On the other hand, the internal source of interference is the transmitter itself, which leaks both a high-power signal and noise to the receiver through all the possible paths expected from component reflections and non-ideal isolation in the RF path [117]. This combination of unwanted signals are referred as the *transmitter leakage*. As a result, the downconverted signals from the interferers can be expressed as the sum of the random interferers (V_r), clutter (V_c) and transmitter leakage (V_l), i.e.,

$$V_{int}(t) = V_r(t) + \left(V_c e^{\phi_c} + V_l e^{\phi_l}\right) e^{j\omega_m t}. \tag{6.3}$$

While random external interferers are likely to be mitigated by digital signal-processing algorithms [105], clutter and transmitter leakage are the most critical unwanted signals since they occupy the same frequency spectrum of the retrieved signal from the tag, especially the latter, since is a very high-power signal. Therefore, the main challenge of the reader is to distinguish the tag from these two interferers.

The clutter effect can be avoided by following the three-step calibration method in [99], although this technique is impractical for a real scenario. Alternatively, cross-polarized interrogation can be used

Figure 6.2: External interferers and self-interference signal that cause reading range degradation in single-antenna monostatic chipless readers.
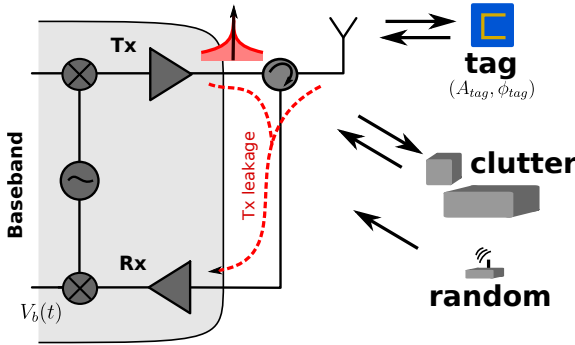
Source: The author.

together with depolarizing tags and/or digital signal processing techniques where just a single [50, 51, 52, 122, 123, 50] or even no calibration measurement may be required [121].[2]

Regarding the transmission-to-receiver high-power leakage signal, this can drastically affect the dynamic range of the receiver, resulting in desensitization or voltage clipping of the RF blocks. Furthermore, not only the transmitted signal is leaked but also its noise. The transmitter leakage is a very well-known issue in monostatic architectures such as in high-performance RFID readers and radars, which have been addressed by means of SIC techniques [117], which has also gain recent attention in transceivers' design for full-duplex (FD) communication [116]. In the case of the chipless reading system, the employed SIC technique should guarantee that the RF front-end does not saturate and that the leakage noise is below the backscattering signal level from the tag [119]. This issue is analyzed in the next section.

---

[2]Imperfect cross-polarization interrogation due to real antennas should be expected in practice.

6.2   READING RANGE CONSIDERING THE TRANSMITTER LEAK-
AGE AND A SIC TECHNIQUE

6.2.1   Leakage noise analysis

In a chipless reader with monostatic configuration and sub-carrier modulated FSCW, as discussed previously, considering that the clutter can be highly attenuated by depolarizing tags [50] and/or by digital signal-processing techniques [105, 121, 113], we may assume that the main interferer is given by the transmitter leakage $(V_{int}(t) \approx V_l e^{j\omega_m t + \phi_l})$. When the reader includes the implementation of any SIC technique, the leakage signal is expected to be reduced in 20 to 40 dB, as shown in typical implementations [116, 117]. With regard to all these facts, one can express the reader's sensitivity as

$$S_r = SNR_o N_i, \tag{6.4}$$

where SNR_o is the minimum required signal-to-noise ratio (SNR) at the input of the baseband signal processing unit, and N_i is the total input-referred noise at the antenna, which can be written (neglecting the phase noise of the transmitter) as [119]

$$N_i = N_i^{th} + N_i^l, \tag{6.5}$$

where N_i^{th} represents the contribution of the intrinsic thermal noise of the receiver chain and N_i^l corresponds to the leakage noise from the transmitter chain.

The thermal noise term is given by

$$N_i^{th} = k_B T_0 BW NF_{rx}, \tag{6.6}$$

where k_B is the Boltzmann constant, T_0 is the operating temperature (in Kelvin), BW is the channel frequency bandwidth, and NF_{rx} is the noise figure of the receiver chain. Moreover, the leakage term can be written as

$$N_i^l = \frac{N_{tx}}{\alpha_{sic}\alpha_{iso}}, \tag{6.7}$$

where the transmitted noise power $(N_{tx} = P_{tx}/SNR_{tx})$ is a function of the transmitted signal power (P_{tx}) and the SNR of the transmitter (SNR_{tx}), α_{sic} is the attenuation factor attained by the SIC circuit, and α_{iso} is the value of the intrinsic isolation of a monostatic system

(referred to the antenna), which, depending on its configuration, may be written as

$$\alpha_{iso}^{-1} = \begin{cases} I_{cc}^{-1} + |\Gamma_a|^{-2} & \text{, single-antenna w/ circulator;} \\ C_{cp}/I_{cp} + |\Gamma_a|^{-2} & \text{, single-antenna w/ coupler;} \\ I_a^{-1} & \text{, two-antenna;} \end{cases} \tag{6.8}$$

where Γ_a represents the voltage reflection coefficient of the reader antenna, C_{cp} is the coupling factor of the coupler and I_{cc}, I_{cp} and I_a represent the isolation factors of the circulator, coupler, and between antennas, respectively.

Alternatively, the noise leakage term can be expressed as

$$N_i^l = \frac{P_{tx}}{\alpha_{iso} FOM_r}, \tag{6.9}$$

where $FOM_r = \alpha_{sic} SNR_{tx}$ is a figure of merit related to the reader [119]. As a result, the maximum reading range calculated from the sensitivity expression obtained from the radar equation (assuming line-of-sight propagation) is equal to

$$d_{(max)}^{tn} = \sqrt[4]{\frac{P_{tx} G_a^2 \delta_{pol}}{S_r} \frac{\lambda^2 RCS}{(4\pi)^3}}, \tag{6.10}$$

where G_a is the antenna gain, δ_{pol} is an attenuation factor due to polarization mismatch between the antenna and the tag. The superscript *tn* makes reference to the *total noise*.

Similar to an analysis made for an RFID chipped system [119], provided a transmitter power level (P_{tx}), the sensitivity will be determined either by the thermal noise or by the transmitter leakage noise. When this power is low, the thermal noise is the dominant noise source, thus, the traditional equation from the radar equation can be used.[3] However, when it is high, the leakage noise dominates. The transition between both conditions depends on α_{iso}, α_{sic}, and SNR_{tx}. Moreover, the leakage noise is expected to be more severe in single-antenna monostatic readers, since the isolation factor α_{iso} is typically lower, and the reader sensitivity becomes more dependent on the SIC circuit performance (see (6.9)). Therefore, for $N_i^{th} << N_i^l$, (6.10) is reduced to

$$d_{(max)}^{ln} \approx \sqrt[4]{\frac{FOM_a FOM_r}{SNR_o} \frac{\lambda^2 RCS}{(4\pi)^3}}, \tag{6.11}$$

---

[3]Refer to (2.2) in Section 2.1.

where $FOM_a = \alpha_{iso}\delta_{pol}G_a^2$ is the antenna figure of merit. Here, the superscript *ln* emphasizes that this equation considers only the *leakage noise*.

Equation (6.11) is in agreement with the expression obtained in [119][4]. Nevertheless, in chipless RFID tag measurements, not only the transmitter thermal noise must be considered but also its phase noise, since it produces a residual noise after downconversion of the signal backscattered from the tag due to the so-called *range correlation effect* [124]. Then, the phase-noise should be taken into account by including it in the SNR_{tx}, i.e., $N_{tx} = N_{tx}^{th} + N_{tx}^{ph}$. This component is equal to the total integrated phase noise within the band of interest

$$N_{tx}^{ph} = \int_{f_n}^{f_n + \Delta f} S_{ph}(f)\alpha_{ph}(f)df, \qquad (6.12)$$

which is dependent on the phase-noise power spectrum of the transmitter signal ($S_{ph}(f)$) and the range correlation factor $\alpha_{ph}(f) = 4\sin^2\left(\pi f \tau_{rt}\right)$, where τ_{rt} is the round-trip delay time of the CW interrogating signal that impinges on the tag.

6.2.2 Leakage signal power analysis

Besides the impact of the transmitter leakage noise, its high-power leakage signal must be analyzed as well. For instance, it is necessary that the downconverted signal is digitized with enough accuracy at the input of the digital processing unit. We can express this requirement by relating the minimum resolvable step of the Analog-to-Digital Converter (ADC) at the end of the receiving chain and the minimum SNR at processing unit:

$$\frac{FSV}{2^{ENOB}} < \frac{G_b V_{tag}}{\sqrt{SNR_{o(min)}}}. \qquad (6.13)$$

The left term represents the least significant bit value given by the ratio of the full-scale voltage (FSV) and the effective number of bits ($ENOB$) of the ADC, and G_b is the baseband voltage gain of the receiver chain (baseband amplifier plus filter).

The maximum achievable value of the baseband gain without saturating the baseband reception chain is limited by the sum of amplitudes of the downconverted signals retrieved from the tag (V_{tag}) and

---

[4]For chipped tags, $RCS = G_{tag}^2 \eta_{MOD} \lambda^4 / 4\pi$.

transmitter residual leakage signal (V_l) due to the SIC circuit. Typically, the portion due to the tag is very weak compared to the residual leakage signal, so $V_l + V_{tag} \approx V_l$. Therefore,

$$G_{b(max)} \approx \frac{FSV}{V_l}. \tag{6.14}$$

Furthermore, it can be stated that

$$V_l^2/V_{tag}^2 = P_i^l/P_i^{tag}, \tag{6.15}$$

where $P_i^l = P_{tx}/\alpha_{iso}\alpha_{sic}$ is the leakage power from the transmitter referred at the antenna, and P_i^{tag} is the input power due to the tag backscattering signal deduced from the radar equation. Finally, by substituting G_b and V_{tag} in (6.13) using (6.14) and (6.15), the maximum reading range can be determined from

$$d_{(max)}^{dr} = \sqrt[4]{\frac{FOM_a\alpha_{sic}\,4^{ENOB}}{SNR_o}\frac{\lambda^2 RCS}{(4\pi)^3}}, \tag{6.16}$$

where the superscript *dr* indicates its relation to the *dynamic range*.

We should notice that (6.16) is similar to (6.11), both being affected by the SIC attenuation factor. In the case of a reader where $SNR_{tx} > 4^{ENOB}$, the reading distance would be restricted by the power of the transmitter leakage signal rather than its leakage noise.

At this point, it is important to remark that the downconverted leakage signal is typically not a relevant issue in traditional RFID chipped tags since this signal is downconverted at a different frequency, lower than the backscattering link frequency of the tag. Thus, it could be filtered out before reaching the ADC.

6.3   CASE STUDY

6.3.1   Reader implementation and measurement setup

We implemented a chipless reader based on the USRP B210 SDR platform from Ettus Research™, which integrates two transceiver channels with a direct conversion architecture [126]. Self-interference cancellation was achieved by using both channels' transmitters plus an external circuit board comprising a microstrip directional coupler and a Wilkinson power combiner, as shown in Fig. 6.3. The combiner adds

the leakage signal from the main transmitter to the second transmitter output signal. The latter is calibrated in phase and magnitude in order to reduce as much as possible the power level of the leakage signal. Additional information on the functioning principle of similar SIC circuits can be found in the literature [117].

Figure 6.3: PCB implemented on low loss substrate (RT Duroid 5880 - Rogers) for the self-interference cancellation in the chipless reader.
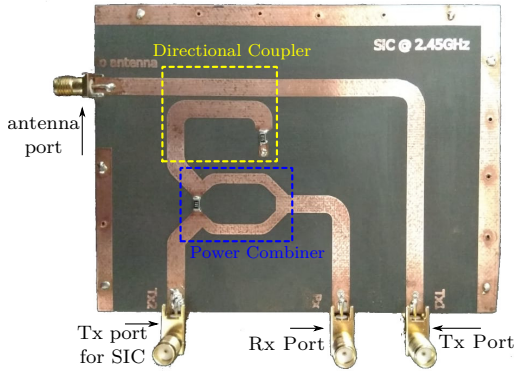
Source: The author.

A photograph of the reader is shown in Fig. 6.4(a). The maximum allowed power at the receiver input port as specified by the manufacturer was taken into account for the design of the directional coupler. The most relevant measured parameters of the SIC board are shown in Fig. 6.4(b). It can be seen that the average coupling and isolation factors were 17 dB and 25 dB, respectively, and the return loss at the transmitter port was greater than 15 dB. In addition, a LogPeriodic Dipole Array (LPDA) antenna was fabricated, which presented a simulated gain of 6 dBi approximately and a measured voltage reflection coefficient lower than −11 dB between 2.2 and 2.8 GHz. According to (6.8), these results equal to an isolation factor (α_{iso}) of approximately 6 dB.

In the measurements, an open-ended patch antenna was used as the chipless tag [125]. The RCS signature of this tag presented an RCS valley of -35 dBsm at the patch resonance, as shown in the RCS plot of Fig. 6.5(a), which was obtained with a Vector Network Analyzer (VNA) and two reflectors with different dimensions as references. The measurements were obtained at a 20-cm distance from the tag to the center of the LPDA antenna.

Figure 6.4: (a) Photo of the implemented reader and (b) measured parameters of the microstrip SIC board: reflection coefficient seen at the Tx port (Γ_a), transmission coefficient of the power combiner (α_{comb}), coupling (C_{coup}) and isolation (I_{coupl}) factors of the directional coupler.

(a)   (b)
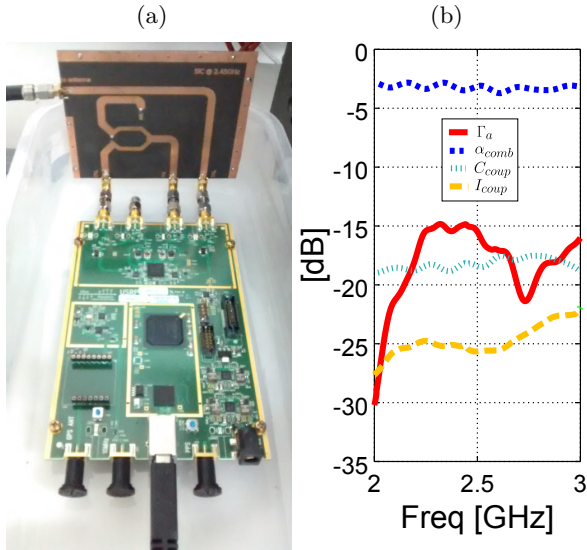
Source: The author.

The CW interrogating signal was modulated with a 32-kHz sub-carrier, and its output power was set to approximately 8.5 dBm. A PC running Ubuntu 16.04 was used for controlling the SDR board, whose sampling rate was set to 1 MS/s, and the transmitter and receiver bandwidths were set to 100 kHz. The SIC circuit was only effectively enabled when the second transmitter was turned on and set with the pre-calibrated values of amplitude and phase at each frequency. These parameters were previously obtained by a calibration routine within the frequency band of interrogation with a 1 MHz step. All measurements were carried on in a typical office environment, where the measurement with the tag was subtracted from a measured without the tag for clutter suppression.

In Fig. 6.6, the amplitude values of the baseband signals in the presence of the tag with both SIC circuit disabled and enabled (3 measurements each plus an average) are shown, without clutter subtraction. Since both measurements were done at the same receiver gain, the difference of power from both responses corresponds to the average SIC factor ($\overline{\alpha_{sic}}$), which resulted in approximately 27 dB. The spikes that can be observed in the response with the SIC circuit enabled were caused by small variations in the calibration algorithm and by possible external interference signals during measurements.

To compare the reader performance with and without SIC, instead of measuring the tag at different distances from the reader, the tag was measured at a fixed distance (20 cm) and the effect on the degradation of the SNR due to the reading distance was emulated by decreasing the receiver gain progressively.[5] For each gain setting, it was verified that the correspondent receiver noise figure was kept below a certain value in which this condition was still valid. The equivalent distance at each gain setting is given by

$$d_G = d_{(max)} \sqrt[4]{P_i^{ADC}/FSP_{ref}}, \qquad (6.17)$$

where $d_{(max)}$ is the calculated maximum distance, $FSP_{ref} = 0$ dBm is the reference full-scale power level of the ADC, and P_i^{ADC} is the input power reaching the ADC. We used $P_i^{ADC} = 0.5 G_{rx} P_i^l / C_{cp}$ since the leakage power P_i^l was assumed to be greater than the power due to the tag signal. The 0.5 factor accounts for the power combiner loss (α_{comb} in Fig. 6.4(b)), and G_{rx} is the value of the receiver gain at each gain

---

[5]As it will be shown in the next subsection, it was previewed that the reader was limited by the transmitter leakage signal.

154

setting[6].

6.3.2   Reading range calculation

The expressions developed in Section 6.1 were used to estimate the maximum reading range of the chipless reader. From the technical specifications and characterization of the SDR and SIC boards, the following values were used in the calculations: $BW = 1\,\text{MHz}$, $\alpha_{sic} = 27\,\text{dB}$, $ENOB = 12$, $SNR_{tx} = -84.5\,\text{dB}$, $SNR_o = 10\,\text{dB}$, $FOM_a = 18.2\,\text{dB}$ and $\alpha_{iso} = 6.2\,\text{dB}$. Considering a central frequency of $2.6\,\text{GHz}$ and that $T = 290\,\text{K}$, the results shown in Figs. 6.7(a) and (b) were obtained.

In Fig. 6.7(a), the sensitivity and the maximum distance are shown, assuming that the only limitation was caused by the noise (given by (6.4) and (6.10)) for $RCS = -35\,\text{dBsm}$. Two different receiver noise figure (NF_{rx}) situations were computed since this parameter varies according to the receiver gain setting. As noticed from the sensitivity plot in the left column, there are two different regions according to the transmitter power. The first occurs at low power levels and the reader performance is restricted by the noise figure (NF_{rx}). That is, the thermal noise imposes a fixed sensitivity. As expected, this result is true in a reader where no leakage noise is considered. The second region is located at higher power levels. Here, the sensitivity is limited by the SIC factor, since $N_i^{th} << N_i^l$. Consequently, it can be observed from the plot of maximum achievable distance (in the right column) how the reading range can be largely increased with the use of the SIC circuit. Moreover, it is seen that this condition is achieved at lower transmitter power levels for lower NF_{rx}. Since typically NF_{rx} is reduced at higher receiver gain values, this would be another advantage of employing a SIC circuit.

In Fig. 6.7(b), the maximum reading distances as a function of both RCS and α_{sic} are compared, this time considering both the leakage noise and the leakage signal from the expressions in (6.11) and (6.16) respectively. As noticed from the curves, the reading distance of the reader in study should be limited by the dynamic range rather than the transmitter noise due to the relatively low ENOB. Accordingly, the reader should be able to read a tag with a RCS of -35 dBsm up to a

---

[6]Receiver gain settings differs from real values. These values where characterized by the manufacturer and can be found at `https://kb.ettus.com/B200/B210/B200mini/B205mini`.

distance ($d_{(max)}$) of 0.7 m without SIC. This value is low compare to the approximately 1.4 m when considering only the leakage noise, and also significantly lower if compared to the almost 5.5 m when no leakage exists. Conversely, if SIC is enabled, the reader could reach a of 3.3 m distance taking into account the dynamic range restriction.

This last fact evidenced the importance of the SIC. Thus, the reading range calculated in (6.17) as a function of the normalized input power at the ADC is shown in Fig. 6.8. The curves show that for the same input power, the reader should achieve higher distances by enabling the SIC.

6.3.3   Experimental results

Figures 6.9(a) and 6.9(b) show the measurement results from the tag without and with SIC, respectively, for some points marked in Fig. 6.8. The measurement obtained with the VNA is also plotted as a reference guide (shown in dash lines). It can be seen that the reading performance on both cases is limited by the receiver gain, which confirms the limitation due to the reader's dynamic range.

Regarding the measurements without SIC (Fig. 6.9(a)), it is seen that the curve corresponding to the first gain setting (D1) clearly showed the resonance valley of the tag. Other valleys were also present due to the fact that only the magnitude information could be obtained at the USRP, which resulted in a non-coherent subtraction of the clutter. This issue could be tackled with a suitable calibration for the SDR platform [127]. Despite that issue, it is possible to observe the degradation on the information from the tag as the gain is reduced (D2 - D4) and the theoretical equivalent maximum distance approximates the distance used in our measurements.

Finally, as observed from the plots in Fig. 6.9(b), enabling the SIC circuit allowed for better results at similar input powers, obviating the observable spikes caused by the calibration procedure of the SIC circuit mentioned earlier. The reader was able to read the tag at an input power much lower than the minimum allowed when disabling the SIC (E3). Considering (6.16), this improvement equals to a reading-range increment of more than four times. When this power was reduced to a value equivalent to a distance shorter than 20 cm, the readability was compromised (E4), as expected.

Figure 6.5: RCS of the open-patch tag obtained with VNA and two reflectors with different dimensions (in cm × cm).
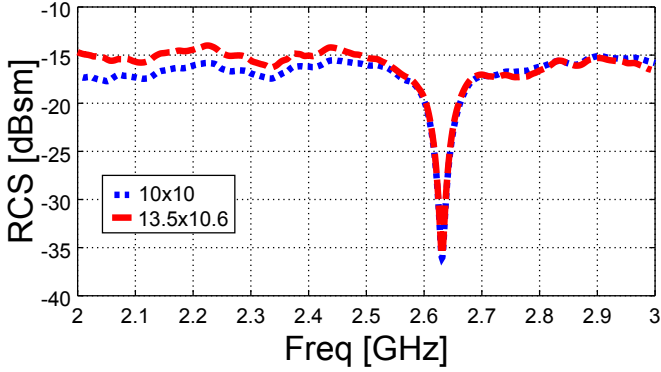
Source: The author.

Figure 6.6: Received signal power at USRP during no-tag measurement w/wo SIC for extraction of the SIC attenuation factor.
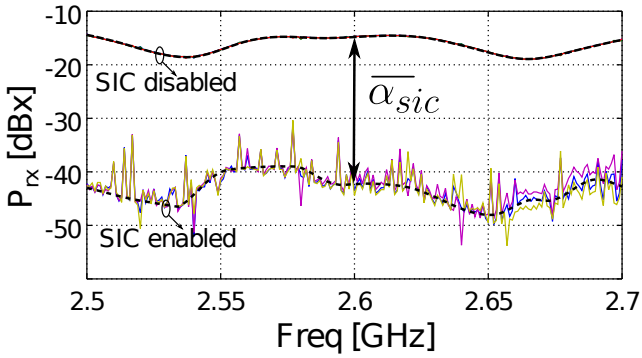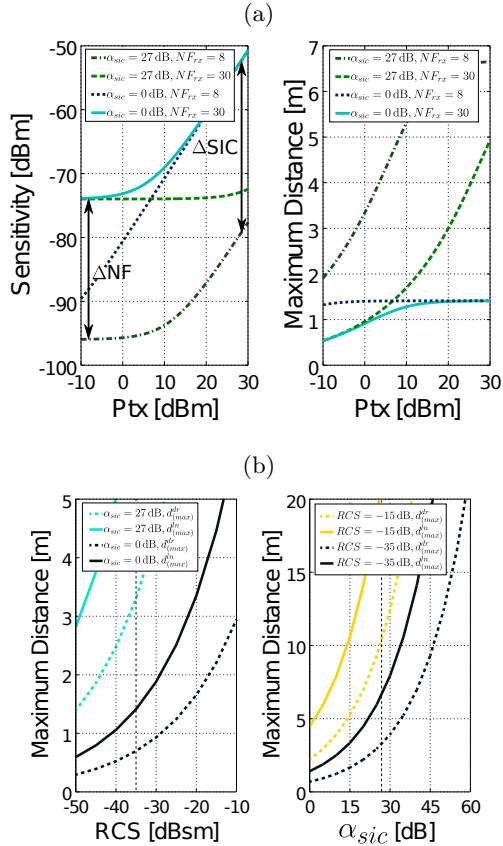
Source: The author.

Figure 6.8: Equivalent distance due to the input power at the ADC, recreated with different gain settings at the receiver for each case with and without SIC.
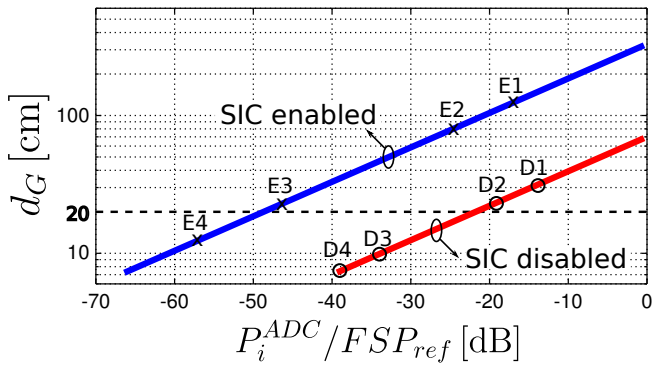
Source: The author.

Figure 6.9: Tag information retrieved from measurements with SIC (a) disabled and (b) enabled, at different receiver gains (Fig. 6.8). The RCS obtained with a VNA appears in dashed lines.
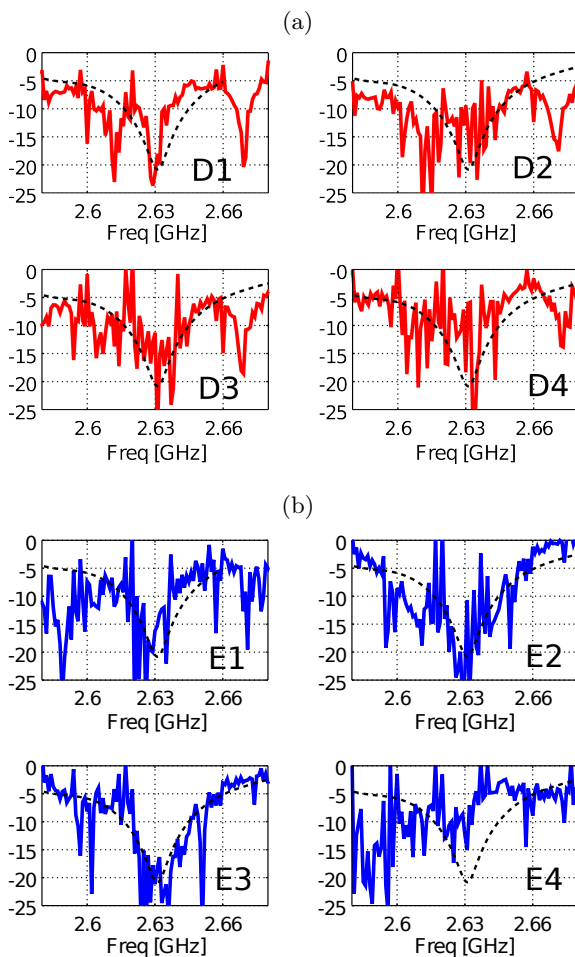
Source: The author.

6.4   CHAPTER CONCLUSIONS

In this chapter, the issue of self-interference in monostatic FSCW chipless readers was addressed. Previous reading range analysis regarding chipless sensors in literature have neglected this issue. Therefore, theoretical expressions for the reading range were provided both from the noise and large-signal perspectives considering the transmitter leakage as the critical interferer.

A chipless reader based on a SDR platform plus a dedicated SIC circuit board operating around the ISM 2.4 GHz band was implemented as a case study. From the developed expressions, the reading range of this reader was previewed to be limited due to the leakage signal power. This fact was verified from the measurement of a chipless tag by varying the receiver gain. The experimental results shown that the 27 dB attenuation factor related to the SIC technique achieved in the reader prototype showed a reading range enhancement of up to four times.

7 CONCLUSIONS AND FUTURE WORK

7.1 CONCLUSIONS AND MAIN CONTRIBUTIONS

Throughout this study, a typical chipless system comprising a chipless reader and sensor has been analyzed with the intention of identifying the main issues that degrade the process of interrogation. More specifically, the contributions of this work has been focused on the enhancing of the reading range of frequency coded miniaturized chipless sensors that are aimed to be fabricated in flexible low-cost substrates and to operate at the ISM band. In this respect, some main contributions resulted from this work.

The first contribution is the proposal of a novel configuration of miniaturized chipless sensor whose design allows for optimization for a determined specification of size and sensitivity. The structure consists in two magnetically-coupled resonating structures, the scatterer and the sensitized resonator, each of which are designed to achieve distinct goals: radiation efficiency and high sensitivity, respectively.

A second contribution is the presented theoretical analysis of the sensor performance based on its electrical model. Theoretical expressions for the main figures of merit based on this analysis were obtained. These expressions depended on the resonance frequency which, in term, was a function of the parameters of the scatterer and the sensitized resonator. Therefore, the resonance frequency obtained from the electrical model was validated through EM simulations. All these theoretical expressions are useful in the design procedure of the sensor.

The third contribution was the implementation of miniaturized sensors based on the novel configuration proposed. The main goal was to accomplish a uniplanar layout compatible with low-cost additive processes and flexible substrates. In this regard, a first round of prototypes of the proposed sensor fabricated in FR-4 substrates showed it can achieve enough sensitivities, for example, for covering the 2.4 GHz ISM band. Moreover, compared to other miniaturized proposed sensors based on capacitive transducers which were also implemented with similar substrates and fabrication processes, the proposed design can achieve higher RCS levels, which means it could be read from a larger distance.

Finally, a second round of prototypes of the sensors in flexible substrates such as paper have demonstrated that it is possible to achieve

RCS peak levels above -40 dBsm, which means those sensors could be read with a low-cost reader from more than a 1 m distance.[1] It has been verified that very few related works have been published showing a functional miniaturized frequency coded chipless sensor implemented in flexible substrates, specially printed on paper.

It is also worth mentioning that not only the sensor but the reader deserves careful attention in a chipless system. Therefore, as an unfolding of this research, a study on the reader size was also done, specifically, considering a typical architecture of FSCW chipless reader. It was concluded that if the reader requires to be low-cost and low-profile, for which a single-antenna monostatic setup is needed, it is very probable that its reading range could be limited by self-interference of its transmitter.

In this way, a theoretical analysis for the determination of the limits of the reading range considering this issue was carried on. This analysis led to two equations describing the maximum achievable distance considering two scenarios. The first one, when the reader is limited by the high-power leakage signal from the transmitter. The second one, when the leakage noise is the critical factor. The theoretical estimations were verified through experimental tests with a customized low-cost reader based on a SDR platform. It was not only proved that the leakage noise degrades the readability of a chipless tag, but that self-interference techniques applied to these readers is a necessary resource for enhancing the reading range.

7.2 FUTURE WORK

Envisaging future implementations based on the results of this study is inevitable. Many aspects of this research can be further investigated or combined to continue to contribute to the achieved results.

For instance, regarding the sensor design, a cross-polarized version of the sensor can be investigated. Cross polarization may reduce in 3 dB the reflected power from the sensor, however, it is necessary for a real scenario in which high levels of clutter are expected and dynamic readings should be performed.[2] Moreover, more measurements can be done considering the design modifications in which a higher coupling factor is achieved.

---

[1]No transmitter leakage considered.

[2]That is, calibration with a known scatterer would not be easy to make.

Another aspect that is very critical is the choice of the sensitive material. A study solely from the materials point of view is a must and should complement this study, with the objective of achieving a sensor with outstanding performance. In this regard, a complete characterization of the dielectric properties of this material within the frequency band of frequency should be done. This includes obtaining an statistical analysis on the variations of these properties for a specific fabrication process.

Complementary to the previous idea, it must be said that the proposed sensor may also be used for contactless materials characterization if a complete and robust technique is idealized for the obtention of the material properties from the measurement of sensitized resonator. This, certainly, includes a de-embedding process of all the setup measurement from the results.

Regarding the sensor modeling, a higher order model of the sensor may be useful to improve the theoretical estimations, for example, the ones related to the quality factor. This also includes considering the ohmic losses of the resonator to be a function of the measurand. Moreover, further analysis on the antenna effect on the results of the quality factor is needed.

Concerning the reader, further measurements can be carried on with the already implemented version, this time varying the reading distance from the tag and also adjusting the non-coherent reading issues. After this, the implemented reader and sensor can be both proved in a single system aiming at low-cost chipless monitoring systems. The design of a specific reader antenna for this system can also be proposed.

Finally, it would be also interesting to investigate the feasibility of the proposed chipless systems at the 920 MHz ISM band, which is the same in which UHF RFID readers operate. A customization of a commercial RFID reader can be used to demonstrate a hybrid prototype that can be used for both chipped ID tags and chipless sensors interrogation.

7.3   LIST OF PUBLICATIONS

As a result of this research, some papers were published. Below, the title of each of these publications is listed together with a summary explaining each of its contributions.

- Paper I: A Low-Cost Passive Wireless Capacitive Sensing Tag

Based on Split-Ring Resonator [152].

In: IEEE International Instrumentation and Measurement Technology Conference (I2MTC), 2015, Pisa.

Summary: In this paper, the authors proposed a wireless capacitive sensing tag that works around the 940 MHz band based on a small antenna loaded with a metamaterial in a single-layer design. The proof-of-concept was shown with two implemented prototypes, one on FR4 and the other on paper substrates. Both prototypes were adapted to work as humidity sensors. Simulations and measurements results showed the suitability of the tags for low-cost sensing applications.

- Paper II: Wireless transducer based on split-ring resonator [153].

  In: Symposium on Microelectronics Technology and Devices (SB-MICRO), 2015, Salvador.

  Summary: In this paper, the same small antenna structure presented in Paper I was proposed as part of a wireless sensing tag working on the UHF RFID band. The transducer works both as antenna for wireless communication to a RFID chip, and as sensing element.

- Paper III: Exploiting the SRR for miniaturization and sensitivity of a humidity chipless sensor [154].

  In: MOMAG, 2016, Porto Alegre.

  Summary: This paper presented preliminary results of the chipless sensor proposed in this thesis. A single-layer structure based on an open-ring resonator coupled to a split-ring resonator working as a humidity wireless sensor at 2.4 GHz ISM band. An analysis of the resonance frequency based on the electrical model is presented. Measurement results proved that the proposed structure achieved a high level of miniaturization and good sensitivity compared to a chipless sensor based only on an open-ring resonator.

- Paper IV: Miniaturized chipless sensor with magnetically-coupled transducer for improved RCS [155].

  In: IEEE Microwave and Component Letters, 2017.

  Summary: In this paper, the main the results presented in Chapter 4, that is, full-wave simulation results and sensitivity measurements of the proposed sensor, wee presented. It was shown that

the structure was able to addressing miniaturization and sensitivity in uniplanar designs, permitting maximizing the RCS for a determined available area and required sensitivity.

- Paper V: Self-interference cancellation in chipless RFID readers for reading range enhancement [156].

  In: IEEE International Instrumentation and Measurement Technology Conference (I2MTC), 2018, Texas.

  Summary: In this work, the study of the effect of self-interference cancellation in single-antenna monostatic chipless RFID readers on its reading range was presented. This included two theoretical limits for this range were obtained by taking into account both the signal and noise leaked from the transmitter. Moreover, a software-defined radio-based reader implemented was shown. Its performance was predicted to be restricted by the leakage signal power rather than the noise power, fact that was verified through measurements of a chipless tag. The experimental results also showed an improvement of more than four-times in the reading range through a 27-dB attenuation of the self-interference signal.

Appendices

A DERIVATION OF FORMULAS

A.1 RADIATION RESISTANCE OF AN ORR

Figure A.1: Open ring resonator with (a) $\varphi_s = 0$ (b) and $\varphi_s \neq 0$.

(a)   (b)
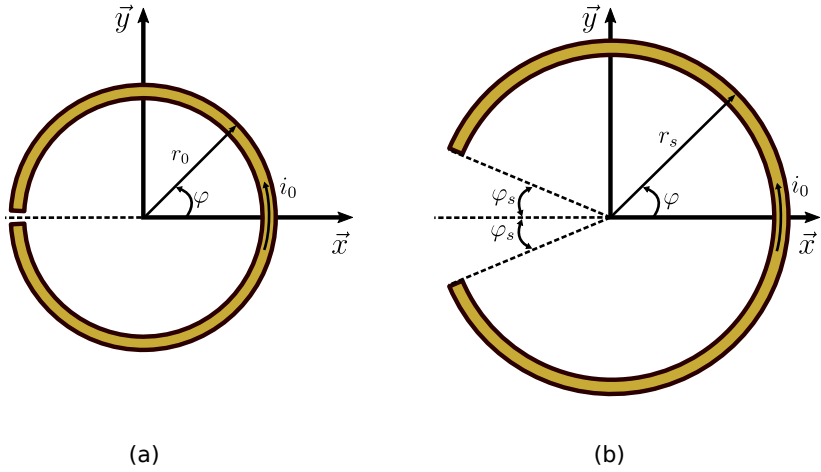
Source: The author.

First, Let us consider the circular ORR with a very small slit ($\varphi_s \approx 0$) in Fig. A.1(a). Assuming that the slit capacitance is negligible, the ring resonance frequency can be expressed as

$$\omega_0 = v_p/\lambda_0, \tag{A.1}$$

where v_p is the phase velocity and λ_0 is the equivalent wavelength at resonance, whose approximated value, in this case, is given by

$$\lambda_0 \approx 4\pi r_0. \tag{A.2}$$

Following a similar procedure than the one described by Zuffanelli et al. [88, 91], the desired objective is to estimate the radiation resistance of the ORR with a non-zero slit defined by the aperture angle φ_s, as illustrated in Fig. A.1(b).

For a given combination of r_s and φ_s, a resonance angular frequency ω_s for the ORR in Fig A.1(b) can be defined as

$$\omega_s = v_p/\lambda_s, \tag{A.3}$$

where λ_s is the equivalent wavelength at resonance, which occurs approximately at

$$\lambda_s \approx 4\pi r_s/(2k_s). \tag{A.4}$$

Here, k_s is a correction factor which accounts for the slit angle:

$$k_s = \frac{\pi}{2(\pi - \varphi_s)}. \tag{A.5}$$

Due to the standing wave condition at resonance, the current distribution is assumed to be sinusoidal along the ring. Thus, for $\varphi \in [-\pi + \varphi_s, \pi - \varphi_s]$, this current can be written as

$$i(\varphi, t) = i_0 \cos{(\varphi k_s)} \cos{(\omega_s t)} \tag{A.6}$$

where i_0 is the current amplitude.

From the continuity equation, the linear charge density can be derived from the integral of the gradient of the current density:

$$\lambda(\varphi, t) = \frac{i_0}{r_s \omega_s} k_s \sin{(\varphi k_s)} \sin{(\omega_s t)}. \tag{A.7}$$

Since the charge distribution is symmetric along the x axis, there is a pair of infinitesimal charges (dq) of opposite polarities at a specific φ value ($[0, \pi - \varphi_s]$). This is equivalent to have an infinitesimal dipole moment given by:

$$d\vec{p} = (\lambda(\varphi, t)r_s)(2r_s \sin \varphi)\ \hat{y}, \tag{A.8}$$

where the first term in parentheses corresponds to dq and the second one corresponds to the distance between the opposite pair of charges.

To calculate the total electrical dipole moment of the ring ($\vec{p}$) in the $\hat{y}$ direction, all the individual dipole moments are integrated along the x axis, thus, by integrating φ from 0 to $\pi - \varphi_s$, one can obtain

$$\vec{p} = \frac{i_0 r_s k_s}{\omega_s} \left(\frac{2\cos(\pi - \varphi_s)}{k_s^2 - 1} \right) \sin{(\omega_s t)}\ \hat{y}. \tag{A.9}$$

This result is compatible to the one found in [91] for $\varphi_s = 0$.

From the Larmor equation, the radiated power by an electric dipole moment of amplitude $|\vec{p}| = p_0$ can be expressed as

$$P_r = c_0^2 \frac{Z_0 k^4 p_0^2}{12\pi}, \tag{A.10}$$

where c_0 is the speed of light, Z_0 is the wave impedance, and $k = 2\pi/\lambda_s$ is the wavenumber. Therefore, one can find the total radiation resistance by substituting the total electrical dipole moment of the ORR in (A.10) from the result obtained in (A.9), and then dividing this expression by the current amplitude squared. This procedure results in

$$R_r = \frac{4Z_0\pi}{3} \left(\frac{r_s}{\lambda_s} \right)^2 \alpha_s^2, \tag{A.11}$$

where $\alpha_s = k_s \frac{\cos(\pi - \varphi_s)}{k_s^2 - 1}$.

Finally, it can be noticed that this last result can be further simplified if the resonance frequency value of the ORR is assumed to happen at the condition given by (A.4). As a result, $r_s/\lambda_s = k_s/2\pi$, and one can obtain from (A.11):

$$R_r = 40k_s^2\alpha_s^2. \tag{A.12}$$

It is observed that the radiation resistance should be a function of φ_s. In other words, it is demonstrated that, independently of the resonance frequency value, the radiation resistance is only dependent on the slit aperture.

A.2 PARAMETER EXTRACTION FOR THE CIRCUIT MODEL

For the estimation of the shifted frequency caused by the coupling of the sensitized resonator with the scatterer, it is necessary to extract not only the parameters of each of the resonators, but also the coupling factor. Therefore, a similar procedure for characterizing miniaturized resonators described in [128] was followed, however, with the scatterer instead of the closed loop as the exciter resonator. All the parameters are calculated as described in that work but one change must be considered for the specific case of the proposed sensor.

Since the self-resonance frequencies of both the resonator and scatterer are close, the latter equivalent series capacitance can not be neglected. Therefore, the step in [128] in which the inductance of the scatterer is estimated, should be modified to:

$$L_s = \frac{\Im(Z_A(\omega_r))}{\omega_r - \frac{\omega_s^2}{\omega_r}} \tag{A.13}$$

B   CARES IN MEASUREMENT PROCEDURES OF CHIP-LESS TAGS

B.1   GENERAL CONSIDERATIONS

Measurement of chipless tags and sensors requires patience, specially if not special shielded rooms such as anechoic chambers are available for the tests. All tests used the VNA available at the laboratory for the chipless tag interrogation. Also, all measurements presented in this work were carried on common laboratory rooms, which included personal computers, other test equipments, nearby classrooms and, sometimes, people. For the best results, specially with low RCS tags and larger reading distances, the best scenario was to use these environments with no people in a 5 m perimeter.

All measurements were always averaged, so eventual external random sources of signals at the same band were attenuated. Moreover, time-averaging was always used in the VNA as to enhance SNR of the reading. Most of the reading were also commanded at distance, that is, from a remote computer that was connected through local network to the VNA.

Particular care was further required when sensitivity related measurements were performed. For example, when dynamic measurements were required (gel to water transition), a very extended time the sensor should remain at the same position. A a slight change in the setup configuration (undesired cable movement, people walking nearby, environment conditions) may lead to misinterpreted results and to the inevitable repetition of the measurement.

B.2   READER ANTENNA AND REFLECTOR SIZE

Tests regarding distance range, reader antenna types and reflector sizes (for RCS reference) were executed. First, a test of reading distance was done with two different antennas. The objective was to verify the maximum achievable distance with the measurement setup available at the Laboratory. For this purpose, a 10 cm x 10 cm metallic plate was employed and two antennas were used (shown in Fig. B.1): a quasi-Yagi antenna and a LPDA antenna.

Figure B.1: Implemented antennas for chipless measurements.

(a) quasi-Yagi   (b) LPDA
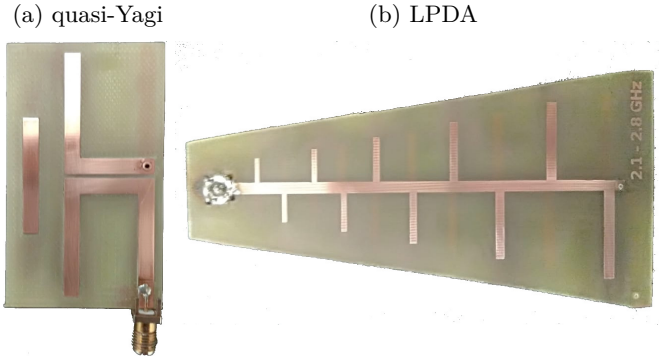
Source: The author.

The results regarding each of the mentioned antennas are shown in Fig. B.2 and B.3. These results showed that larger distance ranges could be achieved with the LPDA antenna. This was expected since its simulated directivity was above 6 dBi, in contrast to approximately 3 dBi of the quasi-Yagi counterpart.

Figure B.2: Measured (a) |S11| (minus clutter) and (b) RCS of loaded ORR with copper tape trace and PET substrate using the quasi-yagi antenna at different distances with 10 cm × 10 cm metallic plate.

(a) |S11| (b) RCS
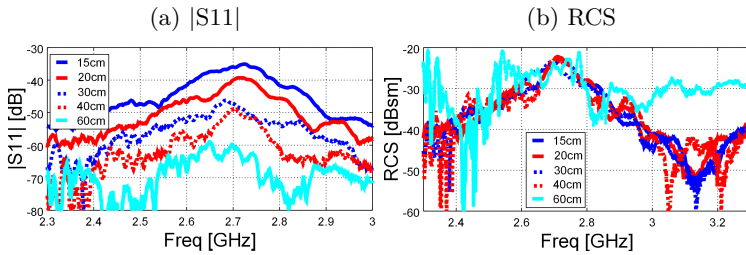
Source: The author.

It is also observed that, when a successful measurement is achieved, the tag information is distinguishable directly from the reflection coefficient (S11) information. Also, as noticed from the results in B.3(b) at 65 cm, slight measurement inaccuracies can turn the RCS results useless. That is, the result of the measurement showed a good result in S11, but an indistinguishable peak at the RCS. This issue might have been

Figure B.3: Measured (a) |S11| (minus clutter) and (b) RCS of loaded ORR with copper tape trace and Epson paper substrate using the LPDA antenna at different distances with $10\,\text{cm} \times 10\,\text{cm}$ metallic plate.
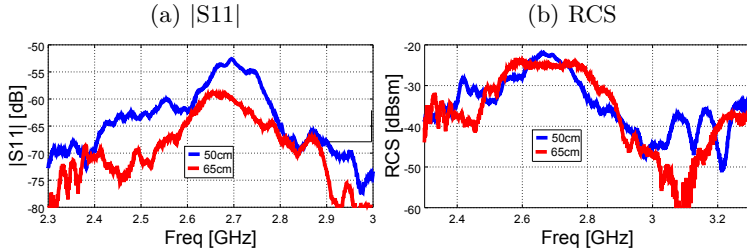
Source: The author.

caused by an artifact during the reflector measurement. This is proved by comparing the same measurement with other reflectors as seen next.

Figure B.4 compares the RCS of the tag at $65\,\text{cm}$ using reflectors of different sizes as references. Each of the plate sizes are listed in Table. B.1. Two things can be verified: first, the peak information at such distance remains very prone to error, due to measurement errors and the relative small reflected power from the tag compared to the clutter and metallic plates; second, the absolute value of the RCS of the tag is not the same for each measurement.

Table B.1: Metallic plates dimensions used as RCS references for chipless measurements.

plate ID	dimensions [cm × cm]
1	10×10
2	51.8×34.2
3	55.8×46
4	112.4×65.2

For the results calculation shown in Fig. B.4, the theoretical RCS of the metallic plates was used as the reference ($RCS_{plate} = 4\pi A^2/\lambda^2$, where A is the plate area). To make sure this is a good approximation, the RCS obtained from FDTD simulations were compared for two plates with different areas, as shown in Fig. B.5. The bigger plate presented simulated RCS results very close to the theoretical predictions. The smallest plate showed a very close result to the theoretical calculations within the frequency band of interest. Therefore, these results proved

Figure B.4: Measured RCS of loaded ORR with copper tape trace and Epson paper substrate using the LPDA antenna at a 65 cm distance with different metallic plates.
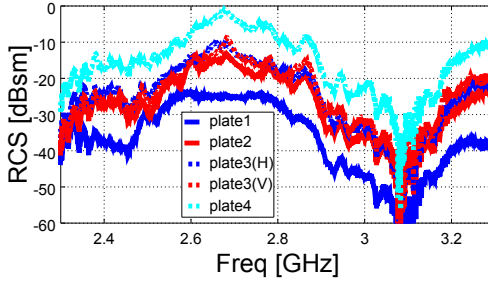
Source: The author.

that all RCS of the used plates can be approximated to its theoretical formulas.

Figure B.5: RCS of metallic plates, simulated vs theoretical.

(a) plate 1   (b) plate 2
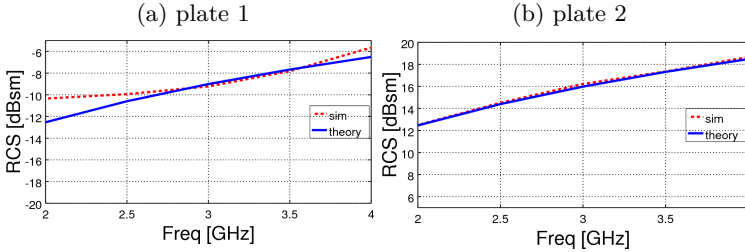
Source: The author.

To find a possible explanation to the results shown in Fig. B.4, another set of measurements were performed. Fig. B.6 shows the measured reflection coefficient (with clutter subtracted) from two plates measured at different distances with two different antennas. It can be observed that in the case of the smaller plate (plate 1), the magnitude of the reflection coefficient changes gradually with distance. On the other hand, the change of the reflected power in the case of the bigger plate is not as expressive as in the first case, for both antennas. This means that the reader does was not able to perceive a difference on the received power.

A possible explanation to this effect is related to the radiation pattern and the beam-width of the maximum lobe of the reader antenna.

It might be the case that when the reflector is considerably big, enough so its main lobe is almost totally reflected, the antenna is not capable of perceive any change on the reflected power, causing a misreading of the RCS. This phenomena is represented in Fig. B.7.

Figure B.6: Measured S11 magnitude of metallic plates vs distance, of (a) plate 1 vs plate 5 with quasi-Yagi antenna, (b) plate 1 vs plate 2 with LPDA antenna.
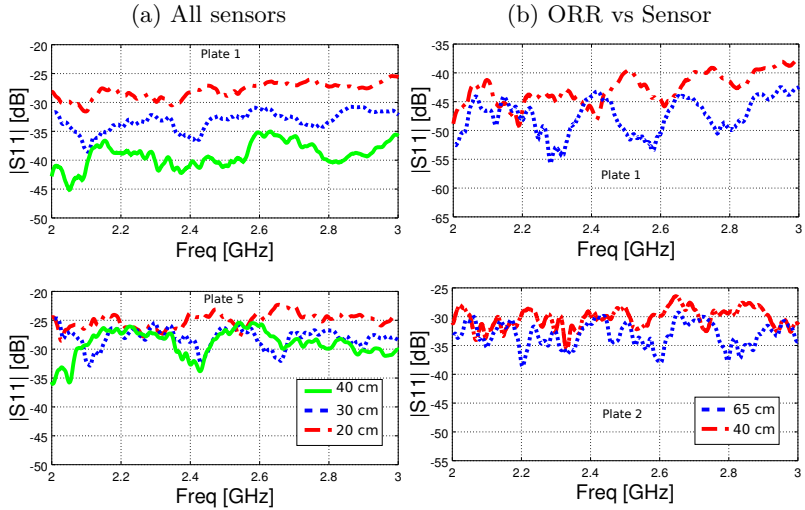
Source: The author.

As a conclusion, it can be stated that for small reading distances, big metallic plates may lead to erroneous RCS estimation of the tag. In contrast, an small plate (such as plate 1) would be accurate enough for the reading distances used in this work. Moreover, its measured RCS is not expected to be much different than the estimated by theory. For a more exact determination of the appropriate reading distance for a metallic reflector, the beamwidth of the reader antenna should be always considered.

Figure B.7: Beamwidth effect on miscalculation of metallic reflector RCS as a function of distance.
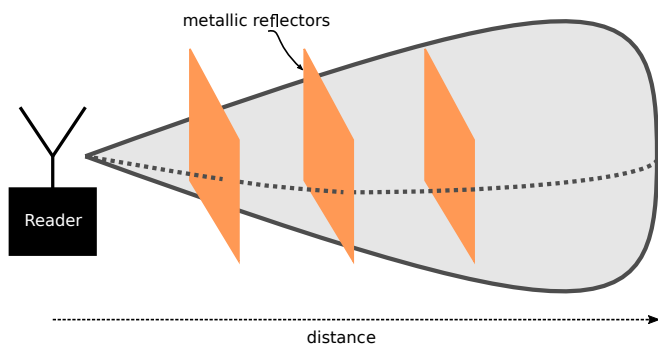
Source: The author.

C CHARACTERIZATION OF MATERIALS USED IN LOW-COST CHIPLESS SENSORS

C.1 CONDUCTIVE INKS FOR INKJET PRINTED CIRCUITS

Inkjet printers allow to use different solution-based materials, such as organic semiconductors, dielectrics and conductive inks. These inks must fulfill a list of requirements in order to be successfully printed from the inkjet nozzles heads. The Electrical Materials Laboratory (LA-MATE) at UFSC is equipped with a material deposition printer model DIMATIX 2831, which is the lowest-cost solution of inkjet printers from Fujifilm®, intended for prototyping purposes and research. This drop-on-demand (DOD) printer uses piezoelectric membranes which are excited by controlled voltage sources for drop formation. The fluid requirements and value ranges of the ink specified by vendor are summarized in Table C.1 [129]. Particle size should be at least 100 times less than cartridge nozzle diameter, and when this is not 100% guaranteed by ink provider, filters should be used when filling the cartridge.

Table C.1: Fluid requirements for inks used with Dimatix 2831 inkjet printer

Specification	Min	Max
Particle size [nm]		200^1
Viscosity [cP]	10^2	12
Surface tension [dynes/cm]	28	42
pH	4	9
Boiling point [° C]	100	-

Besides the fluid characteristics, the printing parameters set during printing process impact directly on the final quality of the printed patterns. These parameters include nozzle waveform for drop formation, cartridge temperature, substrate temperature, printing resolution or equivalently drop spacing (DS), jetting speed, time between printed layers, number of printing nozzles, alternative printing strategies, among others. These parameters does not only depend on the ink type but also

on the specific substrate used, since the interaction between ink and substrates varies. Moreover, post-printing processes required to cure inks, such as thermal sintering, have a tremendous effect on the conductivity on the final patterns. Therefore, evaluating all these procedures in a systematic way in order to be reproducible are necessary for guarantying good performance of the printed circuits.

Commercial nanoparticle silver-inks are commonly used for inkjet printing of conductive traces in printed electronics. These inks consists mainly of three components: The solvent, the nanoparticles of metal, and a plaster made of a polymer which covers the nanoparticles. The melting temperature of the nanoparticles are related to its size, i.e., lower particles are expected to be sintered at lower temperatures and at faster rates. Previous works reported in technical literature were reviewed in order to confirm the most adequate curing procedure (sintering and annealing) of the conductive ink. Among all different methods for curing, this work emphasizes on thermal curing [130]. At room temperature, when the ink is completely dry, there is not effective contact between nanoparticles, since the plaster covering them is not melted. Partial melting is achieved at middle range temperatures, and the trace starts showing conductive properties. However, a complete annealing only occurs at higher temperatures.

From the reviewed literature, it can be concluded that there is no unique recipe for curing inks. Specific parameters such as optimal temperature, time, and multiple thermal cycles have been employed. Specific limitations arises when working with polymer-based low-cost substrates. From one side, temperature must satisfy the solvent evaporation and plaster melting, while from the other side, temperature must not cause substrate degradation. This degradation can be physically evident, such as burning, or can cause substrate shrinkage, which may cause micro-cracking and lead to high losses of conductivity [131].

In the case of the acquired silver ink for our experiments, Polyvinyl-pyrrolidone (PVP) is the polymer used for the plaster that covers the nanoparticles of the ink [132, 133], and its melting temperature is expected to be above $150°$ C. This temperature threshold was also verified by Scanning Electron Microscope (SEM) images of sintered printed structures reported in [131]. At temperatures between 100 and $150°$ C, conductance resulted by solvent evaporation and slight melting of polymer coverage. Just at temperatures above $150°$ C the nanoparticles grains began to unify and formed bigger ones. According to the ink vendor website [134], the curing temperature of the ink is between 120 to $150°$ C. The reviewed studies which have reported

working with the same nanoparticle ink are summarized in Table C.2, including printing and post-printing settings and their electrical performance results. It is shown that the reported works in [131, 135, 136] have been capable to cure this ink at relative low temperatures ($<120° C$), $allowing printing structures on paper. In the case of [131], they claimed to ha$ with 1 hour sintering in a convection oven at $120°$ C after a pre-drying 2-hour period ad ambient temperature. This resistivity is equivalent to a conductivity of 9.4e6 S/cm, which is almost seven times less than the conductivity of bulk silver. Also, in [135], they have achieved a sheet resistance of $0.06\,\Omega$/sqr with 1 hour sintering in a convection oven at $120°$ C.

After the ink is sintered, the conductivity can be obtained from the sheet resistance measurement. Sheet resistance is directly obtained by resistance (voltage over current) measurement of the sample. When the expected resistance value to be measured is low, such in well-sintered silver inks, the cables and probe contact resistances may influence the measurement. In that case, a four-point probe is frequently used [141]. By measuring with this technique, the sheet resistance of any geometrical structures is obtained, as long as a correspondent correction factor is applied, which depends on the type of probes arrangement, thickness of the sample with respect to probes separation, finite dimensions, and limit/border corrections. When using arbitrary-shape structures that present a plane of symmetry, the well-known Van-der Pauw theorem can be applied [144].

The printed structure should result in solid homogeneous almost-2D sample (very small thickness). Also the probes contact must be an order of magnitude less than the area of the sample, and much smaller than the distance between probes. Moreover, all probes and wires should be made from the same materials, in order to minimize thermoelectric effects. The sheet resistance is calculated by applying a current through the two outer probes and measuring the voltage at the two inner probes. In our case, the structures for characterizing our inkjet printing process were squares (see Fig. C.6). The four probes were positioned in line at the middle of the square. Two perpendicular measurements were done, vertically and horizontally, and with different polarities, so an average resistance measurement was obtained. Then, the sheet resistance (R_{SH}) is calculated from [144]:

$$R_{SH} = \frac{2\pi R_{av}}{\ln 2}, \tag{C.1}$$

where R_{av} represents the average measured resistance. The resistivity

of the material can then be obtained from :

$$\rho = R_{SH}t, \tag{C.2}$$

where t is the thickness of the conductive trace of the sample. Finally, the conductivity can be also obtained:

$$\sigma = 1/\rho. \tag{C.3}$$

Alternatively to the in-line probes, the probes can also be disposed in a square configuration [141], and the Greek-cross structure [142] can be used instead of the squares, using less ink for R_{SH} characterization. For higher expected resistance measurements, a two-point probe would be enough, and resistivity can be calculated directly from resistance measurement divided by cross-section area of the sample and multiplied by its length. This can be a quick verification procedure for comparing different printing settings.

At this point it is worth remarking that resistivity and conductivity are intrinsic material properties, while sheet resistance is a device parameter and not a material parameter because it depends on the thickness of the sample. However, since the printing patterns density are dependent on sintering process, and not complete annealing of nanoparticles are expected at low temperatures, final conductivity will indeed depend on printing and post-printing settings. The more the sintering process joins the nanoparticles forming an homogeneous dense structure, the more the conductivity will approach the Silver bulk conductivity ($\approx 6.3\,e7\,\text{S/m}$ at $20°$ C).

In this section, the procedure for printing and characterizing a silver-nanoparticle conductive ink, more specifically, ANP-40L-15C from Advanced Nano Products [134], is described. Specific tests were done based on literature review of previous works which have worked with similar inks and substrates, as well as ink providers specifications. As a result, electrical parameters, such as sheet resistance and effective conductivity are extracted from the followed process, and will then be used within simulation environments for the sensors design.

C.1.0.1   Experimental results

The first step for characterizing the ink interaction with substrate is to measure the size of one printed drop on the substrate. Each ink and its interaction with different substrates determine the drop size,

and consequently, the printing resolution. A squared pattern of 10 x 10 pixels, with enough large DS (100 - 200 μm), is commonly used for observing the drops individually. The camera included with the inkjet printer (known as fiducial camera) is used for measuring the drop size, with an approximated error of $\pm\,2\,\mu$m.

The drop size will also depend on the substrate temperature. Higher temperatures are usually related with smaller drops when substrates have a low-surface tension, like some plastics, or do not have any chemical coating to trap the ink, as photo-quality paper. Therefore, it is interesting to observe temperature effect on this step. Figure C.1 shows the drop sizes of the silver ink on different photo-quality papers printed from a 10 pl cartridge. The average drop sizes are listed in Table C.3. The drop diameter sizes vary from 40 to 60 μm depending on the paper used. Note that in the paper fabricated by Filipaper the ink was not naturally adhered, revealing that there is a mismatch between surface tensions which causes the ink to disperse randomly. Smaller and darker drops were obtained with papers from Epson, which reveals a higher substrate surface tension and not easy solvent absorption. The biggest drops were obtained with Datajet and Techno papers, while a middle size was obtained with Multilaser paper. In these cases, the solvent was quickly absorbed by the paper. Another test was done for comparing the drop size at different substrate temperatures. As seen from Fig. C.2 and C.3, no significant change was observed in drop size, probably due to the coating over the paper substrate which captures the ink solid materials and absorb the solvent letting it drown to the bottom part. Temperature, though, can be efficiently used when more printed layers are required and for faster printing procedures.

The substrates selected for realizing the electrical parameters were the high glossy inkjet paper 180 g/m^2 A4-size from Multilaser and the glossy photo paper A6-size from Epson, which did show good printability without any previous surface treatment. The Multilaser paper was easily acquired from a local bookstore at a unitary cost of R$ 0.60. It is single face and water resistant, and stands up to 145° C. It presented an average diameter drop size of approximately 52 μm. The Epson paper is a more expensive paper (R$ 0.78) due to its enhanced photo quality, and was purchased at an online bookstore. It is fully water-resistant, has a bearable exposing temperature of up to 135° C and the average diameter drop size is 40 μm. The exposing temperatures of each paper were determined from tests with the papers over glass

---

[3]Samples of this paper came with the printer when acquired. No further technical details where given.

Figure C.1: Drop size in different paper substrates: a) Datajet, b) Techno, c) Filipaper, d) Epson, e) Epson (A6), f) Multilaser.
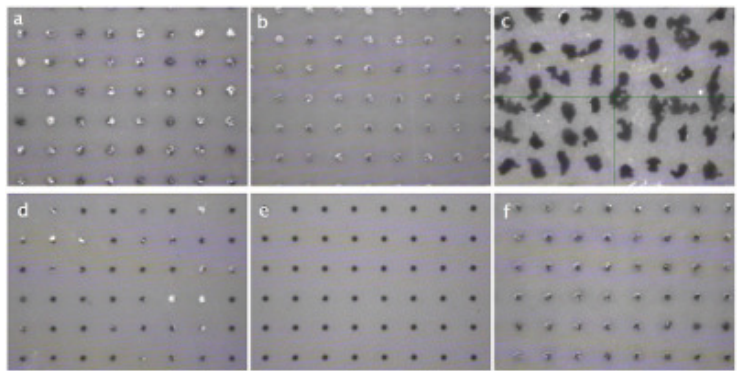
Source: The author.

Figure C.2: Drop size in Multilaser paper calculated from fiducial camera at different substrate temperatures (35, 50 and 60° C).
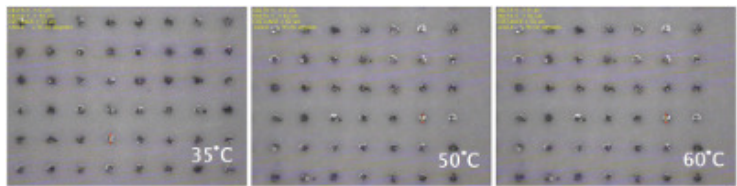
Source: The author.

Figure C.3: Drop size in Epson A6-size paper calculated from fiducial camera at different substrate temperatures (35, 50 and 60° C).
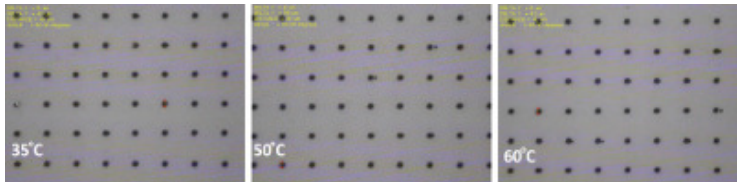
Source: The author.

and metal plates inside a convection oven acquired from QuincyLab. These tests were done with small-size pieces of paper and comparing the results with and without adhesive tapes that fixed them to the plates. Best results were achieved without any fixing or metal plates.

For printing continuous homogeneous patterns, usually, half of the diameter drop size value is a good start-point reference for testing. Figure C.4 shows horizontal and vertical lines printed on Multilaser paper with DS of 26 μm and a substrate temperature of 35° C. These line patterns were made with a single nozzle. Stable and well defined patterns can be observed for one, three and five lines. The so-called *coffee ring effect* is somehow noticed at the beginning of the horizontal lines [143]. Figure C.5 shows the same printed patterns on Epson paper, this time with a DS of 18 μm, since the drop size at this paper was smaller. Two different tests with one and six simultaneous nozzles were done. The verification of printing performance with multiple nozzles becomes crucial if faster fabrication is desirable, specially for large-area patterns [4]. The results presented in Fig. C.5 show that homogeneous patterns are also achieved. A little bulging exists on some of the horizontal lines when using of 6 nozzles. This bulging appears since the drops simultaneously falls over the substrate, and their interaction could be slightly stronger than the interaction with the substrate [143]. This, in fact, was already observed from the drop size tests where it was verified that the diameter in Epson paper where smaller due to the fact of presenting less absorption and evaporation rate of the solvent. From these line test it can also be expected than less layers might be used in Epson paper in comparison to Multilaser for achieving the same thickness.

Figure C.4: Horizontal and vertical lines printed on Multilaser paper, respectively, printed with drop spacing of 26 μm (1, 3 and 5 lines respectively). The cartridge temperature was of 37° C and substrate was set at 35° C.
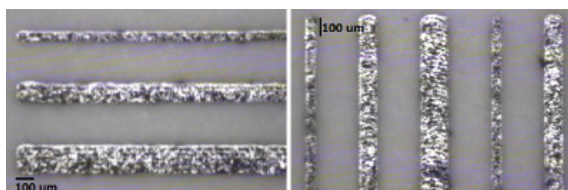
Source: The author.

First sintering tests and conductivity measurements were carried on Multilaser paper substrates. Squared structures (see Fig. C.6) were printed for measuring conductivity with the 4-probe method. Two different DS values were used, 26 μm and 22 μm, and also different number of layers (1, 3, and 5). The squares were sintered in an convection

---

[4]Dimatix 2831 inkjet printer has a maximum of 16 nozzles.

oven at 130° C average ($\pm$ 2° C), and varying the sintering time from one to two hours [5]Total time of sintering was considered when oven was turn-off, but it was left closed. Internal temperature decayed in 2 ° C/min average rate (from 130 to 110° C in 10 min, to 80C in 20 min, to 60° C in 30 min, 55° C 40 min).. Photographs taken with the fiducial camera of the pre-sintered and sintered squares are shown in Fig. C.7. Evident differences can be seen in the structures after sintering. It can be also observed that a two-hour sintering step (at 130° C) caused visible micro-cracks on printed squares, both at DS of 26 and 22 μm.

Further analysis of the printed squares were done by measuring its thickness (and roughness) at the Detak profilometer. The curve results are illustrated in Fig. C.8. These curves show the transition of paper and the border of the squares, and the profilometer sweep was made opposite to the direction of the printed lines of the printer, since here we can observe better the junctures of printed lines. Spacial resolution of 0.1 μm/px was set by selecting sweep time at the profilometer. All curves were processed by software with a two-point linear fit in order to eliminated the bends or little curvatures on paper, which was easier to realized for three and five-layer squares.

The curve extracted from one printed layer revealed that the existence of many valleys- which was not visibly noticeable from previous inspection with fiducial camera from the inkjet printer. This may suggest

Figure C.5: Horizontal and vertical lines printed on Epson A6-size paper, respectively, printed with drop spacing of 18 μm (1, 3 and 5 lines respectively). The cartridge temperature was of 35° C and substrate was set at 35° C.
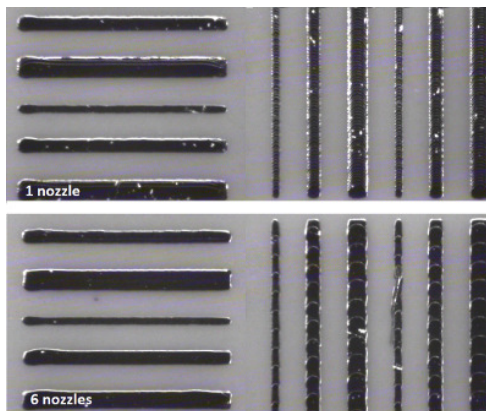
Source: The author.

Figure C.6: Printed squares with different number of layers and drop spacing to verify conductivity by 4-probe measurement.
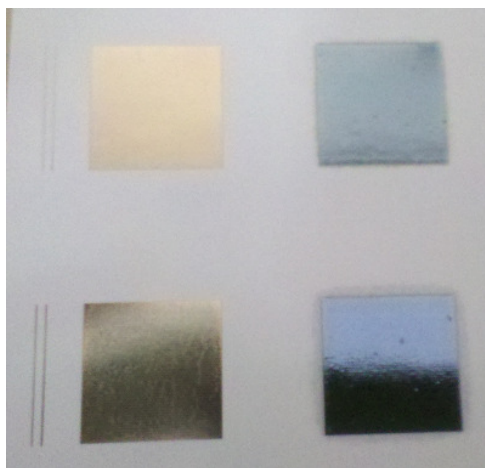
Source: The author.

the presence of micro-cracks. Some valleys are also observable in the three and one-layer squares. Although not visible at the naked eye or with the fiducial camera, the one-hour sintered structures presented signals of microcracks as well. Therefore, a closer inspection of Multilaser paper was done in an optical microscope with up to 1000x magnification. The observations revealed that cracks were present at the paper itself, before printing and even before sintering.

In Figure C.9, printed squares as well as line patterns in Multilaser paper are shown. The micro-cracks are present in all printed structures, following the paper surface defects. Even a seven-layer printed structure could not fill in the spaces continuously in some cases, causing an electrical discontinuity.

The final obtained values of DC conductivity and sheet resistances from 4-probe conductivity measurement of the printed squares are presented in the same figure. An average of $400\,\mu$m thickness for each printed layer was considered for the calculations, even though the presence of big valleys extracted from profilometer curves. For DS of $26\,\mu$m and 1 hr sintering, the results were the highest achieved. Nonetheless, the results are still lower than other reported for the same ink and other silver inks at similar sintering time and temperature. These poor performance are related to the presence of the micro-cracks. The results

Figure C.7: Photographs taken with the inkjet printer fiducial camera of printed squares a) with DS $= 26\,\mu$m not sintered, b) with DS $= 26\,\mu$m 1hr sintering at $130°$ C, c) with DS $= 26\,\mu$m 2hr sintering at $130°$ C, d) with DS $= 22\,\mu$m 2hr sintering at $130°$ C. Sintered structures in c) and d) clearly shows micro-cracking.
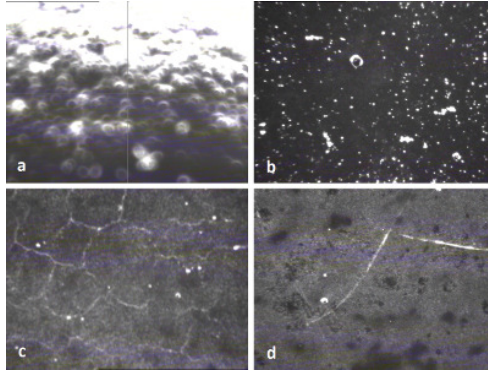
Source: The author.

for two-hour sintering were worse, which reveals that the cracks effect is higher at larger sintering times. From these tests, it can be concluded that Multilaser paper is not suitable for inkjet printing due to the poor conductivity achieved and lack of performance control, even for several printed layers.

Another set of printability tests were carried with Epson paper. First, the a single-layer line pattern for intended for two-probe conductivity measurement was observed with the optical microscope with 20x, 50x, 200x, and 1000x magnification, as shown in figure C.10. There is an obvious difference from these results compared to the one obtained with Multilaser paper, since no cracks are present and an homogeneous surface is achieved even after sintering.

The thickness of these printed lines were also obtained by profilometer measurement. The spacial resolution of the profilometer tip was set to $0.18\,\mu$m/px, 100 times less than the DS. The results for one and two layers are shown in Fig. C.11. No pronounced valleys were detected, confirming the absence of cracks. An average thickness of $1.2\,\mu$m per layer was measured.

The conductivity for the printed lines on Epson A6-size paper was obtained from 2-probe measurements with a digital multimeter. These results of sheet resistance and calculated conductance are summarized in Table. C.4.

Figure C.8: Profile curves obtained with Detak profilometer, for printed squares with 1, 3 and 5 layers on Multilaser paper.
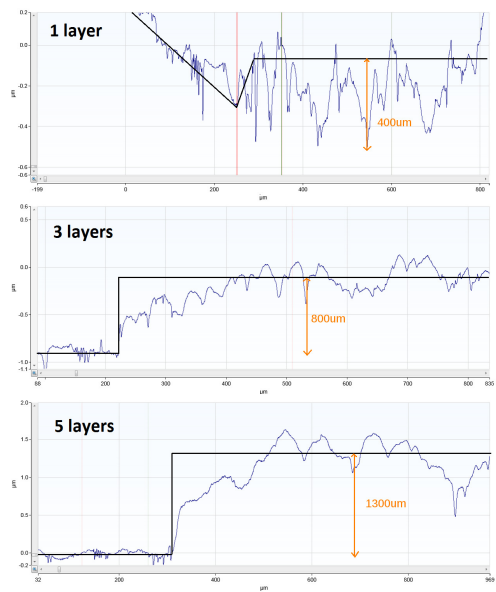
Source: The author.

Figure C.9: Images of printing structures on Multilaser paper taken from optical microscope showing evidence of microcracks. Below, the conductivity results for this paper obtained from 4-probe measurements.

Temperature (C)	Not sintered				130				
Sintering time (hr)	-		1				2		
Drop spacing (um)	26		26		26		22		
Number of Layers	1	1	3	5	1	5	1	5	
Conductivity (S/m)	4.37E+02	1.98E+04	1.42E+05	1.07E+06	1.63E+05	3.20E+03	2.09E+04	1.23E+05	
Thickness (um)	0.4	0.4	0.8	1.3	0.4	1.3	0.4	1.3	
Sheet Resistance (Ohms / square)	5,775.75	127.32	8.85	0.72	16.69	281.24	159.81	34.26	
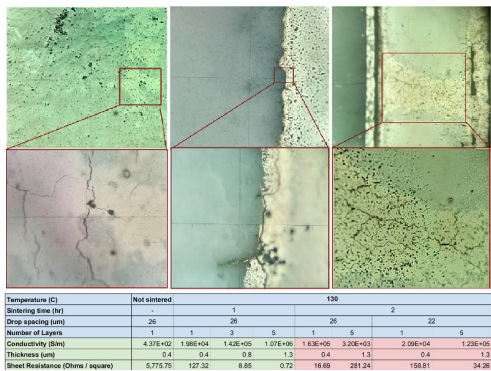
Source: The author.

Table C.2: Reported works using DGP-40L-15C silver jet ink on different substrates

Reference	Substrate	T_{subs} [°C]	DS [μm]	# of layers	Curing eqp.	T_{sint} [°C]	Time [hr]	Electrical performance
[131]	Photo and Laser papers	28	20	1	air / Oven	ambient/ 110	2/ 1	ρ = 10.7 μΩ−cm
[135]	Photo paper	n.r.	n.r.	2	Oven	120	1	R_{sh} = 0.063 Ω/sqr
[137]	p-type Silicon	-	-	3-5	Oven/ furnace	100/ 250	1/ 0.5	n.r.
[138]	LCP	60	20	3	Oven	60/ 150	3/ 0.5	σ = 4e6 S/m
[132]^a	Silicon	-	-	1	Oven	150/ 200	0.5/ 3-9	n.r.
[136]	Photo paper	n.r.	n.r.	1-2	Oven	110	0.4	R_{sh} = 0.19 Ω/sqr
[139]	PET, Polyimide, Silica	n.r.	5	10	Hot plate	150	0.67- 1	ρ = 20 μΩ−cm
[140]	Glass	n.r.	n.r.	n.r.	Oven	180	1	ρ = 11 μΩ−cm

^{a}Ink applied with spin coater.

Table C.3: Average drop size of silver ink in different paper substrates

Paper brand	Drop average diameter size (range) [μm]	Substrate Temperature [C]
Datajet	60 (56-64)	35
Techno	52 (48-56)	35
Filipaper	-	35
Epson A4[3]	44 (41-48)	35
Epson A6	40 (36-43)	35, 50, 60
Multilaser	52 (51-53)	35, 50, 60

Figure C.10: Images from optical microscope of printed structures with DS 18 μm and a single layer on Epson A6-size paper sintered at 128° C for 1.5 hr. Magnification factors of 20x, 50x, 200x, and 1000x are shown.
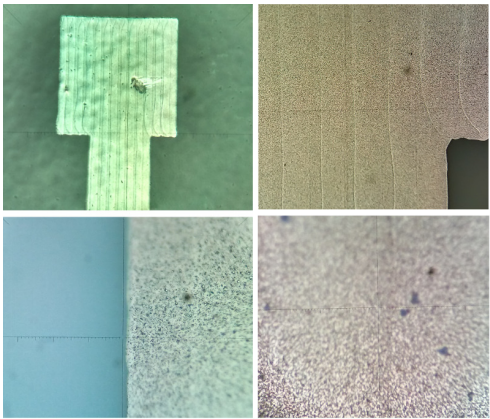
Source: The author.

Table C.4: Electrical performance of printed structures with silver ink on Epson A6-size paper. (DS = 18 μm, Sintered at 128° C for 1.5 hr.)

Layers	R_{SH} [Ω/sqr]	Thickness [μm]	Conductivity [S/m]
1	0,94	1.2	8.9e5
2	0,46	2.4	9.1e5

Figure C.11: Profile curves obtained with Detak profilometer, for 1 mm-wide printed lines with 1 and 2 layers on Epson A6-size paper with DS 18 μm, sintered at 128° C for for 1.5 hr.
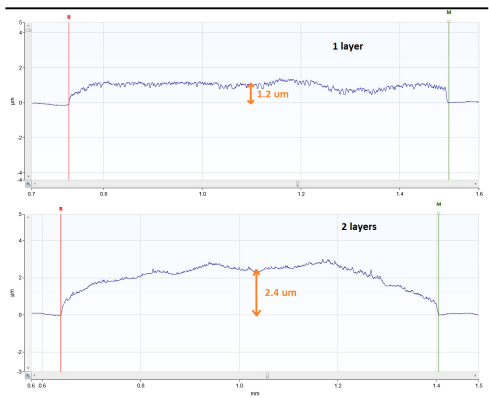
Source: The author.

C.2 DIELECTRIC PROPERTIES CHARACTERIZATION

A dielectric properties characterization of the materials used as substrates for the printed structures is mandatory, since permittivity and loss factor are two necessary parameters for inclusion into the models for electromagnetic simulations at the design stage of the chipless tag. There are plenty of methods for characterizing the dielectric properties of the substrates . Within the most reported for flexible substrates at RF frequencies we can cite the method based on the microstrip ring resonator [145], the T-resonator [146], and two transmission lines [147]. In this work, since rectangular shapes were preferred to circular due to fabrication simplicity, the two last methods were investigated.

In the T-resonator method, an opened parallel stub of a quarter of wavelength of the frequency of interest is added to a microstrip line. At this length, the stub behaves as grounded LC-series resonator. Therefore, from resonance frequency detected at a transmission coefficient measurement (measured with the aid of a VNA) , the approximated dielectric constant is obtained from the following relation:

$$4(L_{stub}) = \lambda = \frac{\lambda_0}{\sqrt{\varepsilon_{eff}}} \tag{C.4}$$

where L_{stub} is the stub length, λ and λ_0 are the wavelength at resonance of the medium and vacuum, respectively, and ε_{eff} is the effective permittivity, which embeds the permittivity of air and of the material of interest (the substrate) .

The total loss of the microstrip T-resonator is also obtained from the quality factor at the resonance frequencies by the following formula:

$$Q_t = \left(\frac{f_0}{BW_{3dB}} \right) F_l \tag{C.5}$$

where f_0 is the resonance frequency, BW_{3dB} is the 3dB-bandwidth of the valley resonance observed at the transmission coefficient ($S21$) measurement and F_l is the loading factor, which should be applied in order to unload the desired quality factor from the measurement ($F_l = 1/\sqrt{1 - 10^{S21_{dB}/20}}$). Since Q_t embeds all losses on the microstrip (radiation, conductors and dielectric loss), losses due to dielectric should be isolated. If the microstrips lines are smaller than 10 times the wavelength , the radiation losses are negligible. The conductor losses can be estimated by the ohmic losses caused by the non-ideal conductivity of the lines, which is also frequency dependent due to the *skin effect.*

The second method, referred here as the two-transmission lines (2-TL) method, has the advantage of obtaining the dielectric characteristics in a wide range of frequencies, compared to the previous method in which just the information was only available at the resonance (or odd multiples) frequency. Moreover, its differential measurement facilitates the measurement setup because it dispenses with complex calibrations procedures. Both the permittivity and loss factor can be found from the following equations [147]:

$$\varepsilon_{eff} = \frac{\Delta\theta}{2\pi f \Delta L}, \tag{C.6}$$

$$\alpha_t = -\frac{\ln(|S21_l|/|S21_s|)}{\Delta L} \tag{C.7}$$

where α_t is the total loss factor, $\Delta\theta$ is the difference of phase of both lines in rads, ΔL is the difference of length, and $|S21_{l(s)}|$ is the magnitude of the transmission coefficient of the long (short) line.

C.2.0.1 Experimental results

The methods described previously were used to characterize photo-quality paper from Multilaser. Even though, this paper was not suitable for printing structures, it is cheap and also sensitive to humidity of the environment, so it can be used for some sensing applications without requiring any extra materials. The methods were validated though the design of a patch antenna and compared simulation results using the dielectric parameters extracted. Since Epson paper is the paper selected for printing, their dielectric properties are also presented, however, an specialized probe kit for dielectric characterization was used in combination with a VNA.

After several tests, it was decided to fabricate the conductive traces of the microstrip structures with adhesive copper foil tape from 3M, since it was simpler, cheaper and faster than jetting or evaporating some metal over the paper. The prototypes for both extraction methods were build using 6 layers of photo-paper from Multilaser ($180\,\text{g/m2}$) glued at the borders and at some points near the middle, avoiding to be right below of the conductive traces. The measurements were carried on a ROHDE&SCHWARZ ZVB VNA.

In the case of the T-resonator, no *Thru-Reflect-Line* (TRL) calibration kit was performed for this prototype because no important

differences were detected when measuring a previous prototype in FR4 substrate, therefore usual SOLT calibration was done. A photograph of the resonator is seen in Figure C.12. The measurements were done at a VNA, with previous *Short-Open-Load-Thru* (SOLT) calibration. Measurement setup and transmission coefficient are shown in Fig. C.12.

Figure C.12: T-resonator prototype, transmission coefficient (S21) measurement setup and plot.
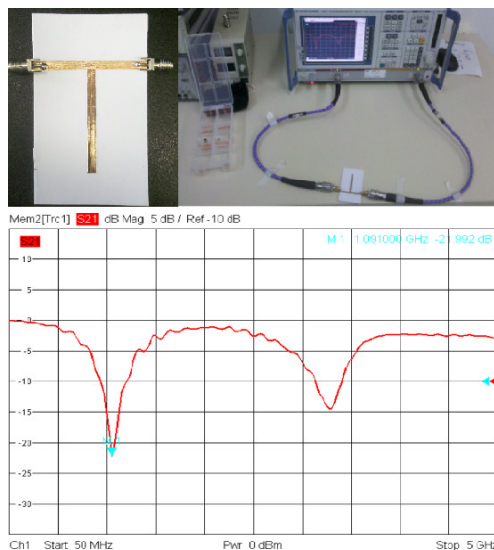
Source: The author.

For the second method, three transmission lines were build with 4, 6 and 8 cm of length. For the measurement, SOLT calibration was also previously applied. The transmission coefficient magnitude and phase were measured for each line, as shown in Figure C.13. Plots of the processed measurements are also shown, obtained from calculations in ADS software from Keysight©. Since the dimensions of the structures are less than 10 cm long, too much noisy results were obtained at low frequencies (< 1 GHz). Also, not trusty results were obtained at frequencies higher than 3 GHz, since SMA connectors and connector-to-substrate transition EM response begin to show up. The extracted parameters from both methods are summarized in Table C.5.

An experimental validation of the extracted values was done through the design of a patch antenna Multilaser paper substrate and copper tape, as shown in Fig. C.14. It was designed to resonate around

Figure C.13: Two-transmission-lines structures, transmission coefficient (S21) measurement setup and plots obtained from ADS.
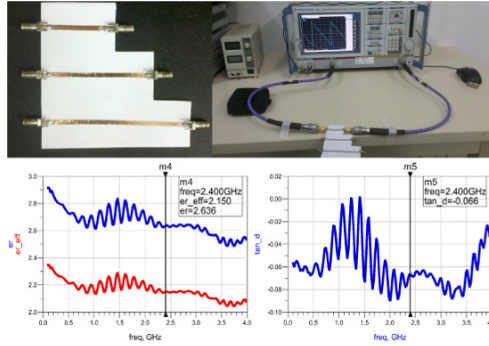
Source: The author.

2.4 GHz. The antenna was simulated in ADS with the Finite-Element Method (FEM) simulator, assuming an uniform substrate thickness of $t = 220\,\mu$m and a relative dielectric constant $\varepsilon_r = 2.636$ at 2.4 GHz. The simulated vs measured results of the reflection coefficient are also shown in Fig. C.14. There values of resonance frequencies obtained from simulation and measurement are well correlated, indicating a good dielectric constant extraction. Differences, on the absolute value of the S11 are possibly due to calibration errors during measurement, the SMA connector and the effect of the adhesive layer of the cooper tape, which is somehow significant compared to the thickness of the paper substrate [102].

The Epson paper was also characterized, since it is suitable for printing electronics, differently from Multilaser paper. Dielectric properties of Epson A6-size paper were extracted by using the dielectric

Table C.5: Extracted dielectric parameters of Multilaser paper from T-resonator and 2-TL methods

Method	T-res	2-TL
Eval. freq. [GHz]	1.09	2.4
ε	2.4	2.64
$\tan\delta$	0.77	0.66

Figure C.14: Patch antenna on paper for validating the dielectric parameters extracted from Multilaser paper. Simulated vs measured results of the normalized magnitude of the reflection coefficient to compare the resonance frequency. Dimensions of patch are $L = 40.3\,\mathrm{mm}$, $W = 48\,\mathrm{mm}$, of feed line are $l = 21.7\,\mathrm{mm}$, $w = 2\,\mathrm{mm}$, and of total antenna are $L_g = 80\,\mathrm{mm}$, $W_g = 90\,\mathrm{mm}$.
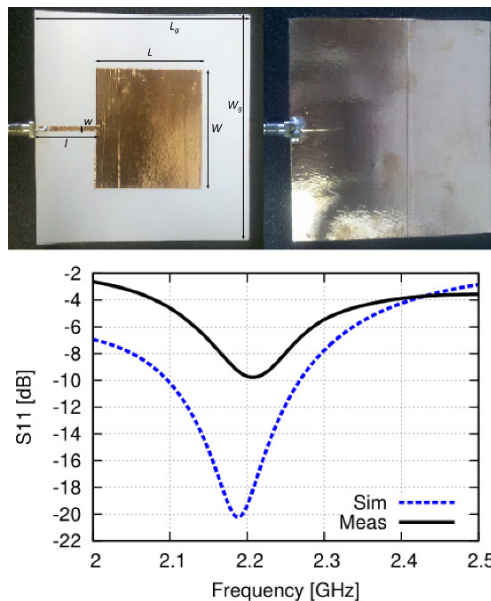
Source: The author.

kit probe N1501A from Keysight Technologies. This kit contains several open-coaxial probes of different sizes and shapes, which can estimate the dielectric permittivity and loss factor from reflection coefficient measurement with the aid of a VNA. The high-temperature probe has been used, from which its relation of dielectric properties and measured reflection coefficient depends on its specific physical dimensions [148]. For the measurement of the Epson paper, a handheld VNA Fieldfox from Keysight was used together with a commercial software from the same company which performs the reflection coefficient to dielectric parameters conversion. Measurement setup and results are depicted in Fig. C.15.

Figure C.15: Dielectric probe kit measurement setup and dielectric properties results of Epson A6-size paper.
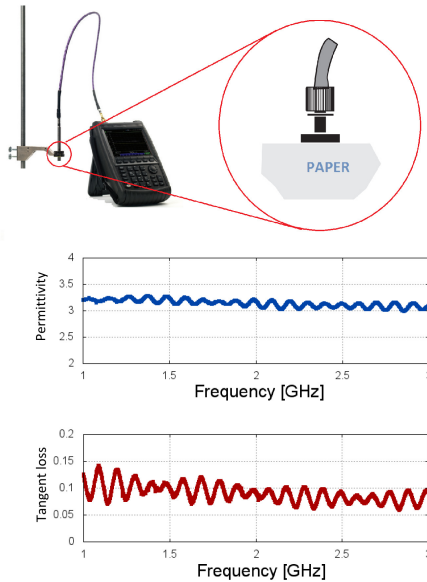
Source: The author.

C.3 FINAL DISCUSSION AND CONCLUSIONS

The materials characterization for realizing chipless tags on flexible and low cost substrates were performed. Specifically, different paper substrates were tested and its suitability for printed electronics was studied.

Particularly, conductivity measurements for silver-nanoparticle inks reported in this section was intended to summarized the theory, methodology, infrastructure and instrumentation needed for this type of characterization. Some specific conclusions can be stated from the obtained conductivity measurements:

- Drop spacing have to be carefully selected in order to make sure of obtaining homogeneous continuous patterns.

- Sintering process by heating needs to be evaluated both versus time and temperature, in order to detect the best achievable

scenario of conductivity for the selected substrate.

- Excess of temperature time can be prejudicial, rather than advantageous, so obtaining this maximum time is really important for the optimization of the printing process.

- Previous high magnification with optical microscope proved useful to examine the suitability of paper substrates for inkjet printing conductive traces.

- Scanning electron microscope (SEM) images can be useful to observe the sintering level on the silver nanoparticles at the worked temperatures with the convection oven.

Regarding dielectric measurements, it can be deduced that it is very important that each type of paper is correctly characterized, because they have different dielectric properties that will have direct influence on the chipless tag design. The two type of papers from different vendors that were studied showed different performances, which are summarized in Table C.6. It is concluded that Multilaser paper can be attractive as a low-cost green RF substrate alternative to traditional substrates used for electronic circuits. It can be also used as substrate for chipless tags or passive electronics in which the conductive traces are not printed, but other type of material such as copper tape is used instead [149]. Epson paper is the most indicated for printed chipless tags, although it stands lower temperatures, which impacts on the final conductivity, and would require an additional coating for humidity sensing purposes. Both papers can be also used as sensors due to its responsivity to humidity.

In addition, some specific conclusions can be stated from our results of dielectric characterization:

Table C.6: Performance comparison between different paper types studied

Brand	Size	Quality	Price [R$]	Good for printing?	Max. temp. [° C]	Sensitive to humidity?
Multilaser	A4	Photo - inkjet	0.60	no	145	yes
Epson	A6	Photo - inkjet	0.78	yes	130	yes

- The T-resonator method is a simple method to evaluate the dielectric characteristics on flexible substrate, although information only appears at a single resonating frequency and many structures may be constructed of a curve of dielectric parameters vs frequency is desirable.

- The two-transmission line method is attractive because it requires no calibration since it depends on the length difference of the lines. Similar results with the T-resonator method were accomplished, however not with enough precision.

- The patch antenna experimental verification of both methods revealed good accuracy on the extraction methods.

- Copper tape works well enough as conductor for methods realized, being a fast and cheaper solution than using silver ink for the dielectric measurement.

- T-resonator and Two transmission line methods both required a thick (> 1mm) layer of dielectric in order to attain wide enough lines for a $50\,\Omega$ characteristic impedance. This is a drawback in terms of time a manageability of the device under test. Other methods, such as some based on CPW, can be considered.

There is one more consideration that must be stated at this point. In RF and microwave circuits, the ohmic losses cause performance degradation since part of the EM energy is dissipated as thermal energy. In the case of radiating elements, such as antennas and chipless tags, ohmic losses reduce the effective gain, so less power is radiated, impacting directly on interrogating distances. The sheet resistance characterized from the measurements of the printed structures in Epson A6-size paper just provides DC (low frequency) information. At higher frequencies, the current circulating through a conductor tends to flow only near the surface. This means that the effective cross-area section through which the current passes is effectively decreased, which causes an equivalent higher resistivity, or less conductivity. In order to account with this effect, a common parameter known as *skin depth* is usually employed in microwave and RF devices The skin depth is the effective RF thickness that determines the final cross-area section for the circulating current. In metals, the skin depth (δ_s) can be calculated approximately as the inverse of the real part of the complex wave propagation constant, which results in the expression:

$$\delta_s = \sqrt{\frac{2}{\omega\mu\sigma}}, \tag{C.8}$$

where ω is the angular frequency, μ is the effective permeability, and σ is the material conductivity.

From this concept, the sheet resistance for RF frequencies is calculated by introducing the *skin effect* [150]:

$$R_{SH}^{RF} = \frac{1}{\sigma\delta_s(1 - e^{-t/\delta_s})}, \tag{C.9}$$

where t is the thickness of the conductor.

This previous equation is valid only when $t > \delta$, since at lower values wave reflections at the metal-substrate interfaces become significant. In printed chipless tags operating at RF, it is often the case that the printed layers thickness are on the order of some μm, so specific characterization procedures for obtaining the sheet resistance must be employed [151]. For example, at 0.92 GHz, the skin depth for an equivalent conductivity of 1e6 S/m ($R_{SH} = 0.8\,\Omega/$sqr, $t = 1.2\,\mu$m) is $16.3\,\mu$m, and at 2.5 GHz, is $9.9\,\mu$m, which in both cases is much more than the thickness of printed layers with conductive inks, at least with by inkjet printing processes. This fact should be taken into consideration on the final performance of a printed chipless sensing tag.

BIBLIOGRAPHY

[1] R. Minerva, A. Biru and D. Rotondi, "Towards a definition of the Internet of Things (IoT)", IEEE, 2015.

[2] Ericsson, "Internet of things forecast", Available at: `https://www.ericsson.com/en/mobility-report/internet-of-things-forecast`

[3] Cisco, "Internet of things", `https://www.cisco.com/c/dam/en/us/products/collateral/se/internet-of-things/at-a-glance-c45-731471.pdf`

[4] Ahlgren, M. Hidell and E. C. H. Ngai,"Internet of Things for Smart Cities: Interoperability and Open Data," in *IEEE Internet Computing*, vol. 20, no. 6, pp. 52-56, Nov.-Dec. 2016.

[5] Z. Bi, L. D. Xu and C. Wang, ''Internet of Things for Enterprise Systems of Modern Manufacturing," in *IEEE Transactions on Industrial Informatics*, vol. 10, no. 2, pp. 1537-1546, May 2014.

[6] A. M. Ortiz, D. Hussein, S. Park, S. N. Han and N. Crespi, "The Cluster Between Internet of Things and Social Networks: Review and Research Challenges," in IEEE Internet of Things Journal, vol. 1, no. 3, pp. 206-215, June 2014.

[7] C. Arcadius Tokognon, B. Gao, G. Y. Tian and Y. Yan, "Structural Health Monitoring Framework Based on Internet of Things: A Survey," in *IEEE Internet of Things Journal*, vol. 4, no. 3, pp. 619-635, June 2017.

[8] M. Wollschlaeger, T. Sauter and J. Jasperneite, "The Future of Industrial Communication: Automation Networks in the Era of the Internet of Things and Industry 4.0," in *IEEE Industrial Electronics Magazine*, vol. 11, no. 1, pp. 17-27, March 2017.

[9] Solanas et al., "Smart Health: A Context-Aware Health Paradigm within Smart Cities", in *IEEE Comm. Mag*, vol 52, no 8, 2014.

[10] G. Kobayashi, M. E. Quilici-Gonzalez, M. C. Broens and J. A. Quilici-Gonzalez, "The Ethical Impact of the Internet of Things in Social Relationships: Technological mediation and mutual trust,"

in *IEEE Consumer Electronics Magazine*, vol. 5, no. 3, pp. 85-89, July 2016.

[11] I. Kounelis, G. Baldini, R. Neisse, G. Steri, M. Tallacchini and A. Guimaraes Pereira, "Building Trust in the Human-Internet of Things Relationship," in *IEEE Technology and Society Magazine*, vol. 33, no. 4, pp. 73-80, winter 2014.

[12] P. A. Laplante and N. Laplante, "The Internet of Things in Healthcare: Potential Applications and Challenges," in *IT Professional*, vol. 18, no. 3, pp. 2-4, May-June 2016.

[13] J. Luo and R. Eitel, "An Integrated Low Temperature Co-Fired Ceramic-Based Clark-Type Oxygen Sensor," in *IEEE Sensors Journal*, vol. 17, no. 6, pp. 1590-1595, March15, 15 2017.

[14] R. Goncalves et al., "RFID-Based Wireless Passive Sensors Utilizing Cork Materials," in *IEEE Sensors Journal*, vol. 15, no. 12, pp. 7242-7251, Dec. 2015.

[15] C. Mariotti, W. Su, B. S. Cook, L. Roselli and M. M. Tentzeris, "Development of Low Cost, Wireless, Inkjet Printed Microfluidic RF Systems and Devices for Sensing or Tunable Electronics," in *IEEE Sensors Journal*, vol. 15, no. 6, pp. 3156-3163, June 2015.

[16] N. Tahir and G. Brooker, "Toward the Development of Millimeter Wave Harmonic Sensors for Tracking Small Insects," in *IEEE Sensors Journal*, vol. 15, no. 10, pp. 5669-5676, Oct. 2015.

[17] P. Kumar, et al., "The rise of low-cost sensing for managing air pollution in cities, " in *Environment international*, vol. 75, pp.199-205, 2015.

[18] C. Occhiuzzi, S. Caizzone and G. Marrocco, "Passive UHF RFID Antennas for Sensing Applications: Principles, Methods and Classifications," in *IEEE Antennas and Propagation Magazine*, vol. 44, no. 6, pp. 14-34, December, 2013.

[19] S. Caizzone and E. DiGiampaolo, "Wireless Passive RFID Crack Width Sensor for Structural Health Monitoring," in *IEEE Sensors Journal*, vol. 15, no. 12, pp. 6767-6774, Dec. 2015.

[20] E. DiGiampaolo, A. DiCarlofelice and A. Gregori, "An RFID-Enabled Wireless Strain Gauge Sensor for Static and Dynamic Structural Monitoring," in *IEEE Sensors Journal*, vol. 17, no. 2, pp. 286-294, Jan.15, 15 2017.

[21] PhaseIV, `http://www.phaseivengr.com/wp-content/uploads/2014/01/61-100027-00-UHF-Passive-DL-BAP-rev1_5-standard-res.pdf`.

[22] RFMicron, `http://rfmicron.com/temp-sensor`.

[23] ON Semiconductors, `http://www.onsemi.com/pub/Collateral/SPS1M002-D.PDF`.

[24] Idtechex, " RFID sensors 2017-2027 forecast players and opportunities". Available at: `http://www.idtechex.com/research/reports/rfid-sensors-2017-2027-forecasts-players-opportunities-000518.asp`

[25] G Martins and F. R. Sousa, "An RF-Powered Temperature Sensor Designed for Biomedical Applications, " in *Journal of Integrated Circuits and Systems*, JICS, (Ed. Português), vol. 9, pp. 7-15, 2014.

[26] E. A. U. Calpa, A. U. A. Florian, F. Ramirez, J. S. Riquelme, J. C. B. Reyes and F. E. Segura-Quijano, "Towards Fully Integrated Low-Cost Inductive Powered CMOS Wireless Temperature Sensor," in *IEEE Transactions on Industrial Electronics*, vol. 64, no. 11, pp. 8718-8727, Nov. 2017.

[27] Thinfilm, "Thinfilm Smart Label for Temperature Threshold Detection". `http://thinfilm.no/products-sensor-platform`

[28] Tedjini, S. et al., "Hold the Chips: Chipless Technology, an Alternative Technique for RFID," *IEEE Microwave*, vol.14, no.5, pp.56-65, July, 2013.

[29] S. Dey, J.K. Saha and N.C. Karmakar, "Smart Sensing: Chipless RFID Solutions for the Internet of Everything," in *IEEE Microwave*, vol. 16, no. 10, pp. 26-39, Nov., 2015.

[30] Das, R and Harrop, P., "RFID Forecasts, Players and Opportunities 2016-2026," IDTechEx, 2015.

[31] Girbau, D. Ramos, A. Lazaro, A. Rima, S. Villarino, R., "Passive Wireless Temperature Sensor Based on Time-Coded UWB Chipless RFID Tags," Microwave Theory and Techniques, IEEE Transactions on , vol.60, no.11, pp.3623,3632, Nov. 2012

[32] Amin, E.M.; Bhuiyan, M.S.; Karmakar, N.C.; Winther-Jensen, B., "Development of a Low Cost Printable Chipless RFID Humidity Sensor," *Sensors Journal*, IEEE , vol.14, no.1, pp.140,149, Jan. 2014.

[33] C. Carlowitz, Christian et al., "An ultra-wideband time domain reflectometry chipless RFID system with higher order modulation schemes," in *IEEE German Microw. Conf.*, GeMiC, 2016.

[34] B. Li, O. Yassine and J. Kosel, "Integrated passive and wireless sensor for magnetic fields, temperature and humidity," 2013 IEEE SENSORS, Baltimore, MD, 2013, pp. 1-4.

[35] Forouzandeh, Mohammadali, and Nemai Chandra Karmakar. "Chipless RFID tags and sensors: a review on time-domain techniques." Wireless Power Transfer 2.02 (2015): 62-77.

[36] Scheer, Jim, and William A. Holm. Principles of modern radar. Eds. Mark A. Richards, and William L. Melvin. SciTech Pub., 2010.

[37] N. C. Karmakar, "Tag, You're It," in *IEEE Microwave*, vol. 17, no. 7, pp. 64-74, July, 2016.

[38] Amin et al., "Towards an Intelligent EM Barcode."

[39] D. Lu et al., "Highly sensitive chipless wireless relative humidity sensor based on polyvinyl-alcohol film," in *IEEE Antennas Propag. Society Int. Symp.* APSURSI. 2014, pp. 1612-1613.

[40] Nair, R.S.; Perret, E.; Tedjini, S.; Baron, T., "A Group-Delay-Based Chipless RFID Humidity Tag Sensor Using Silicon Nanowires," in Antennas and Wireless Propagation Letters, IEEE , vol.12, no., pp.729-732, 2013.

[41] Costa, "Encoding/Decoding Strategies for Frequency Domain Chipless RFIDs Employing Periodic Surfaces", URSI, 2016.

[42] M. Pöpperl, J. Adametz and M. Vossiek, "Polarimetric Radar Barcode: A Novel Chipless RFID Concept With High Data Capacity and Ultimate Tag Robustness".

[43] Sebastian Sauer and Wolf-Joachim Fischer, "A Passive Wireless Humidity Th reshold Monitoring Sensor Principle Based on Deliquescent Saltsanda Diffusion Based Irreversible State Change," in *IEEE Sensors J.*, vol. 14, no .4, pp. 971-978, Apr., 2014.

[44] M. Borgese et al.,"An Inkjet Printed Chipless RFID Sensor for Wireless Humidity Monitoring," in *IEEE Sensors Journal*, vol. 17, no. 15, pp. 4699-4707, Aug.1, 1 2017.

[45] M. Garbati, R. Siragusa, E. Perret and C. Halopé, "Impact of an IR-UWB Reading Approach on Chipless RFID Tag,´´ in *IEEE Microwave and Wireless Components Letters*, vol. 27, no. 7, pp. 678-680, July 2017.

[46] R.V. Koswatta and N.C. Karmakar, "A novel reader architecture based on UWB chirp signal interrogation for multiresonator-based chipless RFID tag reading," in *IEEE Trans. Microw. Theory Tech.*, vol. 60, no. 9, pp. 2925-2933, 2012.

[47] Vena, A.; Babar, A.A.; Sydanheimo, L.; Tentzeris, M.M.; Ukkonen, L., "A Novel Near-Transparent ASK-Reconfigurable Inkjet-Printed Chipless RFID Tag," in *Antennas and Wireless Propagation Letters, IEEE*, vol.12, no., pp.753-756, 2013.

[48] M. A. Islam and N. C. Karmakar, "Real-World Implementation Challenges of a Novel Dual-Polarized Compact Printable Chipless RFID Tag," in *IEEE Transactions on Microwave Theory and Techniques*, vol. 63, no. 12, pp. 4581-4591, Dec. 2015.

[49] Costa, "Normalization Free Chipless RFIDs by Using Dual-Polarized Interrogation", in *Trans on MTT*. 2016.

[50] A. Vena, Arnaud, E. Perret and S. Tedjni, "A depolarizing chipless RFID tag for robust detection and its FCC compliant UWB reading system," in *IEEE Trans. Microw. Theory Tech.*, vol. 61, no. 8, pp. 2982-2994, 2013.

[51] M. Martinez and D. Van der Weide, "Circular polarization on depolarizing chipless RFID tags," in *IEEE Radio Wireless Symp.*, Austin, TX, RWS, 2016, pp. 145-147.

[52] M. A. Islam and N. C. Karmakar, "Compact Printable Chipless RFID Systems," in *IEEE Transactions on Microwave Theory and Techniques*, vol. 63, no. 11, pp. 3785-3793, Nov. 2015.

[53] Mandel, Christian, et al. "Metamaterial-inspired passive chipless radio-frequency identification and wireless sensing." annals of telecommunications-annales des télécommunications 68.7-8 (2013): 385-399.

[54] A. Vena et al., "Design of Chipless RFID Tags Printed on Paper by Flexography," in *IEEE Transactions on Antennas and Propagation*, vol. 61, no. 12, pp. 5868-5877, Dec. 2013.

[55] A. Vena, E. Perret and S. Tedjini, "Design of Compact and Auto-Compensated Single-Layer Chipless RFID Tag," in IEEE Transactions on Microwave Theory and Techniques, vol. 60, no. 9, pp. 2913-2924, Sept. 2012.

[56] Feng, Yi, et al. "Low-Cost Printed Chipless RFID Humidity Sensor Tag for Intelligent Packaging." *Sensors Journal*, IEEE, vol.15., no.6, 2015, pp. 3201-3208.

[57] S. Preradovic and N.C. Karmakar, " Multiresonator based chipless RFID tag and dedicated RFID reader," in *Microwave Symp.Digest*, IEEE MTT-S, 2010.

[58] Vena, Arnaud, Etienne Perret, and Smail Tedjini. Chipless Rfid Based on Rf Encoding Particle: Realization, Coding and Reading System. Elsevier, 2016.

[59] Kubina, B.; Mandel, C.; Schussler, M.; Sazegar, M.; Jakoby, R., "A wireless chipless temperature sensor utilizing an orthogonal polarized backscatter scheme," in Microwave Conference (EuMC), 2012 42nd European , vol., no., pp.61-64, Oct. 29 2012-Nov. 1 2012.

[60] Karmakar, Nemai Chandra, Emran Md Amin, and Jhantu Kumar Saha. Chipless RFID Sensors. John Wiley & Sons, 2016.

[61] Mandel et al., "A Wireless Passive Strain Sensor."

[62] Noor, T., et al. "High-density chipless RFID tag for temperature sensing." Electronics Letters 52.8 (2016): 620-622.

[63] A. Traille et al., "A wireless passive RCS-based temperature sensor using liquid metal and microfluidics technologies," 2011 41st European Microwave Conference, Manchester, 2011, pp. 45-48.

[64] A. Vena, E. Perret and S. Tedjini, "A compact chipless RFID tag using polarization diversity for coding and sensing."

[65] . Vena et al.,"An Embroidered Two-Dimensional Chipless Strain Sensor for Wireless Structural Deformation Monitoring" in IEEE Sensors Journal, vol. 13, no. 12, pp. 4627-4637, Dec. 2013.

[66] E. M. Amin, R. Bhattacharyya, S. Sarma and N. C. Karmakar, "Chipless RFID tag for light sensing," 2014 IEEE Antennas and Propagation Society International Symposium (APSURSI), Memphis, TN, 2014, pp. 1308-1309.

[67] Vena et al., "A Novel Inkjet-Printed Wireless Chipless Strain and Crack Sensor on Flexible Laminates." *Antennas and Propagation Society International Symposium* (APSURSI), 2014 IEEE, Memphis, TN, 2014, pp. 1294-1295.

[68] A. Vena et al., "A Fully Inkjet-Printed Wireless and Chipless Sensor for CO2 and Temperature Detection." in *IEEE Sensors J.*, vol .15, no. 1, pp. 89-99, 2015.

[69] M. Yang et al., "A Resistance-Type Sensor Based on Chipless RFID," in *IEEE Transactions on Antennas and Propagation*, vol. 65, no. 7, pp. 3319-3325, July 2017.

[70] C. Mandel, B. Kubina, M. Schüßler and R. Jakoby, "Passive chipless wireless sensor for two-dimensional displacement measurement," 2011 41st European Microwave Conference, Manchester, 2011, pp. 79-82.

[71] E. M. Amin, M. S. Bhuiyan, N. C. Karmakar and B. Winther-Jensen, "Development of a Low Cost Printable Chipless RFID Humidity Sensor," in *IEEE Sensors Journal*, vol. 14, no. 1, pp. 140-149, Jan. 2014.

[72] A. Vena, E. Perret, S. Tedjini, D. Kaddour, A. Potie and T. Barron, "A compact chipless RFID tag with environment sensing capability," 2012 IEEE/MTT-S International Microwave Symposium Digest, Montreal, QC, Canada, 2012, pp. 1-3.

[73] J. Lorenzo, D. Girbau, A. Lazaro, and R. Villarino, "Temperature sensor based on frequency-coded chipless RFID tag", in Microwave and Optical Technology Letters", vol. 56, no. 10, pp. 2411–2415, 2014.

[74] A. Vena, E. Perret, D. Kaddour and T. Baron, "Toward a Reliable Chipless RFID Humidity Sensor Tag Based on Silicon Nanowires," in IEEE Transactions on Microwave Theory and Techniques, vol. 64, no. 9, pp. 2977-2985, Sept. 2016.

[75] E. Perret, "Permittivity characterization based on Radar Cross measurements," 2016 URSI International Symposium on Electromagnetic Theory (EMTS), Espoo, 2016, pp. 457-460.

[76] Hester, J. G. D., and M. M. Tentzeris. "Inkjet-printed Van-Atta reflectarray sensors: A new paradigm for long-range chipless low cost ubiquitous Smart Skin sensors of the Internet of Things." Microwave Symposium (IMS), 2016 IEEE MTT-S International. IEEE, 2016.

[77] C. A. Balanis, *Antenna Theory: Analysis and Design.* 3rd edition: John Wiley & Sons. Inc., 2005.

[78] "IEEE Standard for Definitions of Terms for Antennas,´´ in *IEEE Std 145-2013* (Revision of IEEE Std 145-1993), pp.1-50, March 6 2014.

[79] E. Knott, J.Shaeffer and M. Tuley, *Radar Cross Section*, 2nd ed, SciTech Publishing, Inc., 2004.

[80] R. B. Green, "The general theory of antenna scattering," Ph.D. dissertation, Dept. Elect. Comput. Eng., Ohio State Univ, Columbus, OH, 1963.

[81] Balanis, Constantine A., *Modern antenna handbook.* John Wiley & Sons, 2011.

[82] Griffiths, David J, *Introduction to electrodynamics*, 4th ed. Prentice Hall, 2013.

[83] T. Ohira, "What in the World Is Q?,´´ in *IEEE Microwave Magazine*, vol. 17, no. 6, pp. 42-49, June 2016.

[84] Pendry, John B., et al. "Magnetism from conductors and enhanced nonlinear phenomena." Microwave Theory and Techniques, IEEE Transactions on 47.11 (1999): 2075-2084.

[85] R. Marqués, M. Ferran and M. Sorolla, "Metamaterials with negative parameters: theory, design and microwave applications´´, vol. 183, John Wiley & Sons, 2011.

[86] A. N. Reddy and S. Raghavan, "Split ring resonator and its evolved structures over the past decade," in *Proc. of the IEEE International Conference ON Emerging Trends in Computing, Communication and Nanotechnology* (ICECCN), Tirunelveli, pp. 625-629, 2013.

[87] Marques, Ricardo, Francisco Medina, and Rachid Rafii-El-Idrissi. "Role of bianisotropy in negative permeability and left-handed metamaterials." Physical Review B 65.14 (2002).

[88] S. Zuffanelli et al., "Analysis of the Split Ring Resonator (SRR) Antenna Applied to Passive UHF-RFID Tag Design,´´ in *IEEE Transactions on Antennas and Propagation*, vol. 64, no. 3, pp. 856-864, March 2016.

[89] Alici, Kamil Boratay, and Ekmel Ozbay. "Electrically small split ring resonator antennas". Journal of Applied Physics, vol.101, no.8, 2007).

[90] Yuandan Dong; Toyao, H.; Itoh, T., "Design and Characterization of Miniaturized Patch Antennas Loaded With Complementary Split-Ring Resonators," in Antennas and Propagation, IEEE Transactions on , vol.60, no.2, pp.772-785, Feb. 2012.

[91] Zuffanelli, S. et al., "On the Radiation Properties of Split-Ring Resonators (SRRs) at the Second Resonance," in *IEEE Trans. Microw. Theory Tech.*, vol. 63, no. 7, pp. 2133-2141, July, 2015.

[92] Garcia-Garcia, J., et al., "On the resonances and polarizabilities of split ring resonators." Journal of Applied Physics 98.3 (2005): 033103.

[93] J. D. Baena et al., "Equivalent-circuit models for split-ring resonators and complementary split-ring resonators coupled to planar transmission lines," Microwave Theory and Techniques, IEEE Transactions on, vol. 53, no.4, pp. 1451-1461, 2005.

[94] F. Alimenti et al., "A New Contactless Assembly Method for Paper Substrate Antennas and UHF RFID Chips," in *IEEE Transactions on Microwave Theory and Techniques*, vol. 59, no. 3, pp. 627-637, March 2011.

[95] A. Vena, E. Perret, and S. Tedjini. "Chipless RFID tag using hybrid coding technique." *IEEE Trans. Microw. Theory Tech.*, vol. 59, no. 12, pp. 3356-3364, 2011.

[96] N. K. Das, S. M. Voda, and D. M. Pozar, "Two methods for the mea-surement of substrate dielectric constant." *IEEE Trans. Microw. Theory Tech.*, vol. MTT-35, no. 7, pp. 636–642, jul. 1987.

[97] S. Manzari, C. Occhiuzzi, S. Nawale, A. Catini, C. Di Natale and G. Marrocco, "Polymer-doped UHF RFID tag for wireless-sensing of humidity," in *IEEE International Conference on RFID* (RFID), Orlando, FL, 2012, pp. 124-129.

[98] Virtanen, J. and Ukkonen, L. and Bjorninen, T. and Elsherbeni, A.Z. and Sydnheimo, L. "Inkjet-Printed Humidity Sensor for Passive UHF RFID Systems." *Instrumentation and Measurement, IEEE Transactions on*, vol. 60, no.8, pp. 2768-2777, 2011.

[99] W. Wiesbeck and D. Kahny, "Single reference, three target calibration and error correction for monostatic, polarimetric free space measurements," in *Proc. IEEE*, vol. 79, no. 10, pp. 1551-1558, Oct., 1991.

[100] Fontana, A. J. (2008). Appendix A: Water Activity of Saturated Salt Solutions. In Water Activity in Foods (eds G. V. Barbosa-Cánovas, A. J. Fontana, S. J. Schmidt and T. P. Labuza).

[101] E. Amin et al., "Polyvinyl-Alcohol (Pva)-Based RF Humidity Sensor in Microwave Frequency," Progress In Electromagnetics Research B, vol. 54, pp. 149-166, 2013.

[102] F. Alimenti, P. Mezzanotte, M. Dionigi, M. Virili and L. Roselli, "Microwave Circuits in Paper Substrates Exploiting Conductive Adhesive Tapes," in IEEE Microwave and Wireless Components Letters, vol. 22, no. 12, pp. 660-662, Dec. 2012.

[103] Khan, S.; Lorenzelli, L.; Dahiya, R.S., "Technologies for Printing Sensors and Electronics Over Large Flexible Substrates: A Review," in Sensors Journal, IEEE , vol.15, no.6, pp.3164-3185, June 2015.

[104] A. Vena et al., "A Fully Inkjet-Printed Wireless and Chipless Sensor for CO2 and Temperature Detection," in *IEEE Sensors J.*, vol. 15, no. 1, pp. 89-99, 2015.

[105] A. Vena et al., "Toward reliable readers for chipless RFID systems," in *General Assembly and Scientific Symposium*, URSI GASS, 2014, pp. 1-4.

[106] N.C. Karmakar et al., *Chipless RFID reader architecture*. Artech House, 2013.

[107] D. Betancourt et al., "Bending and Folding Effect Study of Flexible Fully Printed and Late-Stage Codified Octagonal Chipless RFID Tags," in *IEEE Trans. Antennas Propag.*", vol. 64, no. 7, pp. 2815-2823, 2016.

[108] Nijas, C. M., et al. "Low-cost multiple-bit encoded chipless RFID tag using stepped impedance resonator." IEEE Transactions on Antennas and Propagation 62.9 (2014): 4762-4770.

[109] M.A. Islam, A.K.M. Azad and N.C. Karmakar, "A novel reader architecture for chipless RFID tags," in *IEEE Asia-Pacific Symp. Electromagnetic Compatibility*, APEMC, 2013.

[110] M. Garbati et al. "High performance chipless RFID reader based on IR-UWB technology," in *IEEE 9th European Conf. Ant. Propag.*, EuCAP, 2015.

[111] G. Galindo-Romera et al., "An IoT Reader for Wireless Passive Electromagnetic Sensors," in *Sensors* vol. 17, no. 4, pp. 693, 2017.

[112] A. Ramos et al., "IR-UWB radar system and tag design for time-coded chipless RFID," in *IEEE 6th European Conf. Ant. Propag.*, EUCAP, 2012.

[113] A. Fawky et al., "Novel Pseudo-Noise coded chipless RFID system for clutter removal and tag detection," in *IEEE Int. Conf. RFID*, RFID, 2015.

[114] M. El-Hadidy et al., "Real-world testbed for multi-tag UWB chipless RFID system based on a novel collision avoidance MAC protocol," in *Trans. Emerging Telecommunications Tech.*, vol. 27, no. 12, pp. 1707-1714., 2016.

[115] L. Lee et al., "Compact Antenna Module With Optimized Tx-to-Rx Isolation for Monostatic RFID," in *IEEE Microw. Wireless Compon. Lett.*, vol. PP, no. 99, pp. 1-3, 2017.

[116] Z. Zhang et al., "Full-Duplex Wireless Communications: Challenges, Solutions, and Future Research Directions," in *Proc. IEEE*, vol. 104, no. 7, July, 2016.

[117] J.S. Boaventura, A. Oliveira and N. B. Carvalho, "Perfect Isolation: Dealing with Self-Jamming in Passive RFID Systems," in *IEEE Microwave*, vol. 17, no. 11, pp. 20-39, Nov., 2016.

[118] A. M. M. Chandran and M. Zawodniok, "Transmitter leakage analysis when operating USRP (N210) in duplex mode," in *Proc. IEEE Int. Instrum. Meas. Tech. Conf.*, I2MTC, Pisa, pp. 340-345, 2015.

[119] G. Lasser and C.F. Mecklenbräuker, "Self-interference noise limitations of RFID readers," in *IEEE Int. Conf. RFID*, RFID, 2015.

[120] A. Vena et al., "Theoretical study on detection distance for chipless RFID systems according to transmit power regulation standards," in *IEEE 9th European Conf. Ant. Propag.*, EUCAP, 2015.

[121] A. Ramos et al., "Temporal Separation Detection for Chipless Depolarizing Frequency Coded RFID," in *IEEE Trans. Microw. Theory Tech.*, vol. 64, no. 7, pp. 2326-2337, July, 2016.

[122] M. Khaliel, M. El-Hadidy and T. Kaiser, "Printable depolarizing chipless RFID tag based on DGS resonators for suppressing the clutter effects," 2015 9th European Conference on Antennas and Propagation (EuCAP), Lisbon, 2015, pp. 1-5.

[123] A Chipless RFID Based on Multiresonant High-Impedance Surfaces. IEEE MTT 2013.

[124] Y. Guo et al., "CMOS integrated low TX noise digital transmitter with tunable directional coupler for high performance UHF RFID reader," in *Microw. Optical Tech. Lett.*, vol. 58, no. 7, pp. 1750-1756, 2016.

[125] P. Kalansuriya, N.C. Karmakar and E. Viterbo, "On the Detection of Frequency-Spectra-Based Chipless RFID Using UWB Impulsed Interrogation," in *IEEE Trans. on Microw. Theory Tech.*, vol. 60, no. 12, pp. 4187-4197, Dec., 2012.

[126] USRP b210/b200 Bus Series. Ettus Research, 2015, [online] Available: https://www.ettus.com/content/files/b200-b210_spec_sheet.pdf

[127] J. Hershberger, T. Pratt and R. Kossler, "Automated calibration of a dual-polarized SDR radar," in *IEEE Conference on Antenna Measurements & Applications*, CAMA, Syracuse, NY, 2016, pp. 1-4.

[128] F. L. Cabrera and F.R. Sousa, "Contactless Characterization of a CMOS Integrated LC Resonator for Wireless Power Transferring."

in *IEEE Microw. Wireless Compon. Lett.*, vol. 25, no. 7, pp. 475-477, July, 2015.

[129] Fujifilm, "Jettable Fluid Formulation Guidelines´´, 2013 `http://dimatixsupport.fujifilmusa.com/deposition.htm`,

[130] J. Niittynen et al., "Alternative sintering methods compared to conventional thermal sintering for inkjet printed silver nanoparticle ink´´, Thin Solid Films, vol 556, pp 452–459, 2014.

[131] T. Ohlund et al., "Sintering methods for metal nanoparticle inks on flexible substrates´´, in Proc. NIP & Digital Fabrication Conference, no 2, pp 614–617, 2009.

[132] L. Inhwa et al., "Interfacial toughening of solution processed Ag nanoparticle thin films by organic residuals´´, J. of Nanotechnology, vol 23, no 48, 2012.

[133] M. Allen et al., "Substrate-facilitated nanoparticle sintering and component interconnection procedure ", J. of Nanotechnology, vol 21, no 47, 2010.

[134] Advanced Nano Products ANP, Silver jet ink products, `http://anapro.com/eng/product/silver_inkjet_ink.html`.

[135] J. Gao et al., "Printed Electromagnetic Coupler With an Embedded Moisture Sensor for Ordinary Passive RFID Tags", in IEEE Electron Device Letters, vol 32, no 12, pp 1767–1769, 2011.

[136] Y. Qian et al., "Printed Arduino Mini on Paper´´, 2013, `http://www.diva\discretionary{-}{}{}portal.org/smash/record.jsf?pid=diva2%3A630138&dswid=2617`

[137] N. Kim et al., "Highly conductive Ag nanoparticulate films induced by movable rapid thermal annealing applicable to roll-to-roll processing´´, Journal of The Electrochemical Society, vol 158, no 8, pp K165–K169, 2011.

[138] H. Kao et al., "RF Bandpass Filter on Flexible Substrate Fabricated with Inkjet Printing Technology´´, MRS, vol 11, pp. 23, 2012.

[139] G. Li et al., "Interlacing method for micro-patterning silver via inkjet printing", in Proc. IEEE Sensors, pp. 1687-1690, 2014.

[140] J. Bito et al., "Fully inkjet-printed multilayer microstrip patch antenna for Ku-band applications", in Proc. IEEE Antennas and Propagation Society International Symposium (APSURSI), pp 854–85, 2014.

[141] I. Miccoli et al., "The 100th anniversary of the four-point probe technique: the role of probe geometries in isotropic and anisotropic systems", in Journal of Physics: Condensed Matter, vol 27, no 22, 2015.

[142] S. Enderling et al., "Sheet resistance measurement of non-standard cleanroom materials using suspended Greek cross test structures", in IEEE Tran. Semiconductor Manufacturing, vol 19, no 1, pp 2–9, 2006.

[143] I. Huchings and G. Martin, "Inkjet technology for digital fabrication", John Wiley & Sons. 2012.

[144] S. Thorsteinsson et al., "Accurate microfour-point probe sheet resistance measurements on small samples´´, Review of Scientific Instruments, vol 80, no 5, 2009.

[145] L. Yang et al., "RFID Tag and RF Structures on a Paper Substrate Using Inkjet-Printing Technology", in IEEE Tran Microwave Theory and Techniques, vol 55, no 12, pp 2894–2901, 2007.

[146] , B. Cook and A. Shamim, "Inkjet Printing of Novel Wideband and High Gain Antennas on Low-Cost Paper Substrate", IEEE Tran Antennas and Propagation, vol 60, no 9, pp 4148–4156, 2012.

[147] H. Saghlatoon, L. Sydanheimo, L. Ukkonen and M. Tentzeris, "Optimization of Inkjet Printing of Patch Antennas on Low-Cost Fibrous Substrates," in IEEE Antennas and Wireless Propagation Letters, vol. 13, no. , pp. 915-918, 2014.

[148] D. Blackham and R. Pollard, "An improved technique for permittivity measurements using a coaxial probe", Instrumentation and Measurement, IEEE Transactions on, vol 46, vol 46, no 5, pp 1093–1099, 1997.

[149] F. Alimenti et al., "24-GHz CW radar front-ends on cellulose-based substrates: A new technology for low-cost applications," in Proc. IEEE MTT-S International Microwave Symposium (IMS), pp 1–4, 2015.

[150] J. Virtanen, "Development of Sensor Integrated and Inkjet-printed Tag Antennas for Passive UHF RFID Systems," Tamper University of Technology, 2012.

[151] X. Wang, A. Díaz-Rubio and S. A. Tretyakov, "An Accurate Method for Measuring the Sheet Impedance of Thin Conductive Films at Microwave and Millimeter-Wave Frequencies," in *IEEE Transactions on Microwave Theory and Techniques*, vol. 65, no. 12, pp. 5009-5018, Dec. 2017.

[152] R. A. Romero et al., "A low-cost passive wireless capacitive sensing tag based on split-ring resonator," in *IEEE Int. Instrum. Meas. Technol. Conf.*, Pisa, I2MTC. 2015, pp. 434-439.

[153] R. A. Romero et al., "Wireless Transducer based on split-ring resonator," in *Symposium on Microelectronics Technol. and Devices*, Salvador, SBMICRO. 2015.

[154] R. A. Romero, C. Rambo and F. Rangel, 'Exploiting the SRR for miniaturization and sensitivity of a humidity chipless sensor," in *MOMAG*, Porto Alegre, 2016.

[155] R. Romero, C. Rambo and F. Rangel, "Miniaturized chipless sensor with magnetically-coupled transducer for improved RCS", in *IEEE Microw. Wireless Compon. Lett.*, v. 27, p. 1-3, n. 2017.

[156] R. A. Romero, C. Rambo and F. Rangel, "Self-interference cancellation in chipless RFID readers for reading range enhancement," in *IEEE Int. Instrum. Meas. Technol. Conf.*, Texas, I2MTC. 2018.